Nanomechanical Sensing of Biological Interfacial Interactions

A Thesis

Submitted to the Faculty

of

Drexel University

by

Wenjian Du

in partial fulfillment of the

requirements for the degree

of

Doctor of Philosophy

December 2016

Dedication

I dedicate this dissertation to my parents, my twin brother and his wife, and my fiancée for their love and support.

Acknowledgements

I am deeply indebted to the following people who have touched my life in so many important ways and supported me in accomplishing this research successfully.

I thank all members of my dissertation committee Dr. Lynn S. Penn, Dr. Anthony W. Addison, Dr. Joe P. Foley, and Dr. Hai-feng (Frank) Ji from Chemistry Department at Drexel University for their support and assistance. I would also like to thank Dr. Nianli Sang from the Department of Biology at Drexel University and Dr. Zhihong Wang from Department of Chemistry and Biochemistry at University of Science for their participation in my dissertation committee. Special thanks to the chair Dr. Penn, I cannot express my gratitude enough for your careful comments and edits to this dissertation.

I am extremely grateful to the group members from Dr. Jun Xi's group: Jennifer Chen and Marcela Del Pilar Garcia, for their support and advice guiding me through these years. You took me in as a family when I first entered our lab. I would also like to thank Dr. Liming Zhao, Dr. Trevor King, Ahmed Bulhassan, and Jose Quejada, who taught me a lot and helped me start my research work. I have also learned so much and benefited immensely from our collaborator Dr. Linghao Zhong.

I wish to send my heartfelt appreciation to Tina Lewinsky, Sue Tang, Genell Sodano, Edward Thorne, Kyle Hess, Tim Wade, Virginia Nesmith, Edward Doherty, and Daniel Gray for all their help during my doctoral years.

I will always remember the Chemistry department community for your support and for enriching my life here in countless ways. I would like to extent my special thanks to all the past and current graduate students I have had the opportunity to interact with,

especially Xiang Liu, Zhen Qiao, Xue Sha, Noah Johnson, Erin Ennis, and Leah Pandiscia.

I want to thank my family for their unfailing love and support. My father, Xiyi, and mother, Huimei, gave me a solid grounding in my early life to realize my dreams and I thank them for their love and patience in me going half way around the world for such a large part of their lives. Special thanks to my twin brother, Wenshu, you can make me happy whenever I feel sad; you just know me so well. Thank you, Jieru, for always being there for me. I miss all of you so much. My fiancée, Jiaying, who supports me unconditionally as my life partner, best friend, unpaid coach, and cheerleader, I want to thank you for your love, patience, and confidence in me and for letting me keep my eye on the finishing line.

Last but not least, I am extremely grateful to my advisor, Dr. Jun Xi, who has unreservedly offered his mentorship, guidance, and generous support throughout my intellectual journey here at Drexel. Thank you for inspiring me with your wisdom, and for challenging me constantly in my growth as a researcher, scholar, and teacher. I also want to thank my advisor, Dr. Reinhard Schweitzer-Stenner, who have dedicated precious time to offer invaluable advice and encouragement for this dissertation. Your insights, probing questions, and helpful comments have strengthened this work immeasurably.

Table of Contents

List of Tables

List of Figures

Abstract

Nanomechanical Sensing of Biological Interfacial Interactions
Wenjian Du
Prof. Reinhard Schweitzer-Stenner
Prof. Jun Xi

Cellulose is the most abundant biopolymer on earth. Cellulase is an enzyme capable of converting insoluble cellulose into soluble sugars. Cellulosic biofuel produced from such fermentable simple sugars is a promising substitute as an energy source. However, its economic feasibility is limited by the low efficiency of the enzymatic hydrolysis of cellulose by cellulase. Cellulose is insoluble and resistant to enzymatic degradation, not only because the β-1,4-glycosidic bonds are strong covalent bonds, but also because cellulose microfibrils are packed into tightly bound, crystalline lattices. Enzymatic hydrolysis of cellulose by cellulase involves three steps—initial binding, decrystallization, and hydrolytic cleavage. Currently, the mechanism for the decrystallization has not yet been elucidated, though it is speculated to be the rate-limiting step of the overall enzymatic activity. The major technical challenge limiting the understanding of the decrystallization is the lack of an effective experimental approach capable of examining the decrystallization, an interfacial enzymatic activity on solid substrates. The work presented develops a nanomechanical sensing approach to investigate both the decrystallization and enzymatic hydrolytic cleavage of cellulose. The first experimental evidence of the decrystallization is obtained by comparing the results from native cellulase and non-hydrolytic cellulase. Surface topography has been applied to examine the activities of native cellulase and non-hydrolytic cellulase on cellulose

substrate. The study demonstrates additional experimental evidence of the decrystallization in the hydrolysis of cellulose. By combining simulation and monitoring technology, the current study also investigates the structural changes of cellulose at a molecular level. In particular, the study employs cellulose nanoparticles with a bilayer structure on mica sheets. By comparing results from a molecular dynamic simulation and the distance between cellulose layers monitored by means of the atomic force microscopy (AFM), the current study shows that water molecules can efficiently reduce the energy required for separating two layers of cellulose bilayers during hydration of cellulose bilayer nanoparticles. The findings of the study contribute to explicating the mechanism of cellulose the decrystallization, a free-energetically unfavorable process, through enzymatic hydrolysis of cellulase. The study also investigates the application of a cell-based microcantilever sensor to monitor the real-time ligand-induced response of living cells. These nanomechanical approaches offer unique perspectives on the interfacial activities of biological molecules.

(page intentionally left blank)

Chapter 1: Introduction

Three fossil fuels—petroleum, natural gas, and coal—have provided most of the world's energy in the past century and are predicted to account for 78% of the total global energy consumption in 2040. In the future, the worldwide consumption of petroleum will likely continue to increase, from 90 million barrels per day (BPD) in 2012 to 100 million BPD in 2020 and 121 million BPD in 2040[1]. Commentators predict that the production of conventional oil will reach a peak and begin to decline before 2030, or even sooner before 2020 (so-called *peak oil*: the hypothetical point when the global production of fossil oil reaches its maximum rate, after which production will gradually decline)[2]. Thus, the predicted energy crisis is increasingly become a major concern. To avoid the serious social and economic pitfalls following the peak oil, the Hirsch report emphasizes the need to find affordable alternatives and renewable energy sources, as well as to lessen the world's dependence on petroleum over time[3]. Hirsch indicates that use of renewable or alternative energy sources to replace petroleum is the most efficient method for mitigating the peak oil. Moreover, such energy sources should be able to fill the gap between global oil production and consumption at least 10 to 20 years before the peak oil. The five most common renewable energy sources include hydropower, geothermal, wind, solar, and biomass. These are the world's fastest-growing energy sources. In 2014, these renewable energy sources will account for 10% of total U.S. energy consumption and 13% of U.S. electricity generation, with an increase of 2.6% each year between 2012 and 2040. According to the Clean Power Plan (CPP) regulations in the U.S., an additional 7% of U.S. energy use will be renewable in 2020. By 2040, this growth will be 37%. Hydropower is the oldest and largest renewable energy source, but has irreversible

environmental impacts, such as the obstruction of fish migration, effects on the local ecology of rivers, and the relocation of the residents. Biomass is from plants and animals and is the second largest renewable energy source. Its energy comes from the sun through photosynthesis. When buried underground, it spontaneously but slowly turns into hydrocarbon fuels, such as coal. However, the formation of coal takes up to hundreds of millions of years. Biomass can be burned directly to produce a heating source with low energy density, or converted to liquid biofuels and biogas burned as fuels. Biofuels (bioethanol or biodiesel) are typically blended with petroleum fuels (gasoline and diesel) but can also be used by themselves. Bioethanol is usually made from sugars found in grains, like corn, or other sugar production crops, like sugar cane and beets. However, it is not the most ideal to convert edible crops or vegetables into energy materials, especially considering that the current population of the earth does not have enough food to live a healthy and active life[4]. Bioethanol can also be produced from inedible biomass, such as straw, corn stover, grasses, fast-growing trees, sawdust, and even waste paper. Given that the major component of such biomass is cellulose, this bioethanol is also called *cellulosic ethanol*. Although it is considered an advanced biofuel, its production involves a more complicated process than that of conventional bioethanol and thus more substantial production costs. Several challenges have to be overcome before making bioethanol a conventional form of energy, like petroleum fuel. One of them is the low efficiency of the enzymatic hydrolysis of cellulose. The mechanism of cellulose-cellulase interaction is still not fully understood. This chapter introduces the basic concepts of biofuel, cellulosic biomass, enzymatic hydrolysis of cellulosic biomass, and its recalcitrance to the cellulase enzyme.

1.1 Biofuel

Plants on earth absorb energy from the sun and store it as biomass energy. The history of biomass energy can be traced back to an age when hominin routinely used fire, roughly 350,000 years ago[5]. Biomass energy can be released through the direct burning of plants and their derivatives. It can also be converted to other forms, like methane gas, or biofuels such as biodiesel and bioethanol. The use of more biofuels can reduce the dependence of petroleum in the modern world. Moreover, they have significant environmental advantages over petroleum-based gasoline and diesel fuel.

Biodiesel can be made from vegetable oils, fats, or greases, and even recycled restaurant and kitchen grease. It is non-toxic, biodegradable, and less pollution than petroleum-based fuel. It can be sold as pure diesel or as a blend, combined with petroleum-based diesel fuel. A standard commercial biodiesel is B20 which is 20% biodiesel.

Bioethanol is primarily produced by a sugar fermentation process and contributes to 65% of the global ethanol production. There are two generations of bioethanol. The first generation is produced from a small proportion of the whole corn plant—starch—about half the mass of the dry corn kernel. The second generation of bioethanol, also known as the advanced biofuel, can be manufactured from various types of cellulosic biomass. There are two manufacturing paths: biochemical and thermochemical. The former uses enzymatic hydrolysis and yeast fermentation to convert cellulose, the structural components of plants, into ethanol. The latter employs pyrolysis to convert the whole plant to syngas, consisting of hydrogen and carbon monoxide. The syngas is then catalytically converted to bioethanol. While nearly all bioethanol produced in the U.S.

comes from corn starch, it is not considered the best practice to produce transportation fuel from edible food. Thus, ethanol produced from cellulosic feedstock, such as wood, grasses, straw, and agricultural waste, is considered a promising future trend.

Cellulosic biomass is more abundant and less expensive compared to corn and other sugar crops[6]. Particularly, straws and corn stalks are considered agricultural wastes. Furthermore, ethanol is much cleaner than gasoline—it burns more completely and the exhaust gas is quite clean. Moreover, the energy balance is positive for cellulosic biomass—the energy contained in the fuel is more than the energy required to produce it. These qualities make it an attractive alternative to traditional fuel. Additionally, it is carbon neutral—the carbon dioxide released when bioethanol burns is the same amount as previously absorbed by crops during photosynthesis. A carbon cycle such as this could be completed in less than a decade and the overall carbon release is null. By contrast, a similar carbon cycle for fossil fuel requires millions of years, and humans have burned such a large amount of fossil fuel that the CO_2 in the atmosphere is about 30% more than 150 years ago. The use of ethanol-added fuels, such as E85 (gasoline with 85% ethanol), can reduce the emission of greenhouse gases by 37.1%, and even E10 (gasoline with 10% ethanol, which is now the most prevalent gasoline sold in the U.S.) can reduce greenhouse gases by up to 3.9%[7]. Finally, the use of bioethanol greatly benefits the energy security and freedom of many economic entities as it can substantially reduce dependency on countries that produce crude oil. Bioethanol from cellulosic biomass is thus considered as having great potential.

However, while the application of additional renewable energy sources has significantly increased within the past decade, the commercialization process of

cellulosic biofuels has been slower than previously envisioned in 2007[8]. The price of bioethanol produced from cellulosic biomass remains high and can only be competitive when its price is less than $2.15/gallon[9]. The high price of bioethanol stems from the difficulty of converting cellulosic biomass to sugars, largely due to its relatively compressed molecular structure[6].

1.2 Cellulosic Biomass

There are three primary components of cellulosic biomass: cellulose, hemicellulose, and lignin. Through millions of years of evolution, it has developed a complex supramolecular structure by combining the three polymer materials used to strengthen plant cell walls (Figure 1-1). This complex, three-dimensional structure provides desirable mechanical properties in plants, and prevents plants from being attacked by microorganisms and other adverse physical and chemical factors[10]. Such recalcitrance is considered the principle obstacle that prevents the full use of cellulosic biomass.

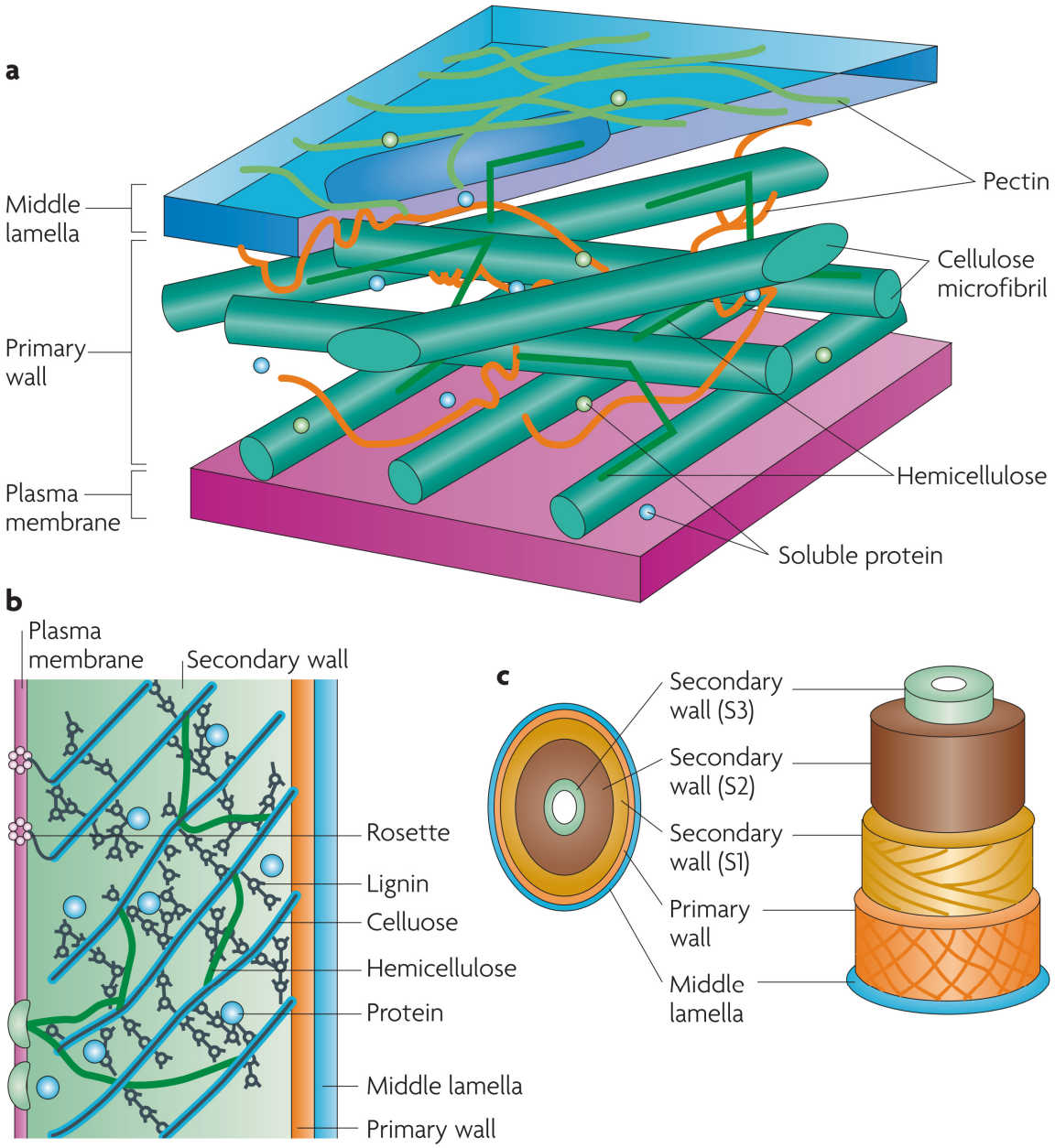

Figure 1-1. Plasma membrane and cell wall structure of plants.
Adapted from Sticklen, 2008. (a) Cell wall containing cellulose microfibrils, hemicellulose, lignin, pectin, and soluble proteins. (b) Cellulose synthase enzymes float in the plasma membrane. (c) Lignification appears in the S1, S2, and S3 layers of the cell wall.[11]

1.2.1 Cellulose

Cellulose is the skeletal structure of almost all plants and the most abundant biopolymer on earth[12]. It is particularly plentiful in non-food plants, such as trees and grasses[13]. A cellulose molecule is a linear polymer of D-anhydroglucopyranose units linked by *β*-1,4-glucosidic bonds (C1 of one glucose ring covalently bonded to C4 of the adjacent ring), see Figure 1-2. The repeating unit is composed of two anhydryoglucose rings ($(C_6H_{10}O_5)_n$; n = 10000 to 15000). The cellulose molecule chain has an unsubstituted hemiacetal on the reducing end and a hydroxyl group on the non-reducing end. When cellulose is synthesized by plants, van der Waals interactions between ring carbon atoms and intermolecular hydrogen bonding between –OH and –O of the adjacent molecules promotes parallel stacking of multiple cellulose chains, in turn producing elementary fibrils[14]. These fibrils then aggregate into larger microfibrils. The fibril matrix structures provide the mechanical properties of plants' cell walls, see Figure 1-3. Some cellulose chains in the regions within these microfibrils are highly ordered (crystalline region) and others are disordered (amorphous region)[15], see Figure 1-4.

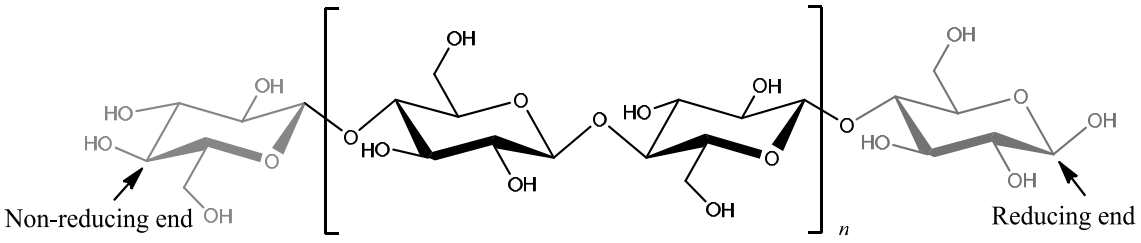

Figure 1-2. The molecular structure of a cellulose molecule.
Adapted from Xi, 2013. A linear polymer of D-anhydroglucopyranose units linked by β-1,4-glucosidic bonds. There is an unsubstituted hemiacetal on the reducing end and a hydroxyl group on the non-reducing end.[12]

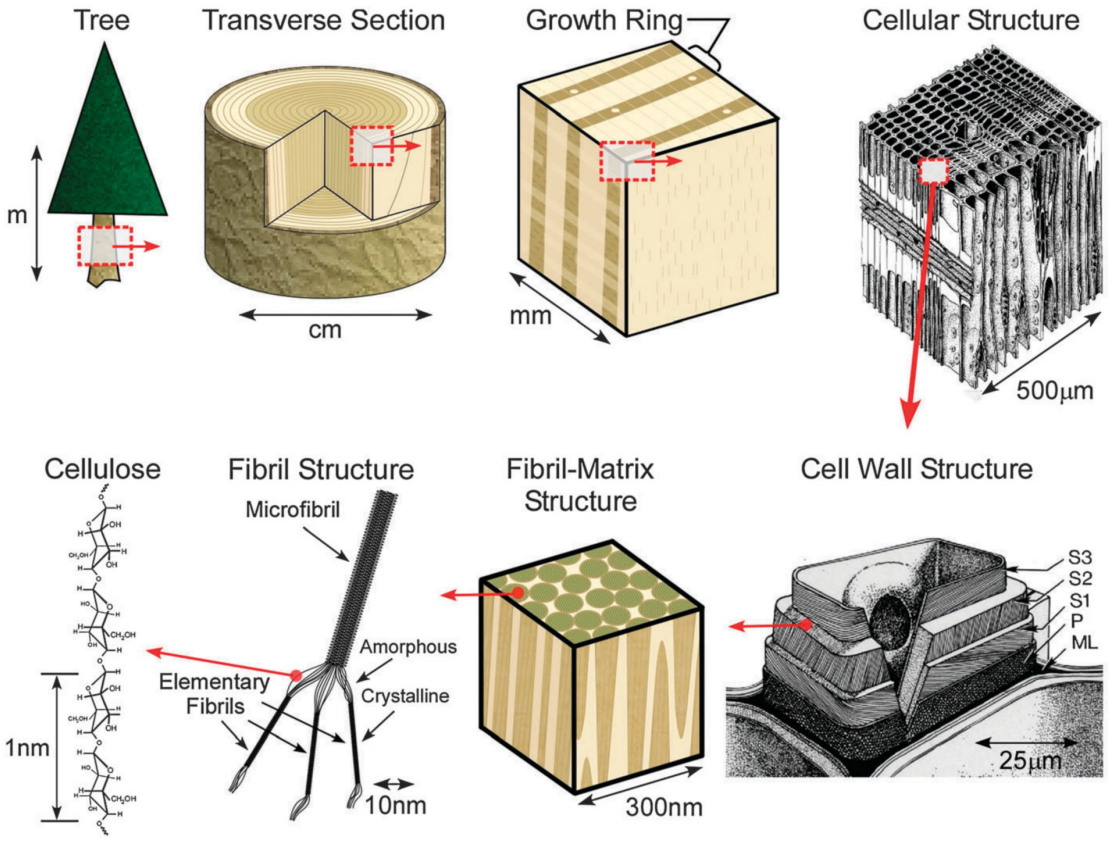

Figure 1-3. The structure of wood from the tree to the cellulose.
Adapted from Moon, 2008. (P = primary cell wall, S1, S2, S3 = cell wall layers, and ML = middle lamellae between tracheids)[16,17].

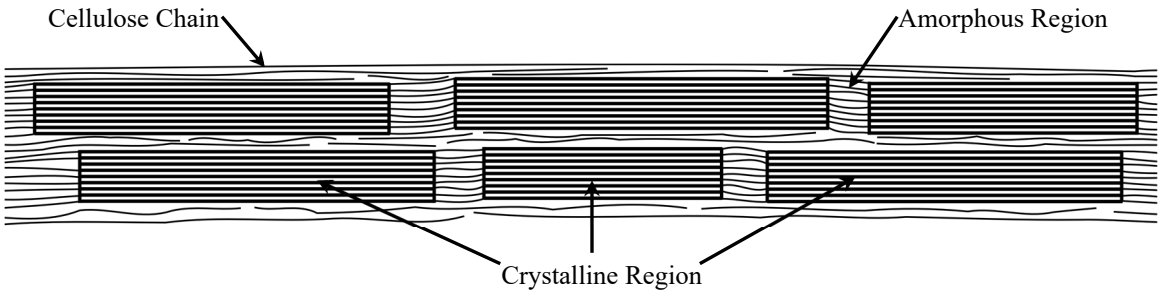

Figure 1-4. Cellulose microfibril showing crystalline and amorphous regions.

Cellulose is strong, crystalline, and resistant to hydrolysis. Various non-covalent interactions, such as hydrogen bonding and van der Waals interactions, are present in the ultrastructure of cellulose. Figure 1-5 shows the arrangement of the intra-sheet hydrogen bonding network in cellulose I_α and the resulting hydrophilic and the hydrophobic faces of the ring plane[15]. While O–H···O hydrogen bonding is primarily responsible for intra-sheet interactions in cellulose, both van der Waals interactions of ring carbon atoms and the much weaker C–H···O hydrogen bonding contribute to the inter-sheet interactions in cellulose[14]. Overall, because of such intra- and inter- chain non-covalent interactions, cellulose chains aggregate into various ultrastructure that neither melt nor dissolve in common solvents. Such aggregation prevents the direct access to each cellulose chain by other biomolecules, such as cellulase.

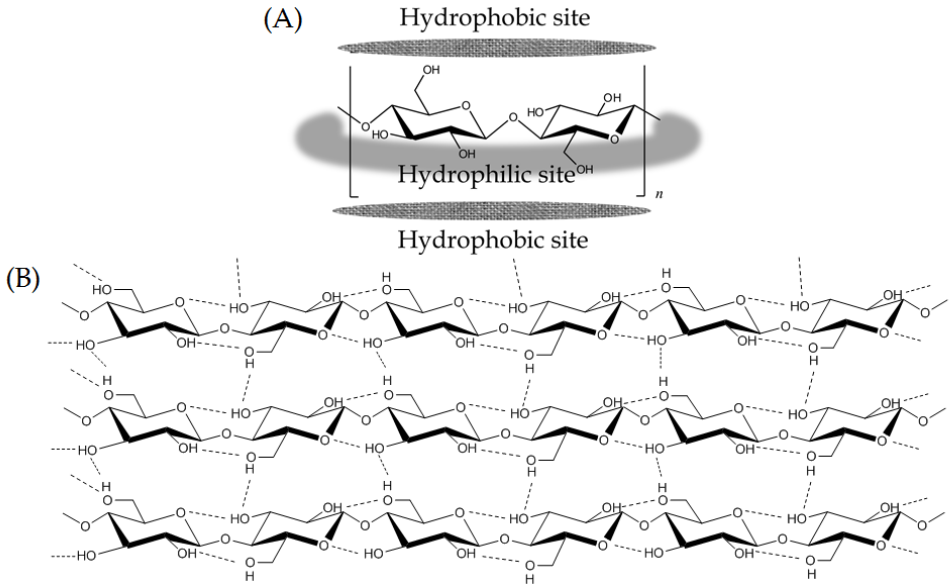

Figure 1-5. The intra-sheet hydrogen bonding network in cellulose I_α and the resulting hydrophilic and hydrophobic face of the ring plane.
Adapted from Xi, 2013. (A) Hydrophilic and hydrophobic faces of the ring plane, and (B) schematic drawing of the intra-sheet hydrogen-bonding network in cellulose I_α.[12]

There are four major polymorphs of cellulose: cellulose I, II, III, and IV. In nature, cellulose exists in the crystalline form, cellulose I, with high resistance and in the amorphous form in less ordered regions. Cellulose I, with high crystallinity, can be isolated from native cellulose through chemical or enzymatic treatment[18]. Cellulose I exists in two allomorphs, i.e., I_α and I_β. Bacteria and algae are rich in cellulose I_α, and higher plants mainly contain cellulose I_β[19]. Both of their chains are aligned in parallel with the same growth direction[20–22]. With the exception of cellulose I, other polymorphs, namely, cellulose II, cellulose III, and cellulose IV, can be transformed through thermochemical treatments of cellulose I. The regeneration of the cellulose solution and mercerization of cellulose I are two ways to obtain the crystalline form cellulose II. Regeneration involves either preparing a solution of cellulose in an appropriate solvent or preparing an intermediate derivative followed by coagulation and recrystallization. Mercerization involves intracrystalline swelling of cellulose in concentrated aqueous NaOH followed by washing and recrystallization. Treatment of cellulose I and cellulose II with liquid ammonia transforms the forms to cellulose III[12] and further heating in glycerol transforms the forms to cellulose IV[23,24]. The hydrolysis rates of different forms of cellulose are influenced by chain packing. The hydrolysis rates can be arranged in decreasing order as follows: amorphous cellulose > cellulose III > cellulose IV > cellulose II > cellulose I[25–28].

Projections of visualizations of the chains arranged in parallel in cellulose I_β and cellulose II are shown in Figure 1-6. Crystal structures proposed for cellulose I_α and cellulose II are compared in Table 1-1.

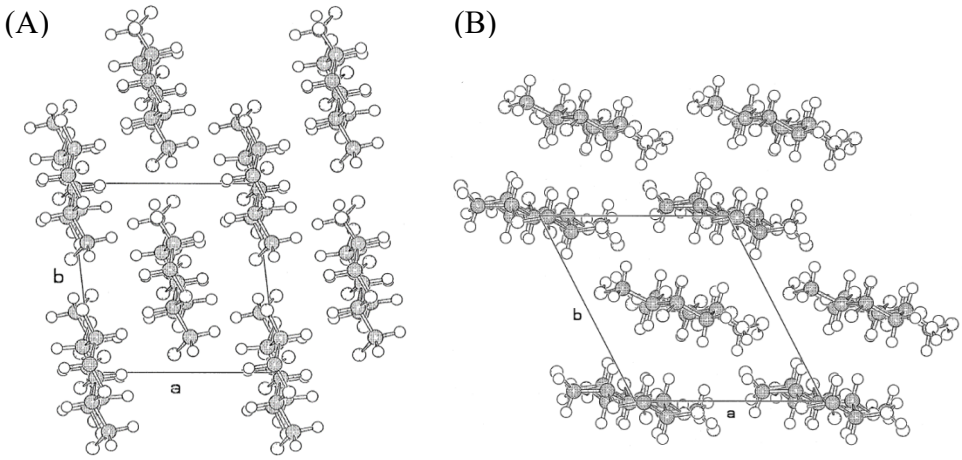

Figure 1-6. Representation of the model of cellulose I_β (A) and cellulose II (B) onto the a-b plane. Adapted from Zugenmaier (2001).[24]

Table 1-1. Comparison of crystal structures of common cellulose allomorphs.

Type	Unit cell	Chains	Repeat distance (Å)	Asymmetric
I_α	One-chain triclinic	Parallel	~10.35	Two glucosyl
I_β	Two-chain monoclinic	Parallel	~10.35	Two glucosyl
II	Two-chain monoclinic	Antiparallel	~10.35	Two glucosyl

Numerous research has focused on the crystal structure, morphology, properties, and hydrolysis behaviors of cellulose. The different intra- and intermolecular hydrogen bonding network of cellulose I and cellulose II influence the crystal structure. The I_β form is found mostly in lignocellulosic biomass derived from the cell walls of higher plants. In the cellulose I_β allomorph, there is an inherent organization of the intermolecular H-bonding network that maintains the cellulose chains in sheets and high crystallinity[22]. Within a cellulose I_β sheet, there are intramolecular hydrogen bonds O3–H···O5, O2–H···O6, O2–H···O1, O6–H···O2, and O6–H···O1, and intermolecular hydrogen bonds O6–H···O3, O6–H···O2, and O2–H···O6[22]. However, there is no indication of intersheet O-H···O hydrogen bonds (Figure 1-7). The cellulose sheets are accumulated by weak C–

H···O hydrogen bonds and van der Waals forces[22]. The crystal structure of regenerated cellulose II was first determined in the same year independently by Kolpak and Blackwell[29] and Stipanovik and Sarko[30] with X-ray diffraction. The crystal structure of cellulose II is formed by an array of antiparallel chain molecules and a three-dimensional network of both intralayer and interlayer hydrogen bonding[29,31]. The intramolecular hydrogen bonds are O3–H···O5 and O2–H···O6, as well as intermolecular hydrogen bonds of O2–H···O2, O6–H···O3, O3–H···O6, and O6–H···O2[30,32]. On a separate note, O2–H···O2 exists as an intermolecular intersheet hydrogen bond[29] (Figure 1-8).

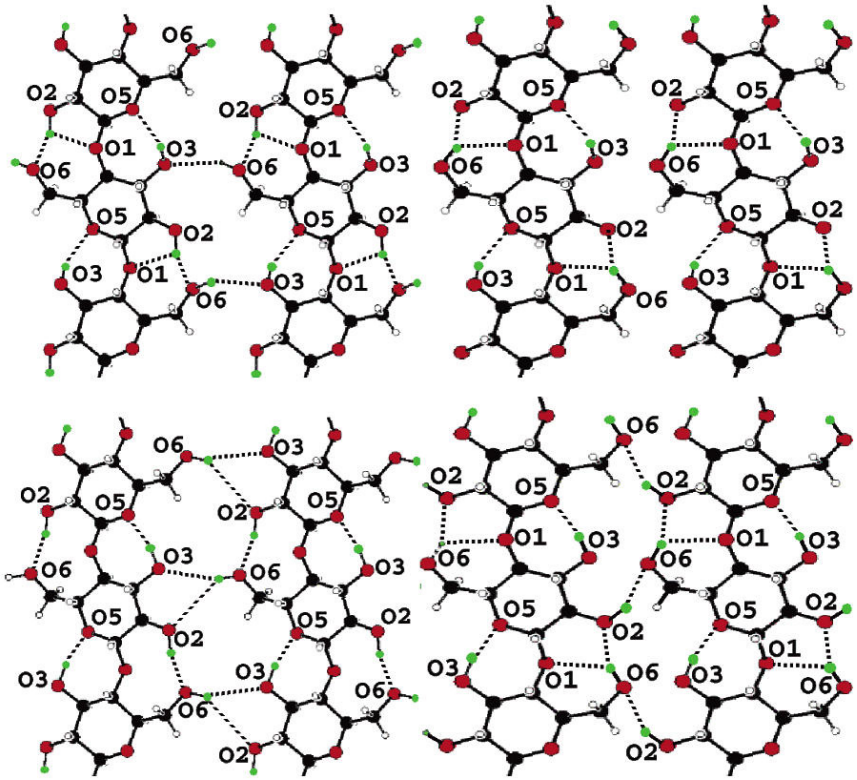

Figure 1-7. Schematic representation of the hydrogen bonds in the origin (top) and center (bottom) sheets of cellulose I_{β}.

Adapted from Nishiyama (2002). Carbon, oxygen, hydrogen, and deuterium atoms are colored black, red, white, and green, respectively. Hydrogen bonds are represented by dotted lines. Only oxygen atoms involved in hydrogen bonding have been labeled for clarity.[21]

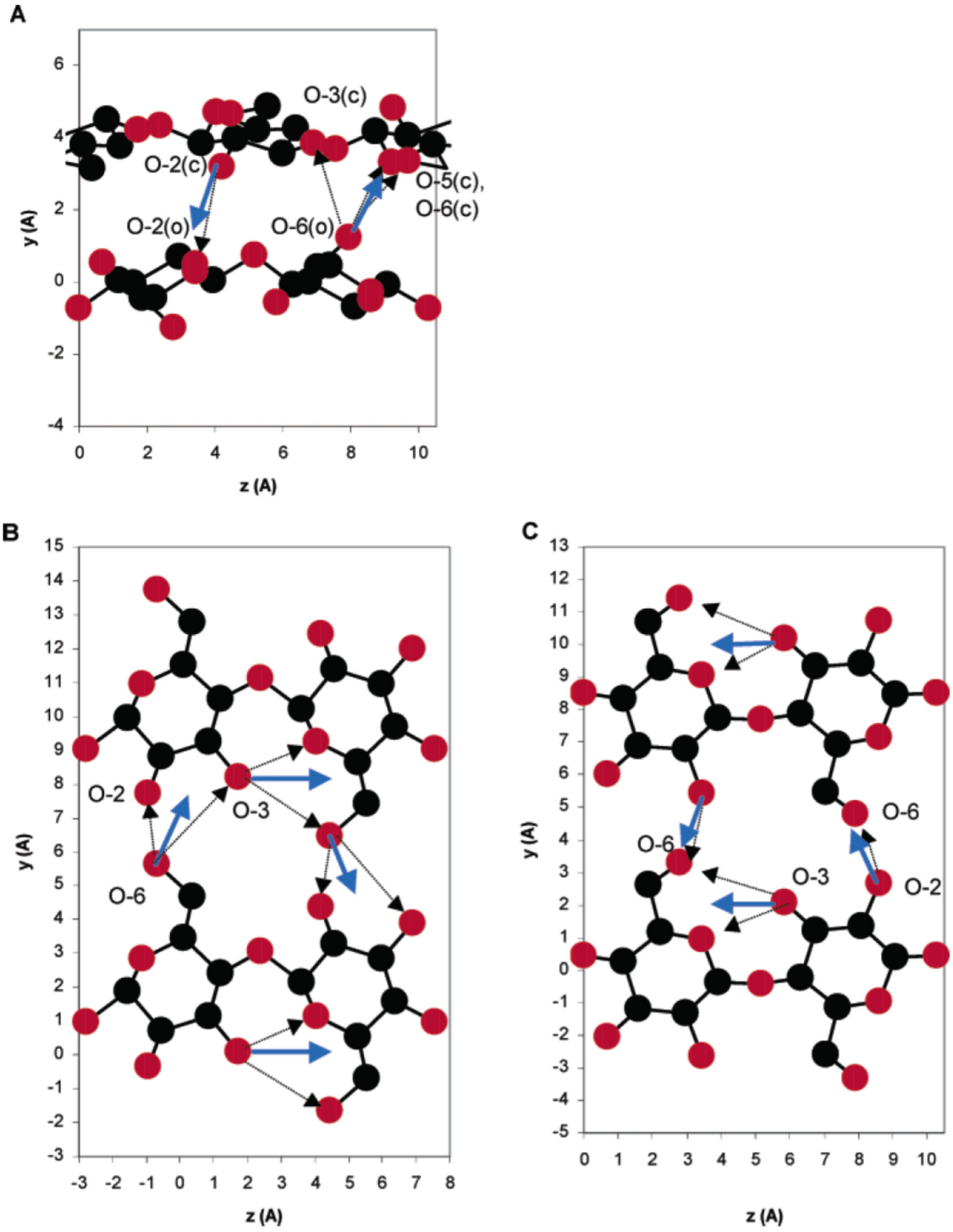

Figure 1-8. Hydrogen-bonding pattern in cellulose II.
Adapted from Šturcová (2003). (A) Intersheet hydrogen bonding; (B) intra- and intermolecular hydrogen bonding within the origin sheet of chains; (C) intra- and intermolecular hydrogen bonding within the center sheet of chains.[33,34]

1.2.2 Lignin

The recalcitrance of biomass materials is largely due to lignin components. Lignin, following cellulose, is one of the most abundant organic polymers in plants. The content of lignin in wood is 20–40%. The term refers to a group of polymeric substances derived from phenylpropene units that are nonlinearly and randomly linked. There are three main types of lignin based on the three most common monomers: coumaryl alcohol, coniferyl alcohol, and sinapyl alcohol (Figure 1-9).

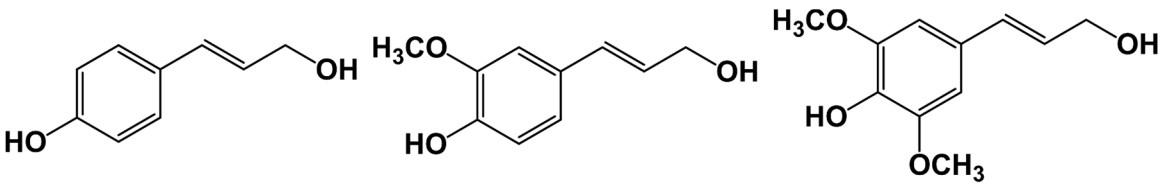

Coumaryl alcohol Coniferyl alcohol Sinapyl alcohol

Figure 1-9. The basic unit structure of lignin.

Lignin presents both physical and chemical barriers to the enzymatic hydrolysis of cellulosic biomass[35]. In the matrix of the plant cell wall, cellulose microfibrils are embedded in lignin (Figure 1-1). To allow the exposure of cellulose to cellulases, it is critical to remove the lignin components. Another mechanism for lignin in limiting the access of cellulases to cellulose is the nonproductive binding of cellulase to lignin[36–40]. Therefore, lignin is the main barrier to biofuel production and pretreatment processes are being developed to break down cell walls into intermediates, removing lignin to allow the exposure of cellulose to cellulase[11].

1.2.3 Hemicellulose

In the plant cell wall, cellulose microfibrils are coated with other polysaccharides, such as hemicellulose or xyloglucans (Figure. 1-1). Depending on the species, 20–40% of the plant cell wall content is hemicellulose. This has an amorphous structure with little mechanical strength compared to cellulose. Like lignin, hemicellulose can also hinder the enzymatic hydrolysis of cellulose by limiting the access of cellulase to cellulose. Moreover, hemicellulose can remain coated on the cellulose microfibrils or bound to cellulose after pretreatment.

1.3 Enzymatic Hydrolysis of Cellulosic Substrates

Cellulase, like all glycosyl hydrolase enzymes found in fungi, bacteria, plants, and some invertebrates, can break down the β-1, 4-glycosidic bonds of cellulose through general acid/base catalysis[41–48]. There are three main kinds of cellulase: endo-β-1, 4-glucanases, exo-β-1, 4-D-glucanases, and β-D-glucosidases (Figure 1-10)[43,48–52]. Each cellulase type alone cannot hydrolyze the crystalline cellulose efficiently, but working synergistically with other types of cellulase, can significantly increase the rate of hydrolysis[53].

Endo-β-1, 4-glucanase breaks internal glycosidic bonds of individual cellulose chains to disrupt the structure of cellulose and expose individual polysaccharide chains.

Exo-β-1, 4-D-glucanase can access a single cellulose chain from the exposed reducing or non-reducing end and cut 2to 4 glucose units at a time to produce tetrasaccharide (i.e., tetraose) or disaccharide (i.e., cellobiose).

Cellobiase or β-D-glucosidase hydrolyzes cellobiose to release D-glucose units.

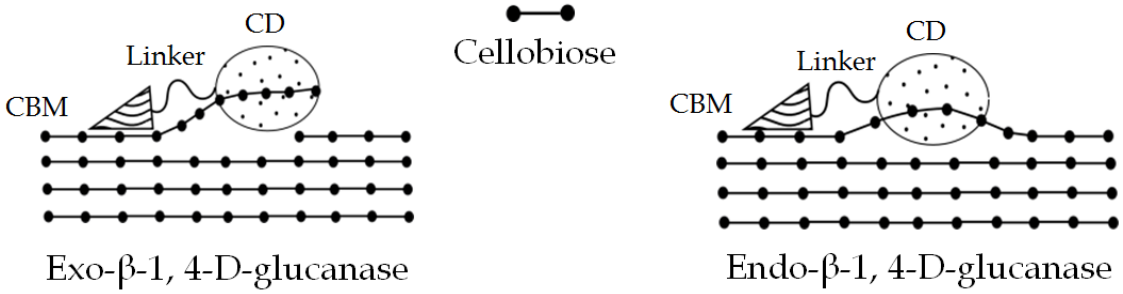

Figure 1-10. Schematic illustration of the hydrolysis of cellulose by various types of cellulases[12]. Adapted from Xi, 2013.[12]

Most fungal cellulases have two domains in their structures, a catalytic domain (CD), and a carbohydrate binding module (CBM)[54]; see Figure 1-11. These domains are connected by a peptide linker known to maintain separation between the CD and the CBM[12]. The CBM is a contiguous amino acid sequence within cellulase that anchors the CD onto the surface of cellulose through van der Waals interactions and hydrogen bonding[55,56]. Cellulases can be grouped into families according to sequence similarities of their amino acid residues within CDs and CBMs.

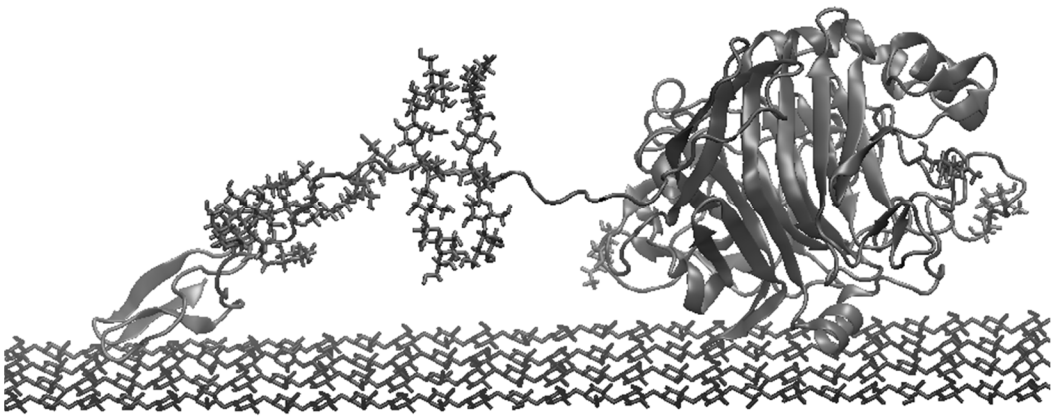

Figure 1-11. The domain-like structure of the cellulase (CBH I) bound to cellulose I_β microfibril. Adapted from Zhong, 2008.[57]

There are several steps for cellulolytic hydrolysis by the cellulase enzyme on the cellulose substrate, shown in Figure 1-12. First, the CBM binds to the cellulose and then lead CD to be close to the cellulose crystal. The cellulase-substrate complex is formed in this *initial binding* step. Then, a single cellulose chain is separated from the cellulose crystal by cellulase and led to the active site of a cellulase. This step is the *decrystallization* step. A pseudo-Michaelis complex is the product of this step. The pseudo-Michaelis complex then undergoes hydrolytic cleavage to produce cellobiose. Finally, the cellulase dissociates from the substrate and is released from the chain.

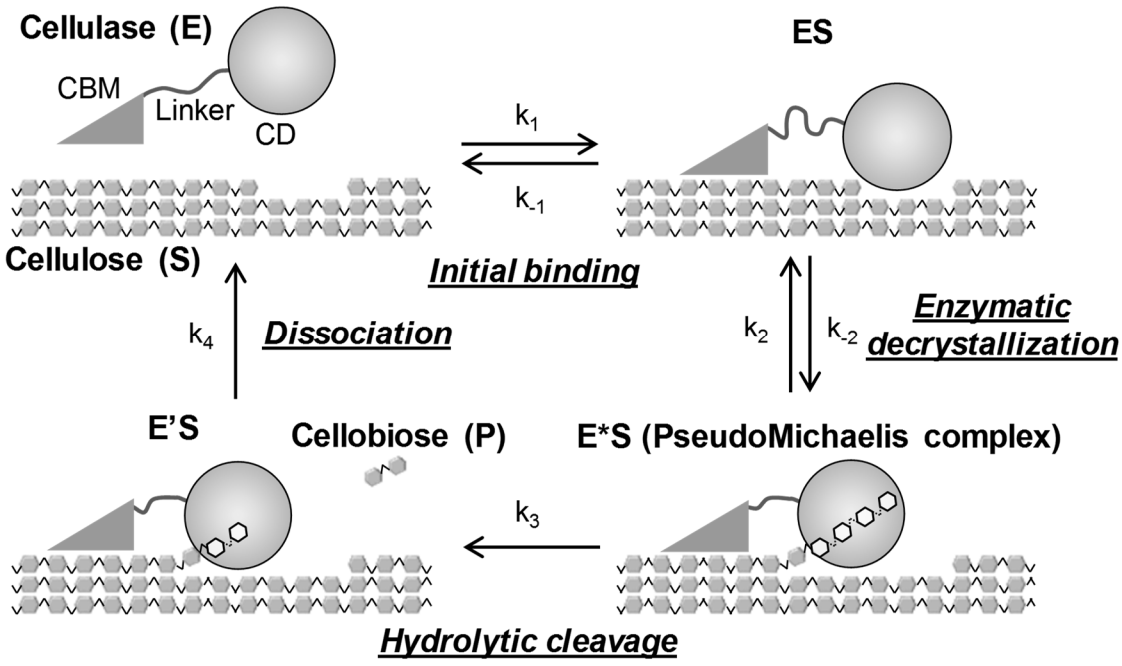

Figure 1-12. Mechanistic model of cellulose hydrolysis by cellulase.
The carbohydrate binding module (CBM) of a cellulase (E) anchors the cellulase onto the surface of cellulose (S). The surface-bound cellulase (ES), then extracts a glucan chain to form a pseudo-Michaelis complex (E*S), which undergoes hydrolytic cleavage to afford the hydrolysis product (P).[12]

For cellulose hydrolysis, the substrate cellulose is water insoluble and the solid aggregate of cellulose fibers is resistant to biological attack. The inaccessibility of a single cellulose chain for cellulase makes the formation of a Michaelis-complex before hydrolytic cleavage harder than when compared to enzymatic reactions involving soluble substrates.

1.4 Cellulosic Biomass Recalcitrance

Cellulosic biomass is a source of biofuel which is the most promising and sustainable alternative energy source to fossil fuels. However, an economically feasible biomass-to-biofuel conversion method has not yet been developed. The deconstruction of cellulosic biomass followed by enzymatic hydrolysis to produce fermentable sugars is a primary method of biofuel production. Nevertheless, the lack of an efficient and profitable cell-wall degrading technique or enzyme continues to be a major obstacle preventing the commercialization of a biologically-based lignocellulosic biomass conversion process.

Plant biomass has developed complex structural and chemical mechanisms for resisting attacks on its structural sugars from the microbial and animal kingdoms[58]. This dissertation considers the natural resistance of plant cell walls to microbial and enzymatic deconstruction, collectively known as *biomass recalcitrance*.

Biomass recalcitrance typically arises from the following aspects: epidermal tissues, chemical compositions, the physical structure of the plant cell wall, the cellulose structure, and pretreatment-induced effects (Figure 1-13). Himmel and colleagues have summarized the natural factors contributing to the recalcitrant nature of cellulosic biomass against physical, chemical, and enzymatic degradation, to include[58–60]: (i) the

epidermal tissues of the plant, particularly the cuticle and epicuticular waxes; (ii) the relative amount of sclerenchymatous (thick wall) tissue; (iii) the arrangement and density of vascular bundles; (iv) the degree of lignification[61,62]; (v) the physical heterogeneity and complexity of cell-wall structures, such as microfibrils and matrix polymers[63]; (vi) the challenges for enzymes acting on an insoluble substrate[64]; and (vii) the inhibitors to subsequent fermentations that naturally exist in cell walls or are generated during the conversion processes[65]. Plant wall cells vary in the levels of degradation simplicity. For example, a vascular tissue cell is most resistant to microbial degradation while a parenchyma cell is more vulnerable to degradation[66]. Additionally, cellulose crystallinity and the presence of other inhibitors to enzymatic hydrolysis, such as cell wall proteins and uronic acid, also cause the recalcitrance of cellulosic biomass. Furthermore, during processes of pretreatment of cellulosic biomass, some structural changes may contribute to a lesser extent to recalcitrance, such as the collapse of the vascular structure of plant wall cells and reannealing of cellulose — hornification[59].

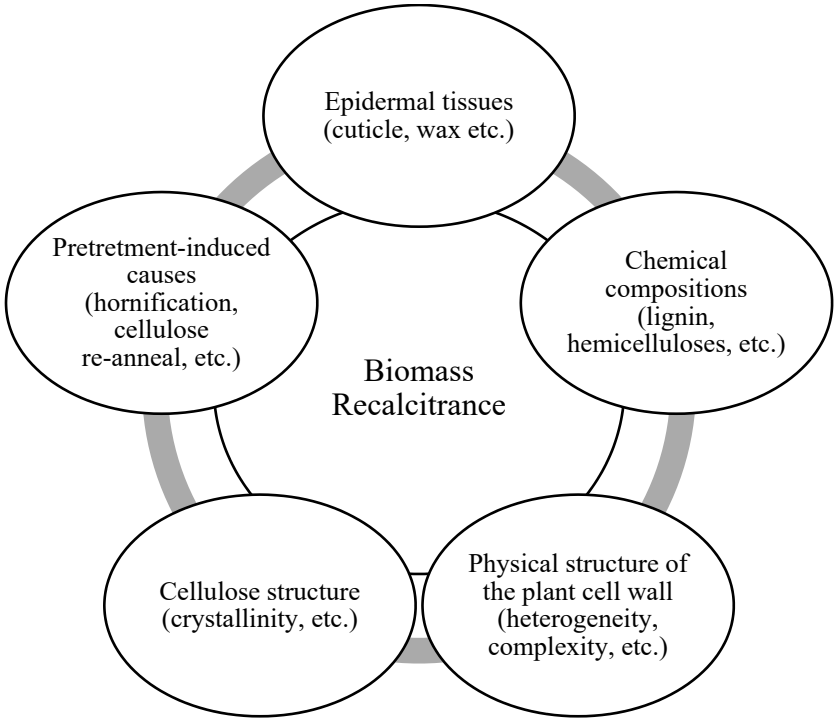

Figure 1-13. Factors constructing biomass recalcitrance.

1.5 Objectives

Enzymatic hydrolysis of cellulose by cellulase is assumed to consist three major steps, i.e., initial binding, decrystallization, and hydrolytic cleavage. Currently, the mechanism for the decrystallization has not yet been elucidated, though it is speculated to be the rate-limiting step of the overall enzymatic function. A major technical challenge to the understanding of the decrystallization is the lack of an effective experimental approach for examining the decrystallization. It is assumed that decrystallization occurs on the surface of solid cellulose and it facilitated by cellulase. Thus, the primary goal of the current study is to develop an experimental approach for assessing the decrystallization activity in real time and to provide experimental evidence for decrystallization.

To achieve these objectives, a cellulose film having a controlled level of physical properties, including thickness, roughness, and crystallinity was developed. Spin coating of a cellulose solution was used to prepare the film. In addition, nanoparticles consisting one to three layers of cellulose molecules was prepared on mica.

An atomic force microscope (AFM) was employed to study the surface topography by measuring the surface roughness of the cellulose film. AFM was also utilized to examine the height of cellulose nanoparticles. X-ray diffraction (XRD) was applied to investigate the crystallinity of cellulose film.

Two forms of cellulase, active cellulase and inactive cellulase, were used in this study. The inactive celluase is made non-hydrolytic by action of a paladium complex. Bovine serum albumin (BSA), which has similar size and mass as cellulase, was used as a blank protein.

1.6 Organization

The current dissertation has seven chapters. Chapter 1 serves as an introduction, detailing background information, including cellulose, cellulase, cellulosic biofuels, and the objectives of the dissertation. Chapter 2 introduces research techniques used in the current dissertation. Chapter 3 describes the use of a nanomechanical sensor (i.e., microcantilever) to probe the interaction between cellulase and cellulose and presents the first experimental evidence of the decrystallization. Chapter 4 describes the study of the cellulase–cellulose interaction based on topography changes during enzymatic hydrolysis, providing further experimental proof of the decrystallization. Chapter 5 presents a study on the interaction between water molecules and cellulose molecule chains (with the cellulose bilayer nanoparticles as a model substrate). Dr. Linghao Zhong

provides the results of computational calculation. Chapter 6 is a published manuscript, and to the best of the current study's knowledge, it reports one of the few studies that utilized a microcantilever nanomechanical sensor to study the mechanical properties of cells. Chapter 7 summarizes the dissertation and discusses the important contribution of the findings, as well as future plans.

Chapter 2: Research Methods

2.1 Atomic Force Microscopy (AFM)

2.1.1 Principles

Atomic force microscopy is a type of scanning probe microscopy (SPM) with high resolution, used to measure surface properties. The scanning tunneling microscope (STM), a precursor to AFM, was developed by Gerd Binnig and Heinrich Rohrer in 1981 at IBM Research, in Zurich, Switzerland. It was the first instrument capable of directly obtaining three-dimensional images of a solid surface at an atomic resolution. Binnig and Rohrer received a Nobel Prize in Physics in 1986 "for their design of the scanning tunneling microscope"[67]. In 1986, based on the design of the STM, Binnig and his colleagues developed the first AFM to measure ultra-small forces (less than 1 μN) between the AFM tip and the sample surface[68–70]. The first commercially available AFM was introduced in 1989 and has become a popular surface profiler for topographic and force measurements on the micro-nano scale[71]. Unlike the STM, which can only be used to study an electrically conductive surface, the AFM can be used to measure any surface, including electrically conductive and insulating surfaces. The AFM probes the topography of the surface of a sample with an ultra small tip located at the free end of a flexible microcantilever beam with a low spring constant (lower than the forces bonding the atoms of the sample surface). It is flexible enough that even van der Waals and coulombic interactions between the microcantilever tip and atoms of the sample's surface bend the microcantilever[72]. The microcantilever, as shown in Figure 2-1, can experience two types of interactions (Lennard-Jones potential): 1) repulsion: if the tip is close enough to the sample surface, the force between the tip and sample will be repulsive,

typically short-range coulombic interactions; 2) attraction: if the distance between the tip and the sample surface increases, the force between them will be an attractive, typically van der Waals interaction. If the distance continues to grow, they will be separated and the microcantilever will experience no force[73]. The force experienced by the microcantilever will make the microcantilever bend according to Hooke's law.

Moreover, the deflection of the microcantilever can be detected by a laser which reflects from the microcantilever to a photodiode. The combination of this deflection signal and the position of the tip on the sample's surface provides information about the surface topography. The working scheme is shown in Figure 2-2. A three-dimensional surface profile will be given by AFM. With this powerful tool for surface imaging, it is possible to investigate surface changes within a chemical or physical process.

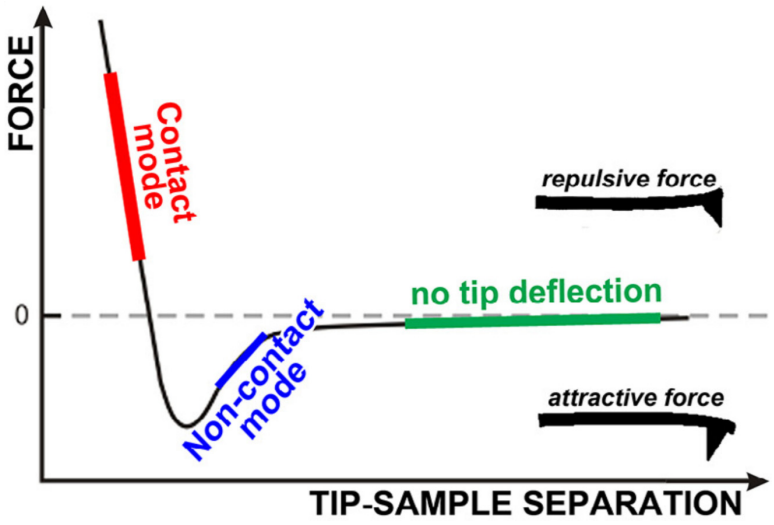

Figure 2-1. Force-distance relation of atomic force microscope (AFM) microcantilever.[74] Adapted from Maver, 2016.[74]

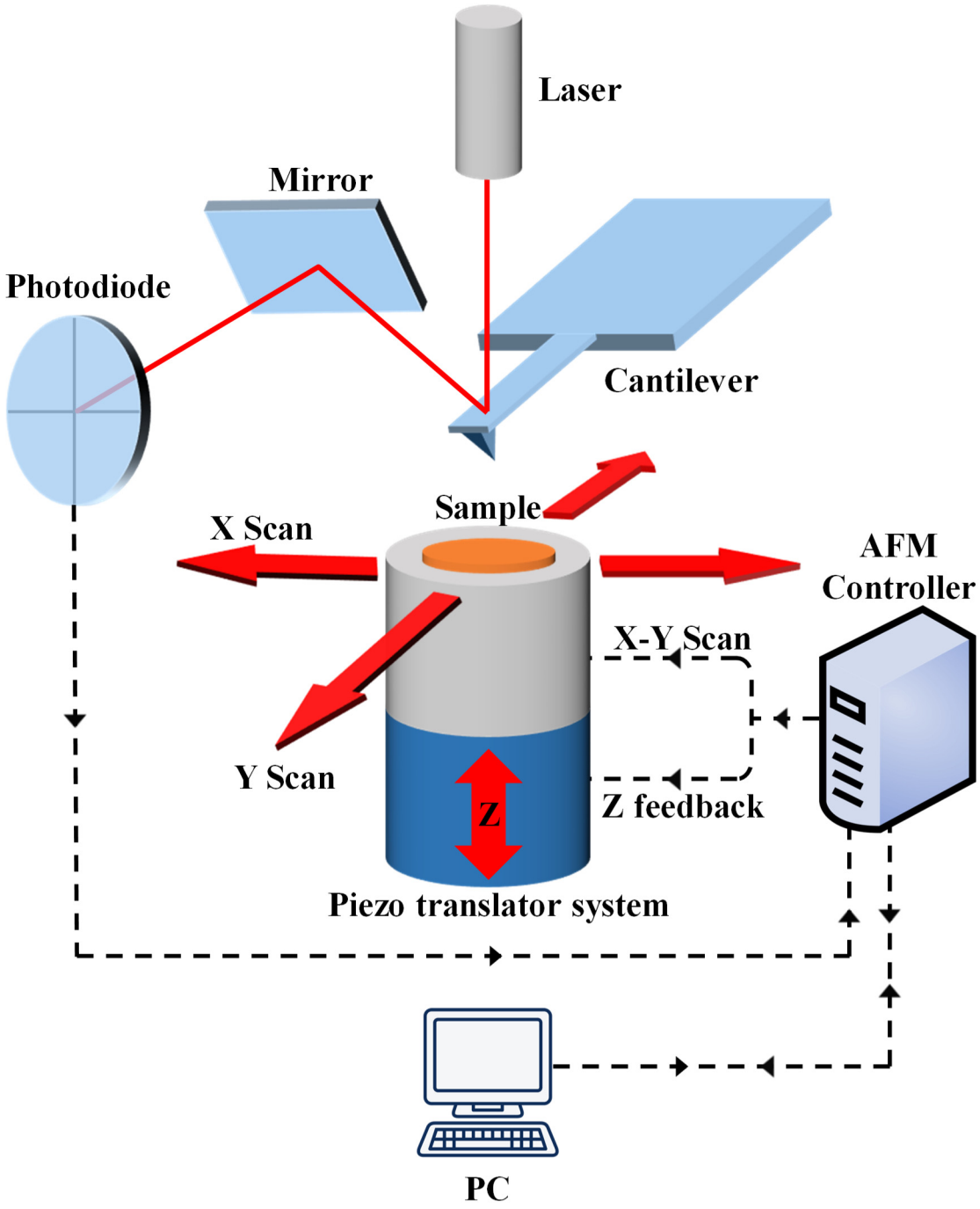

Figure 2-2. Simplified diagram of a generic AFM instrument.

2.1.2 Instrument Configuration

A typical AFM instrument includes the following components (see Figure 2-2).

1) A piezo translator system (piezoelectric tube) which moves the sample under the stationary tip (for small samples, as shown in Figure 2-2) or scans the tip over the sample (for large samples, not shown). The piezoelectric tube scanner can generate sub-Ångstrom motion increments.

2) A flexible microcantilever with a sharp tip secured to the AFM scanner head. The force between the tip and sample is small (less than 10^{-9} N). The microcantilever is usually made from silicon which has a small spring constant.

3) A probe detection system, including a photodiode and electronics, measures the deflection of the microcantilever and feeds this signal to the AFM controller.

4) The AFM controller unit communicates with the computer, scanning system, and probe detector. It provides the voltage to drive the scanner, receives signals from the detector, contains the feedback system to maintain either the deflection (force) or the height of the piezo constant during scanning, retrieves commands from the computer, and feeds all information back to the computer to draw a three-dimensional image.

5) The computer controls all the instruments and completes data processing, image building, analysis, and display.

6) Other components include a vibration isolation table, an optical microscope for sample monitoring and laser alignment, and a thermal block to heat the sample to 50°C.

2.1.3 Functions of AFMs and Working Modes

The AFM has three major functions: surface topographic imaging, force measurement, and manipulation. For force measurement, the AFM can be used to measure the force between the tip and the sample as a function of their distance. For manipulation, this force can be utilized to manipulate the sample in a controlled manner. For surface imaging, there are three primary modes: contact, tapping, and non-contact.

2.1.3.1 Contact (repulsive) Mode

Contact mode is the original and the first operational mode of the AFM. The tip is placed in constant contact with the sample. As the probe slides softly across the sample surface, the contact force causes the microcantilever to bend to accommodate changes in the topography. There are two working modes for contact mode: constant deflection and variable-deflection (constant height). In constant deflection, the contact mode feedback loop maintains the deflection of the microcantilever at a setpoint value by vertically adjusting the scanner. The adjustment of the scanner is displayed as AFM data. By maintaining a constant deflection, the force between the tip and the sample remains constant. The ability to track the surface in this manner is limited by the feedback circuit and scanner. However, in variable-deflection (constant height), the tip is allowed to scan without height adjustment from the scanner and the microcantilever deflection, which changes along with the surface topography, is measured. It is the deflection of the microcantilever that is displayed as data. Constant height mode is extremely useful for high-speed AFM scans, but the sample must be relatively flat and small for the feedback loop to maintain control during scanning.

Because the tip is in firm contact with the surface, the stiffness of the microcantilever must be less than the effective spring constant holding atoms together, around the order of 1–10 nN/nm. Thus, most microcantilevers used for the contact mode have a spring constant less than 1 N/m. The advantages of contact mode are its higher scan speeds, the ability to obtain atomic resolution images, and it is more user-friendly for rough samples. Disadvantages include that the lateral (shear) forces can distort features in the images, capillary forces from the adsorbed fluid layer on the sample surface may significantly influence the interaction force, and the combination of these aspects may damage the sample surface and more easily wear out the microcantilever.

2.1.3.2 Tapping Mode

Tapping mode, also referred to as intermittent-contact or Dynamic Force Mode (DFM), is the most commonly used of all AFM modes. It is a patented technique from Bruker (TappingMode™).

In an ambient environment, most samples develop a liquid layer on the surface. The tip tends to stick to the surface because of capillary forces between this layer and the probe. To prevent this effect while keeping the tip close to the surface for imaging, tapping mode was developed. In tapping mode, a stiff microcantilever oscillates close to the sample at its resonance frequency (~50–500 kHz) and part of this oscillation extends into the repulsive regime. The oscillation amplitude changes with the sample surface topography and there is a vertical feedback loop minimizing this change. By monitoring the amplitude change and the vertical loop feedback, topographic 3D images can be plotted.

An advantage of tapping mode is that it can eliminate lateral forces that damage samples and reduce image resolution and allow imaging samples that are considered impossible to image with other working modes of AFM. Because of the gentle tapping behavior of the microcantilever on the sample surface with the tapping mode, there are lower forces and less damage to soft samples. With proper scanning parameters, the conformation of single molecules can remain unchanged for hours during scanning. However, because of the nature of the tapping movement, the scan rate is slower than contact mode.

Another advantage of tapping mode is the ability to obtain phase images. The phase of the microcantilever's oscillation can provide information about energy dissipation when the microcantilever taps on the sample, containing details about the stiffness or adhesion properties of a sampling area. Tapping mode can thus be particularly useful for studying samples whose parts have different mechanical properties, like block polymers or biological materials.

2.1.3.3 Non-contact (attractive) Mode

In non-contact mode, the tip of the microcantilever does not contact the sample surface. Rather, it oscillates at its resonance frequency near the surface, above the adsorbed fluid layer in the ambient environment. The interaction force between the probe and the sample is within the attractive region (typically van der Waals interactions). This interaction decreases the oscillation frequency of the microcantilever. A feedback loop system monitors this decrease in oscillation frequency and adjusts the tip-to-sample distance to maintain a constant oscillation amplitude or frequency. By measuring this

distance across the entire sample surface, the scanning software can construct a topographic image.

The most significant advantage of non-contact mode is that there is no tip or sample degradation because there is no force exerted on the sample surface. However, the technique has some disadvantages limiting its application, including a lower resolution from the tip-sample separation, a slower scan rate to avoid contacting the adsorbed fluid layer, and it also requires extremely hydrophobic samples to minimize the thickness of the adsorbed fluid layer.

2.1.3.4 Other Operational Modes

There are additional operational modes of AFM. Lateral force microscopy (LFM) measures frictional forces between the probe and the surface. Laterally moving the tip on the sample surface creates a lateral force that will "twist" the microcantilever. By measuring the level of twisting instead of bending, it is possible to qualitatively distinguish areas with higher friction from smoother areas. Magnetic force microscopy (MFM) registers the magnetic force gradient and distribution above a sample's surface by means of a microcantilever coated with a ferromagnetic thin film in non-contact mode. Electrostatic force microscopy (EFM) applies voltage between the probe and the surface, thus, the microcantilever deflects when scanning over static surface charges in non-contact mode, and the electric field gradient and distribution can be mapped. There are other operational modes, including, but not limited to, scanning capacitance microscopy (SCM), scanning electrical potential microscopy (SEPM), magneto-resistive sensitivity mapping (MSM), and chemical force microscopy (CFM).

Most of the methods register the bending of the microcantilever as voltage: the experimenter, using a calibration factor and the microcantilever's spring constant computes the force between the tip and the sample, the force at each point on the scanned area is used to generate a three-dimensional image of the surface. These techniques all belong to surface probe microscopy (SPM).

2.1.4 Advantages and Disadvantages of AFM

The AFM has several advantages over the scanning electron microscope (SEM), transmission electron microscopy (TEM), and the scanning tunneling microscope (STM). Compared to electron microscopes, including SEM and TEM, the AFM can provide a three-dimensional, rather than a two-dimensional image. Also, the sample for AFM imaging does not require special treatment (such as metal coating, specimen sectioning, or positive staining), which may damage samples and alter surface properties. The working conditions for AFM are also more feasible. The process can be completed in a vacuum, air, or even liquid environment. The SEM or TEM requires an expensive vacuum environment for proper operation. Thus, it is possible for AFM to study materials at their working temperature and pressure, biological macromolecules in their proper buffer, and even *in vivo* specimens. Compared to the STM, the AFM does not require the sample to be conductive, significantly broadening its applications.

The AFM also has several disadvantages. Because of the way it probes the sample, the tip must image the entire imaging area point by point. The scan size is small and the scan rate slow. A common, commercial AFM instrument can only produce an image smaller than 15 × 15 μm with a resolution less than 512 × 512, and it may require up to 20 minutes to scan one image of this size and resolution. Also, AFM images need to

be flattened before analysis, due to the nonlinearity, hysteresis, and creep of piezoelectric materials. The larger the scan size, the more flattening require. Moreover, because imaging by AFM depends on a sharp microcantilever tip, there is the possibility of image artifacts. Some of these disadvantages can be overcome by the use of a sharp tip, programming software with better correction algorithms, and deploying a fast-acting design.

2.2 Nanomechanical Microcantilever Sensor

2.2.1 Introduction

Sensors are devices that transform one form of energy or response into another form, detecting the signal produced during this transition. These sensors include, but are not limited to, electrochemical, electroacoustic, photoelectric, electromagnetic, magnetic, thermoelectric, and electrical. A mechanical sensor responds to changes in an external parameter, such as temperature or molecule adsorption, through a mechanical response[75]. Mechanical sensors consist of two parts: a fixed and a movable part. The movable part can be a thin membrane, plate, or beam, fixed at one end or both ends. One common mechanical sensor is a microcantilever. It has a flexible beam fixed on a substrate (Figure 2-3). When used as probes for AFM imaging, there is a sharp tip on the free end of the flexible beam. The fabrication of small microcantilevers takes advantages of developments in silicon micromachining techniques developed for integrated circuit (IC) process technology. They are typically made of silicon, silicon oxide, or silicon nitride, and are commercially available in different shapes, dimensions, and spring constants. The first report to use cantilever-like beams as a sensor was published by Wilfinger *et al.* in 1968[76]. The size of the silicon microcantilever used to detect resonances was about 5 × 3

× 0.8 cm, quite large compared to cantilevers currently manufactured. Their study already contained basic concepts for use of a microcantilever as a sensor, as well as applying piezoelectricity to stimulate the microcantilever. In the following decades, due to limitations of manufacturing techniques, there were only a few reports related to microcantilever sensors[77,78].

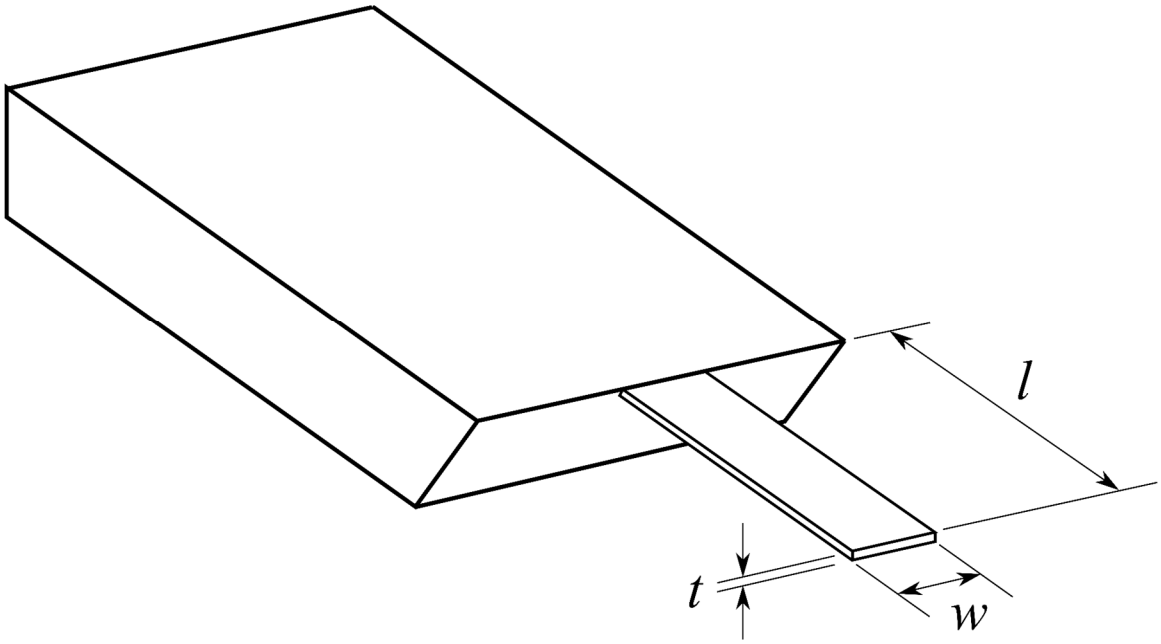

Figure 2-3. Schematic of a microcantilever, including a rigid substrate and a tip. The dimension of tip: *l* – Length, *w* – width, *t* – thickness.

2.2.2 Operational Modes of the Microcantilever

Similar to the AFM, the microcantilever as a sensor has various operating modes. Depending on whether the microcantilever oscillates while working as a sensor, the

modes can be divided into two categories: static and dynamic. Based on their applications, they can then be subdivided into nine main subcategories (Figure 2-4).

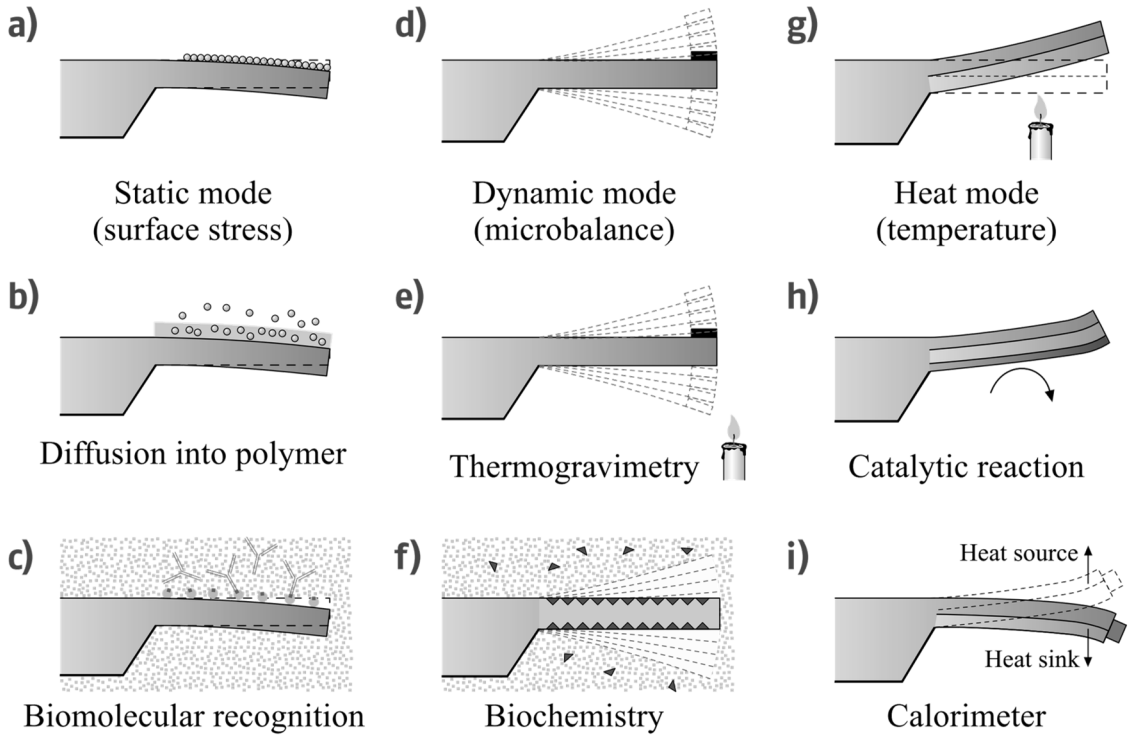

Figure 2-4. Basic microcantilever operation modes.[75]
Adapted from Bhushan, 2010. (a) Static bending of a microcantilever on adsorption of a molecular layer. (b) Diffusion of molecules into a polymer layer leads to swelling of the polymer and eventually to bending of the microcantilever. (c) Highly specific molecular recognition of biomolecules by receptors changes the surface stress on the upper surface of the microcantilever and results in bending. (d) Oscillation of the microcantilever at its resonance frequency (dynamic mode) allows information on mass changes taking place on the microcantilever surface to be obtained (application as a microbalance). (e) Changing the temperature while a sample is attached to the apex of the microcantilever allows information to be gathered on decomposition or oxidation processes. (f) Dynamic-mode measurements in liquids yield details on mass changes during biochemical processes. (g) In heat mode, a bimetallic microcantilever is employed. Here, bending is due to the difference in the thermal expansion coefficients of the two materials. (h) A bimetallic microcantilever with a catalytically active surface bends due to heat production during a catalytic reaction. (i) A tiny sample attached to the apex of the microcantilever is investigated, taking advantage of the bimetallic effect. Tracking deflection as a function of temperature allows the observation of phase transitions in the sample in a calorimeter mode.[75]

2.2.2.1 Static Mode

In static mode, the microcantilever does not oscillate but remains static. The top side of microcantilever is covered by an adhered layer. The microscopic change in geometry of the adhered layer (e.g. length or volume) can induce bending of the cantilever. If the adhered layer expands along the length of the microcantilever, the cantilever bends down. If the adhered layer shrinks along the length of the microcantilever, the cantilever bends up. The deflection on the microcantilever is perpendicular to its long axis.

The static mode can be operated in various environments, including air (Figure 2-4a and Figure 2-4b) and liquid (Figure 2-4c). For example, the top surface of microcantilever can be coated with a layer of gold (Figure 2-5). When this coated microcantilever is exposed to a vapor of alkylthiol molecules, spontaneous adsroption of these straight-chain thiol molecules occurs, and the microcantilever bends down[79,80]. Static mode can also be used in air on polymer films (Figure 2-4b). A wide range of polymers can be selected and the magnitude of response depends on the chosen polymer.

Static mode can also be used in liquids, even in biological buffers. It requires a specific sensing layer on the microcantilever based on molecular recognition response, such as antigen-antibody recognition and DNA hybridization[81–89] (Figure 2-4c). This response with a biochemically functionalized microcantilever is highly specific to biomolecules based on biomolecular key-lock principles of molecular recognition. Depending on biochemical interactions, the cantilever may bend either up or down The detection efficiency is pivotal for this type of application.

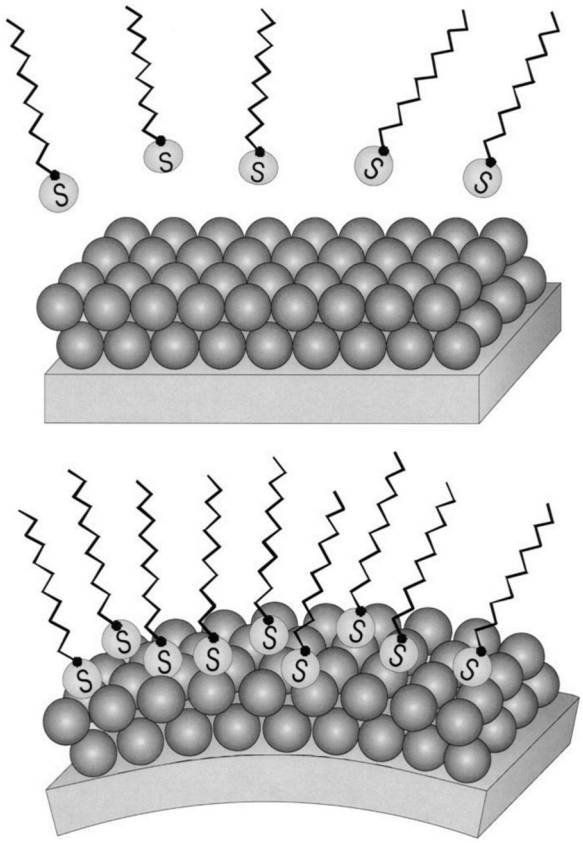

Figure 2-5. Schematic diagram of chemisorption of straight-chain thiol molecules on a gold coated microcantilever.
Adapted from Lavrik, 2004. Spontaneous adsorption processes are driven by an excess of interfacial free energy and accompanied by a reduction of interfacial stress[90].

2.2.2.2 Dynamic Mode

When the microcantilever oscillates at its resonance frequency, the mass change can be accurately determined by the frequency change. Owing to the addition of mass on the microcantilever surface, the microcantilever oscillates at a lower frequency from damping effects (Figure 2-4d). The mass change is calculated from the frequency shift as follows[91]:

$$\Delta m = \frac{k}{4\pi^2} \times \left(\frac{1}{f_1^2} - \frac{1}{f_0^2}\right) \quad 2\text{-}3$$

where Δm is the mass change of the microcantilever, f_0 and f_1 are the frequencies before and after the mass change occurs, respectively, and k is the spring constant of the microcantilever.

Similar to the static mode, the dynamic mode can operate in various environments and at a variety of temperatures (Figure 2-4d, e, f). The simplest and most sensitive setup in dynamic mode operates in air. In air, the resonance frequency can be easily determined with a resolution below 1 Hz. In a liquid, because of the damping of the oscillation due to the viscosity of the surrounding medium, the sensitivity is lower (with a resolution of about 20 Hz). However, it is still an efficient method for studying the adsorption of targeted molecules, especially biomolecules (Figure 2-4f). In dynamic mode, the microcantilever can also be used as a micromechanical thermo-gravimeter. When the test sample is bound to the surface by the end of the microcantilever while it is oscillating, the mass change of the test sample due to thermal treatment can change the oscillating frequency of the microcantilever. It is sensitive due to the small sample size (less than several hundred nanograms), and even a mass modification in the range of a picogram can be detected in real time[92].

2.2.2.3 Other Operational Modes

There are further operational modes of the microcantilever sensor, including but not limited to heat (Figure 2-4g, h, i), photothermal spectroscopy, electrochemistry, electrostatic, and magnetic forces detector modes[93–96]. In heat mode, the microcantilever consists of two different materials with different thermal expansion coefficients. Thus, it

bends when it absorbs heat. For photothermal spectroscopy, it employs a similar microcantilever-like heat mode but is heated by photons from light. In electrochemistry mode, the microcantilever is coated with a metallic electrode. During the electrochemical processes, the transfer of ions between the electrolyte and electrode can produce surface stress and electrostatic forces, in turn producing observable bending of the microcantilever. For electrostatic and magnetic force sensors, charged or magnetic particles are usually deposited on the microcantilever and the attractive or repulsive forces between the particles and the environment can bend the microcantilever. The forces can be calculated based on principles of electrostatics and magnetism.

2.2.3 Advantages and Disadvantages of the Microcantilever Biosensor

The nanomechanical microcantilever sensor has become a powerful and highly sensitive tool to study physisorption, chemisorption, and biosorption, as well as to investigate the properties of materials during heat transfer and phase transitions. For biological applications, since it is possible to work in liquid environments, it also provides great flexibility in tapping into complex biochemical reactions, such as DNA hybridization or molecular recognition.

Due to inevitable thermal drift and other undesirable interactions between the microcantilever and its environment, the results from a sensor system with a single microcantilever are not always reliable. To avoid the baseline drift and deflection induced by nonspecific adsorption of molecules on the microcantilever surface, multiple reference microcantilevers are sometimes introduced as a control. This microcantilever array can produce more consistent results and is likely the future of microcantilevers as sensors.

2.3 Quartz Crystal Microbalance

2.3.1 Introduction to the Quartz Crystal Microbalance

Among mechanical biosensors, the quartz crystal microbalance (QCM) has become one of the most established instruments. This device is based on quartz crystal resonators that are piezoelectric and thus enable the direct measurement of crystal deformation through electrical methods. With this device, the resonance frequency is measured and related to the mass change induced by an analyte binding to the recognition layer immobilized on the crystal surface.

2.3.2 Principles of QCM

The main component of a QCM is a thin quartz wafer sandwiched between two metal electrodes (Figure 2-6). The quartz wafer is produced from bulk quartz cut at specific orientations (Figure 2-7). These orientations are classified based on angles around the rectangular coordinate system OXYZ in a quartz crystal structure. Quartz crystals with different cut types will produce different piezoelectric responses. Two common cuts are X-cut and AT-cut crystals. The X-cut is cut normal to the x-axis. The AT-cut was introduced by Lack *et al.* and it is cut at 35° from the z-axis[97]. The "T" implies that the quartz is temperature-compensated and the "A" stands for the first of such cuts to be discovered. It has good performance over a wide temperature range.

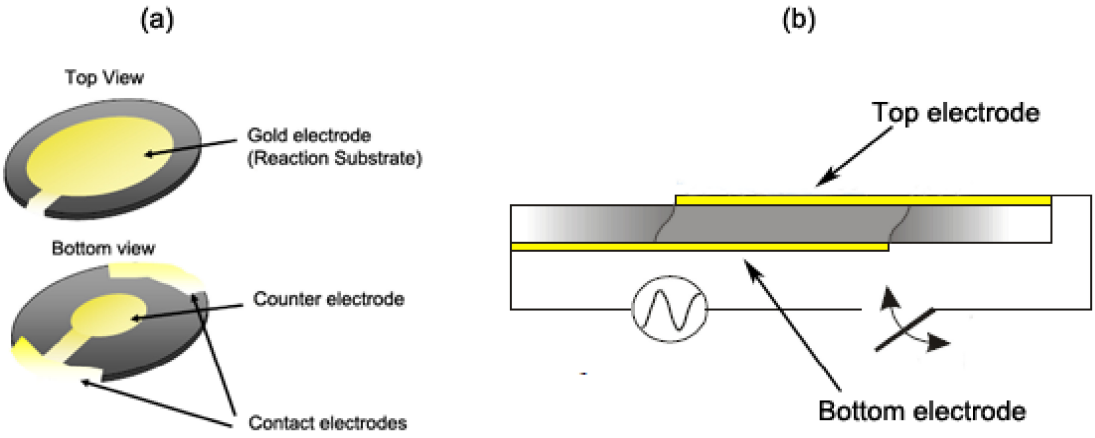

Figure 2-6. (a) Schematic diagram of a quartz crystal sensor, (b) cross-sectional view of the sensor. Adapted from QSense® (http://www.biolinscientific.com/q-sense/).

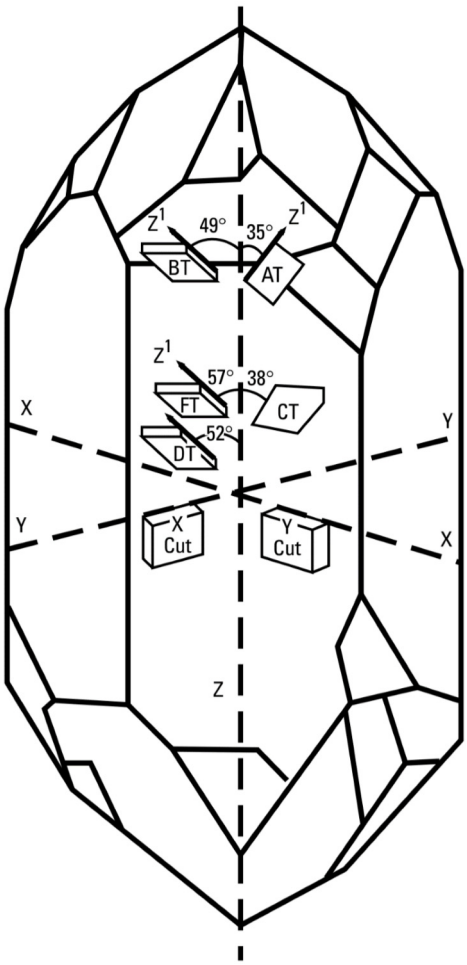

Figure 2-7. Quartz crystal orientation and common quartz crystal cuts.[98]
Adapted from Hewlett Packard®, 1997. AT-cut is the most popular cut of quartz crystal in use.[97]

Due to the piezoelectric nature of the quartz crystal, an alternating current (AC) applied to the electrodes results in the in-plane shear of the quartz crystal[99,100]. Resonance is generated when an AC voltage is applied with a frequency close to the resonance frequency (f_0) of the specific crystal. The resonance frequency of a QCM changes when the mass on one of its electrodes changes. In 1959, Sauerbrey provided experimental proof of the mass-frequency relationship[101]. Sauerbrey demonstrated that adding mass to the surface of the quartz crystal produces a frequency decrease proportional to the added mass. The linear relationship between changes in frequency, Δf, and adsorbed mass, Δm, is referred to as the Sauerbrey relationship[101]:

$$\Delta m = \frac{C}{n}\Delta f_n \qquad 2\text{-}4$$

where Δm is the mass deposited per unit area of crystal surface, Δf_n is the change in frequency at the vibrational mode number n, and C is the mass sensitivity constant of the instrument (17.7 ng/Hz·cm^2 for a 5 MHz quartz crystal)[100]. The Sauerbrey relationship is based on the assumption that the mass adsorbed on sensors is rigid. Many applications of QCM are problematic when frequency changes are due to the viscous and elastic properties of liquid samples.

As such, energy dissipation monitoring was introduced into the QCM system. Dissipation factor, D, is a parameter that quantifies energy damping in the system[100,102–108]. Dissipation occurs when the driving voltage to the crystal is shut off and the energy from the oscillating quartz crystal dissipates from the system (Figure 2-8). D is defined as[109]:

$$D = \frac{E_{lost}}{2\pi E_{stored}} \qquad 2\text{-}5$$

where E_{lost} is the energy lost during one oscillation cycle and E_{stored} is the total energy stored in the oscillator.

This new QCM-D system can spontaneously detect frequency and dissipation and provides insights into the structural (viscoelastic) properties of adsorbed layers.

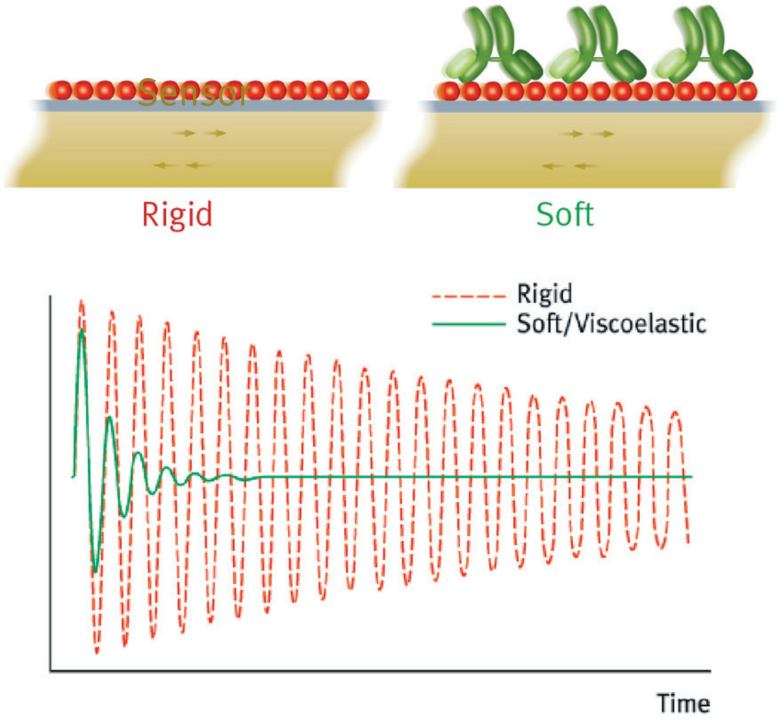

Figure 2-8. Schematic diagram of the difference in dissipation signal generated by a rigid (red) and soft (green) molecular layer on the sensor crystal.
Adapted from QSense® (http://www.biolinscientific.com/q-sense/).

Chapter 3: Use of a Nanomechanical Sensor to Probe the Interaction Between Cellulase and Cellulose

3.1 Introduction

Cellulose is the most abundant biopolymer on earth. It is renewable and biodegradable. Cellulose is insoluble and resistant to enzymatic hydrolysis, not only because the β-1,4-glycosidic bonds are strong covalent bonds, but also because the cellulose microfibrils are packed into tightly bound and crystalline lattices. Aggregation of cellulose prevents the direct access of each cellulose chain by biomolecules, including cellulase. Cellulases are produced by bacteria, fungi, plants, and some invertebrates, to convert insoluble cellulose to soluble sugars through general acid/base catalysis. It catalyzes the hydrolysis of β-1,4-glycosidic bonds of cellulose, breaking insoluble cellulose into fermentable simple sugars. There are three steps in the overall enzymatic hydrolysis process: initial binding, decrystallization, and hydrolytic cleavage. Although some previous research based on computational results suggests that the dissociation of cellulase from the substrate after hydrolysis is the bottleneck[110], most researchers believe that the decrystallization is the rate limiting step[48,111–114]. Even with the importance of the decrystallization, the mechanism for this step has not been fully clarified. The lack of substantial progress in understanding the mechanism underlying the decrystallization can be largely attributed to the dearth of experimental approaches capable of examining interfacial enzymatic activity on solid substrates.

The conventional method for studying the hydrolysis of cellulose involves monitoring the concentration of glucose and other simple sugars produced in this hydrolytic process[12]. This is not suitable for studying the decrystallization, as no new

compounds are generated in this process. Other techniques can be used to investigate the structural change of cellulose fibers, such as Fourier transform infrared spectroscopy (FTIR)[14,115–117], Raman spectroscopy[14,118,119], and X-ray photoelectron spectroscopy (XPS)[120–123]. However, these techniques focus on variations of cellulose at a global scale. The proposed mechanism (Figure 1-12) of decrystallization is likely to cause modification only on the surface of the cellulose substrate and within a relatively small region at nanometer scale. Thus, the techniques mentioned above are insufficiently sensitive for studying decrystallization.

Another common method for studying the interaction between a biological recognition layer (cellulose substrate) and adsorbate (cellulase enzyme) is the use of a biosensor. Existing biosensors can be classified into three categories: optical, electrical, and mechanical. Optical biosensors are highly sensitive but sometimes require laborious labeling processes. Electrical biosensors specialize in detecting biological processes that involve electron transfer.

Mechanical biosensors are based on the physical changes produced by the binding of targeted molecules. Among mechanical biosensors, the quartz crystal microbalance with dissipation monitoring (QCM-D) can be used to study the enzymatic hydrolysis of cellulose[104–108,120,124–134]. However, it is not suitable for studying the decrystallization, as the frequency signal measured by QCM-D is primarily induced by changes in the mass of the substrate coated on sensors, but enzymatic decrystallization by cellulase does not cause any change is the dry mass of cellulose, and there is no firmly established link between any mass change in hydrated cellulose and decrystallization[111,113]. The change in dissipation during enzymatic hydrolysis of cellulose could be caused by various

processes, such as the decrystallization, the adsorption of cellulase, morphological changes during cellulase enzymatic activities, hydration from coupled water, and film swelling[106,124]. This makes it difficult to obtain information about the decrystallization from the QCM-D measurement.

Another mechanical biosensor is the nanomechanical sensor—a mechanical sensor capable of nanometer-scale sensing. A typical nanomechanical sensor is the microcantilever. A microcantilever is typically 200 µm long, 1 µm thick, and 20 µm wide, and comes in various types of shapes (Figure 3-1), as do AFM probes. A microcantilever has been used to study interactions between different biomolecules[89,135–157]. Its applications include, but are not limited to, DNA and RNA recognition[89,145,147,148], the quantitative study of the mechanical response of receptors to antibiotics[142,144,154], the recognition of interactions between proteins and receptors[141,153], the detection of bacteria and pathogens[136,150,151], the study of conformational changess of proteins[135], and the development of a mass sensor for nanoparticles[149,155]. All these interactions can produce bending, which can then be detected by use of a laser beam to measure the deflection of the tip of the microcantilever. Thus, the detection takes place in real time (Figure 3-2)[89,137–140,143,148,158–161].

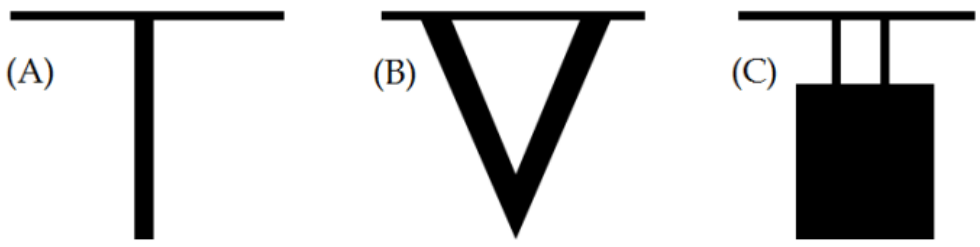

Figure 3-1. Various shapes of the microcantilever

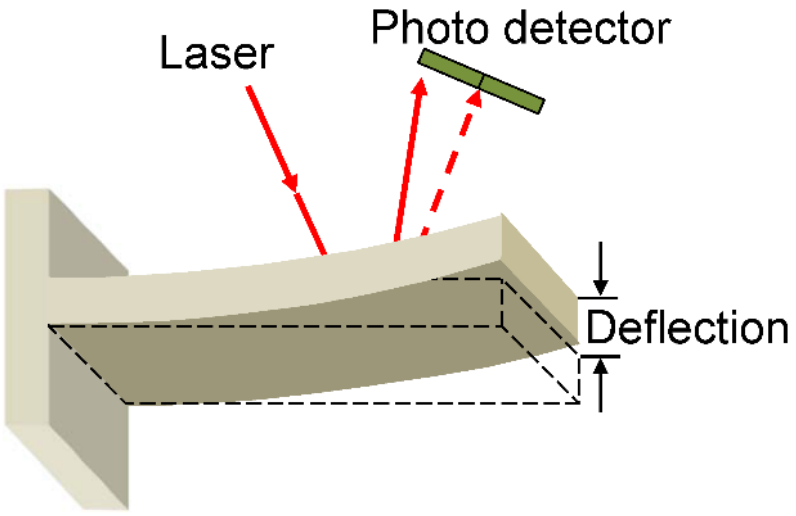

Figure 3-2. Working scheme of the microcantilever.

Other methodologies developed for the real-time study of cellulase include electrochemical sensors[162], flow ellipsometry[163], and isothermal titration calorimetry (ITC)[164–167]. High-Speed AFM[168] and photo-activated localization microscopy[169] can provide highly valuable information about cellulase activities on a substrate. However, like QCM-D, although they are capable of real-time studies, they cannot be used to examine the decrystallization because of the complexity of the data.

The properties of the substrate, including surface topography[170–173], heterogeneity[170], and crystallinity[174,175], can influence the ability of cellulase enzyme to carry out enzymatic hydrolysis[175]. On the other hand, mechanisms of synergistic effects of cellulases are complex and not fully understood[176], and the published results show inconsistent findings[177].

3.2 Previous Research on Decrystallization and Its Limitations

In the absence of experimental approaches for studying decrystallization, computational methods have been used. Beckham *et al.* calculated the free energies of decrystallization for four common cellulose polymorphs and placed them in decreasing order as follows: cellulose I_β, cellulose I_α, cellulose III_I, and cellulose II[111]. It is posited that the lower the free energy of decrystallization, the easier will be the overall hydrolysis. They also predicted that edge chains in native cellulose (cellulose I_α, cellulose I_β) are more difficult to decrystallize than those in synthetic cellulose allomorphs (cellulose II and cellulose III). To explain the enhanced overall hydrolysis of cellulose III compared with cellulose I, Gao *et al.* set up a mechanistic kinetic model, including enzyme binding, decrystallization, and glycosidic bond hydrolysis[113]. They concluded that individual cellulose chain decrystallization free energies are smaller for cellulose III than cellulose I.

3.3 Objective of the Current Study

This section develops a novel nanomechanical sensor and applies it to explore the interaction between cellulase and a cellulose solid substrate. With this technique, activities of both native cellulase and non-hydrolytic cellulase (chemically deactivated) on cellulose substrate film are examined. The experimental evidence for decrystallization is demonstrated by comparing the results from native cellulase and non-hydrolytic cellulase.

3.4 Materials and Methods

3.4.1 Preparation of Microcantilever Coated with Cellulose Model Film

200 mg microcrystalline cellulose (Sigma-Aldrich, Inc., St. Louis, MO) was added to 10 mL of 50-wt.% water/N-methylmorpholine N-oxide (NMMO, Alfa Aesar, Ward Hill, MA) and mixed on a hot plate at 110°C until the solution (~1 wt.%) was transparent. Then, 10 mL of dimethyl sulfoxide (DMSO, VWR, West Chester, PA) was added to dilute the solution. This cellulose solution was freshly prepared before every spin coating.

A microcantilever (SHOCON-TL-200, purchased from Applied NanoStructures, Inc.) was successively soaked in DI-water (Milli-Q, resistivity > 18 MΩ·cm) for 30 min, ethanol for 30 min, followed by UV-ozone (ProCleaner™) treatment for 30 min. Polyvinyl amine (PVAm, BASF) was used as an anchoring substance to improve the attachment of cellulose to the substrate. Microcantilevers were immersed into a 0.22-wt.% solution of PVAm for 20 min three times, rinsed with water between each immersion, and air dried before spin coating. Following this process, a thin layer of PVAm was coated on both the top and bottom sides of the microcantilever, working as anchoring layers to improve the adsorption of cellulose on the substrate. After pretreatment, model films were prepared by means of spin coating the cellulose solution evenly onto the top side of the microcantilever at 3000 rpm for 1 min. The microcantilever was then soaked in DI-water for 12 hours, air dried at room temperature, and dried in an oven at 80°C for 1 hour. As a result, the microcantilever was only coated on one side with cellulose (Figure 3-3). When cellulase acts on the cellulose coating and

changes the surface stress on one side, the surface stress difference Δσ between the two sides of the microcantilever produces measurable deflection of the microcantilever.

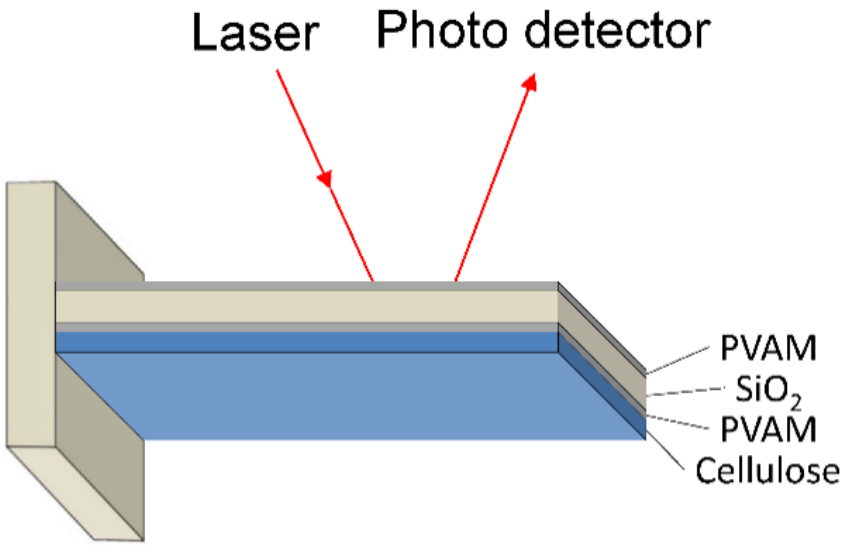

Figure 3-3. The coating scheme of surface coating on the microcantilever.

3.4.2 Enzyme Preparation and Characterization

The native cellulase (Celluclast® 1.5L, a product of Novozyme Corp., isolated from *Trichoderma reesei*) was purchased from Sigma-Aldrich. The partial enzyme, the carbohydrate binding module, (CBM, MW = 17 kD, isolated from *Clostridium cellulovorans*) was purchased from Sigma-Aldrich. Both were prepared as 0.10-mg/mL solution in 50-mM sodium acetate buffer (NaOAc, pH 5.5, VWR, West Chester, PA). In addition, some of the native cellulase was inactivated by treatment with $(NH_4)_2PdCl_6$ (Sigma-Aldrich, Inc., St. Louis, MO)[178–181]; this is termed non-hydrolytic cellulase (NH cellulase) hereafter. The irreversible inhibition of native cellulase was carried out by incubation of 0.30-mg/mL native cellulase with an equal volume of 200-μM $(NH_4)_2PdCl_6$

solution at 50°C for 1 hour. The inactivated solution of cellulase was then loaded onto Sephadex® G-25 gel (Sigma-Aldrich, Inc., St. Louis, MO) and was purified by centrifugation at 1000 rpm for 10 seconds. After this step, the $(NH_4)_2PdCl_6$ was removed from the cellulase solution and NH cellulase was obtained. Then both native cellulase and NH cellulase were mixed separately with 5.0-mM of p-nitrophenyl-β-D-cellobioside (pNPC, TCI America, Portland, OR) at 50°C for 40 minutes, and were quenched with 1.0-M Na_2CO_3. The amount of p-nitrophenol released after hydrolysis of pNPC by native cellulase and NH cellulase was calculated from the molar extinction coefficient of 18.5 ml/μmol/cm for p-nitrophenol at 410 nm (OD_{410}). Relative activity of NH cellulase was determined as the ratio of the amount of p-nitrophenol produced by NH cellulase to the amount of p-nitrophenol produced by native cellulase.

3.4.3 Cellulose Characterization

An AFM was used to characterize cellulose sample films. Before treatments with native cellulase and NH cellulase, surface roughness and topography of the cellulose films was examined with the AFM (Veeco NanoScope 3D multimode atomic force microscope).

There are several roughness calculation methods associated with the AFM technique. The current study employs roughness average (R_a) because it is a relatively straightforward parameter to obtain. The roughness average is described as follows (Figure 3-4)[182]:

$$R_a = \frac{1}{L}\int_0^l |Z(x)|dx \qquad 3\text{-}1$$

where Z(x) is a function that describes the surface profile analyzed regarding height (Z) and position (x) of the sample over the evaluation length (L).

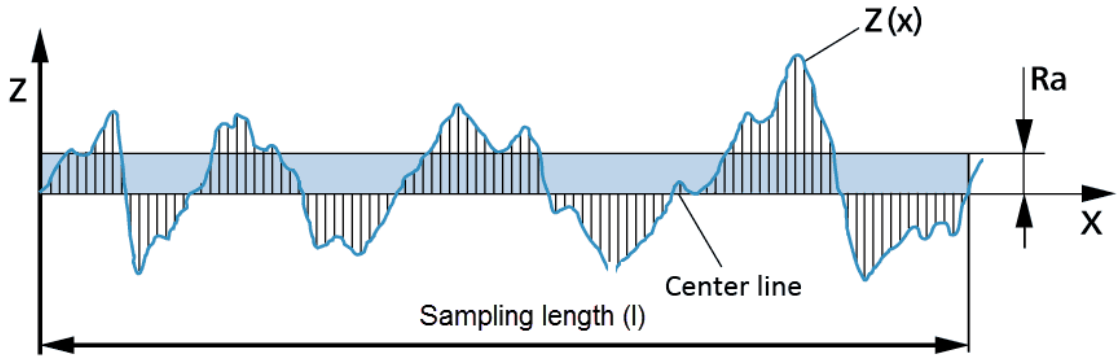

Figure 3-4. Profile of a surface (Z).
This figure represents the roughness average (R_a) based on the center line. Adapted from Jenoptik™. [182]

3.4.4 Detection of Enzyme–cellulose Interactions with a Microcantilever

All microcantilever measurements were performed with a modified commercial Nanoscope III scanning probe microscope (Digital Instruments/Veeco, Santa Barbara, CA). The cellulose-coated microcantilever was mounted with the coating face-down in a liquid cell having a volume of 50 µL. Here, CBM, native cellulase, or NH cellulase was introduced through injection either in a batch or continuous mode. For the batch mode, the solution was injected all at once. In the continuous mode, the injection was controlled by a syringe pump producing a steady flow rate ranging from 1 to 100 µL/min depending on the experiment. The cellulose was allowed to equilibrate with the assay buffer (25-mM sodium acetate, pH 5.5) for at least 2 hours before any addition. The solutions of cellulases and CBM were prepared with the same buffer 30 min before use. Each assay was performed against a reference to allow for subtraction of the background signal and control for the bulk solvent effect. A desktop PC, running programs written in LabView (National Instruments, Austin, TX) was used to record the microcantilever deflection signal from the AFM via a data acquisition board with a maximum data acquisition rate

of 300 kHz. The deflection measurement was monitored with a 5-mW laser diode at a wavelength of 680 nm and a split position sensitive detector. During measurements, data points were taken at a rate of 100 kHz. These data points were then averaged every 30 second. Calibration was carried out by measuring the ratio between the actual bending of the microcantilever (nm) and the change of voltage measured by position sensitive detector (volt) under controlled engagement. The conversion factor is 62 nm/volt.

3.4.5 Curve Fitting

We fit the progressive bending curves induced by the activities of native cellulase and NH cellulase with a combination of an exponential decay function and a linear function. The observed bending curves are apparently biphasic, suggesting that they represent only two steps of the overall enzymatic hydrolysis process. The initial phase is most likely the rapid reaction of the cellulose substrate with the enzyme cellulase to yield a stoichiometric amount of a pseudo-Michaelis complex. This initial phase can be described by an increase in microcantilever bending, the rate of which decreases with time; this can be described by the exponential decay function in Equation 3-2 below. The second phase is the steady state reaction of the pseudo-Michaelis complex that cleaves the cellulose. As a processive enzyme, the cellulase is able to cleave the polymeric chain of cellulose in its pseudo-Michaelis complex in a processive manner. This hydrolytic cleavage results in a steady decrease in microcantilever bending, which can be described by the linear function in Equation 3-2, representing zero order kinetics:[183–186]

$$\Delta Z = A_1 e^{-k_1 t} - k_2 t + C \qquad 3\text{-}2$$

where ΔZ is the magnitute of the microcantilever bending, k_1 is the fitting parameter for the exponential decay phase of the curve corresponding to the initial rise of the bending,

k_2 is the fitting parameter of the linear phase of the curve corresponding to the decline of the bending, A_1 is the amplitude of the exponential decay, and C is a fitting constant. Fitting results are shown in discussion.

3.5 Influence of Coating Methods on Cellulose Coatings

The preparation of a cellulose-coated nanomechanical microcantilever sensor is of utmost importance for the success of this project. This requires the coating of a microcantilever to meet at least two criteria. First, the microcantilever should be coated on one side only. The other side should experience minimal binding to the adsorbate. Otherwise, surface stress on one side would cancel that on the other side. Second, the coating on the coated side should uniformly cover most of the microcantilever. The formation of surface stress requires that the coating fully cover the microcantilever surface. Both of these criteria are easy to achieve for a macro-sized surface by means of spin coating. The small size of a microcantilever makes coating particularly challenging. Also, the preparation of the cellulose solution involves NMMO as a primary solvent, which has a high viscosity and is difficult to disperse on a microcantilever surface. The combination of these two factors makes the task of cellulose coating demanding. For this reason, several different coating methods were attempted to optimize the coating of the microcantilever.

3.5.1 Spin Coating

Spin coating is one of the most common coating techniques for producing uniform polymer thin films[187–191]. A typical sample preparation for spin coating follows the following steps. First, a piece of double-sided tape is affixed to the center of a petri dish. Second, several layers of Teflon tape are stacked next to the double-sided tape on

the petri dish. Third, the microcantilever is then placed on the double-sided tape with the microcantilever base stuck to the tape while keeping the microcantilever tip above the Teflon tape. The number of layers of Teflon tape is carefully determined so the bottom side of the microcantilever is blocked by Teflon tape and the microcantilever remains flat. Then, the entire petri dish is subjected to spin coating such that the top side of the microcantilever is coated with cellulose. See Figure 3-5 and Figure 3-6 for a schematic diagram.

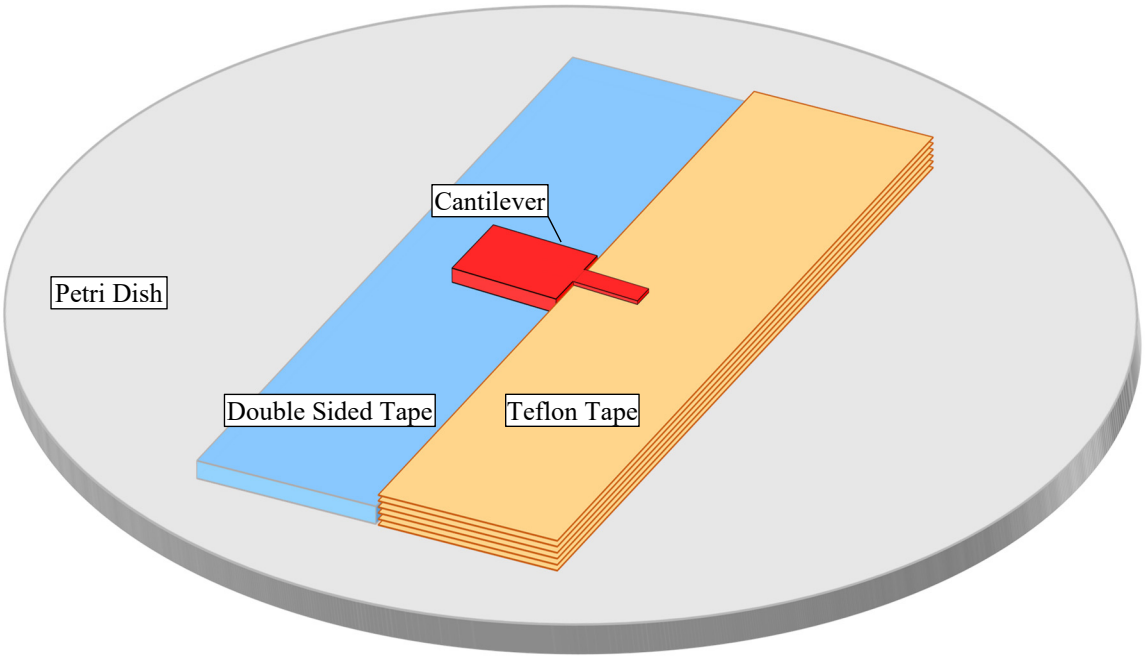

Figure 3-5. Schematic diagram of the blocking technique for spin coating.

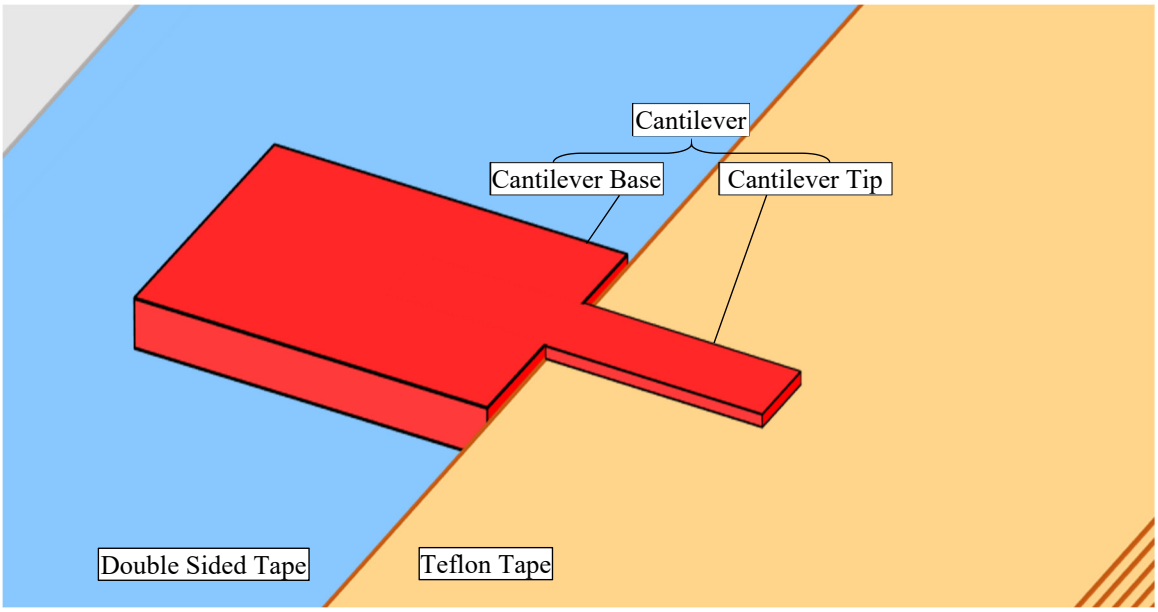

Figure 3-6. Close-up of a schematic diagram of the bottom blocking technique for spin coating.

The spin coating can also be carried out with the microcantilever flipped (Figure 3-7). The top side of the microcantilever has to be blocked with Teflon tape, and the bottom becomes coated with cellulose.

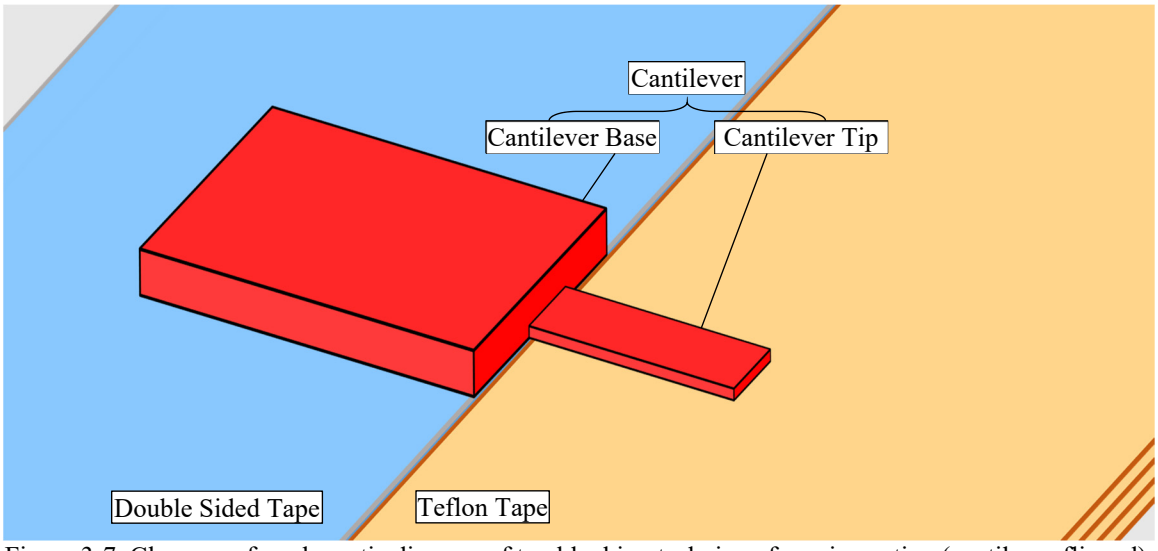

Figure 3-7. Close-up of a schematic diagram of top blocking technique for spin coating (cantilever flipped).

Spin coating for the microcantilever has a major disadvantage. Namely, it does not have the ability to manipulate the solution at a micro scale and the solution tends to bypass the microcantilever during spinning due to the surface tension of the solution. Thus, the success rate of this coating method is likely to be low.

3.5.2 Float Coating

The current study developed a novel coating method, named *float coating.* Figure 3-8 provides a schematic description. This method entails carefully dropping a microcantilever into a freshly prepared hot cellulose solution and slowly removing it after several minutes (e.g., 5 minutes). Because of the low weight of the microcantilever and the strong surface tension of the cellulose solution, the microcantilever can float on the latter. If both steps have been carried out with caution, then only one side of the microcantilever was in contact with the cellulose solution and a single-side coated cantilever was obtained. The advantage of this coating method is that the cellulose solution can completely cover the tip of the microcantilever. However, because there is only a slight contact between the microcantilever and hot cellulose solution, the amount of solution left on the microcantilever is tiny. Thus, the solid cellulose coating is thin and the microcantilever may not be fully covered after the cellulose solution has crystallized. Like spin coating, float coating can also be completed with the microcantilever flipped.

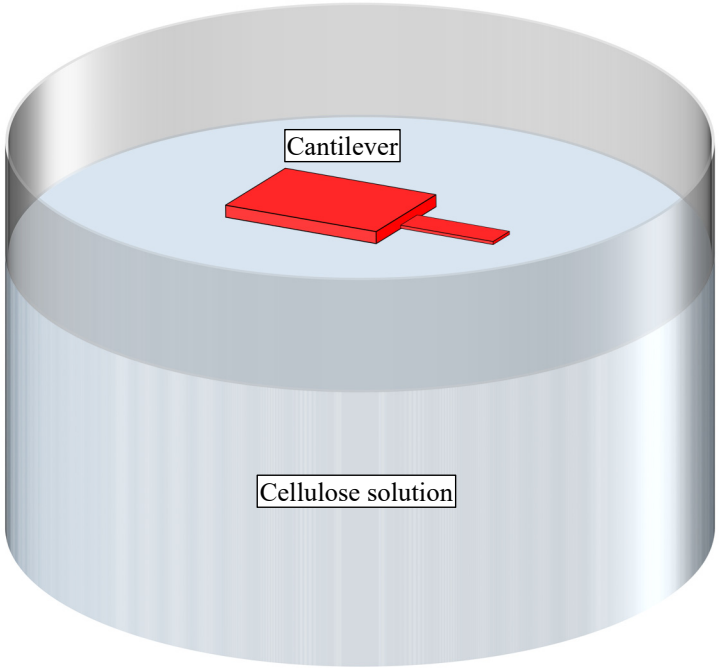

Figure 3-8. Schematic diagram of the float coating technique (cantilever shown flipped).

3.5.3 Brush Coating

The coating methods just discussed cannot be used to successfully manipulate the cellulose solution at a microscale level. As a result, the cellulose solution is coated onto a microcantilever with low chance. To address this problem, the current study developed an additional coating method — *brush coating*—which utilizes a small, iron wire as a brush to apply cellulose solution to a microcantilever under the microscope of AFM (Figure 3-9). The microcantilever is first affixed onto the AFM sample stage with double-sided tape. Next, a small iron wire is mounted to the AFM tip holder which is then inserted into the AFM head. A small drop of freshly prepared cellulose solution is then transferred to the tip of the iron wire. Considering that the AFM can manipulate the iron wire at a nanoscale, the cellulose solution can be spread onto the microcantilever with the iron

wire. This step is repeated three times. The AFM sample stage is heated to 50°C to maintain the fluidity of cellulose solution. As a result, the coating side of the microcantilever can be fully covered while the other side is kept clean.

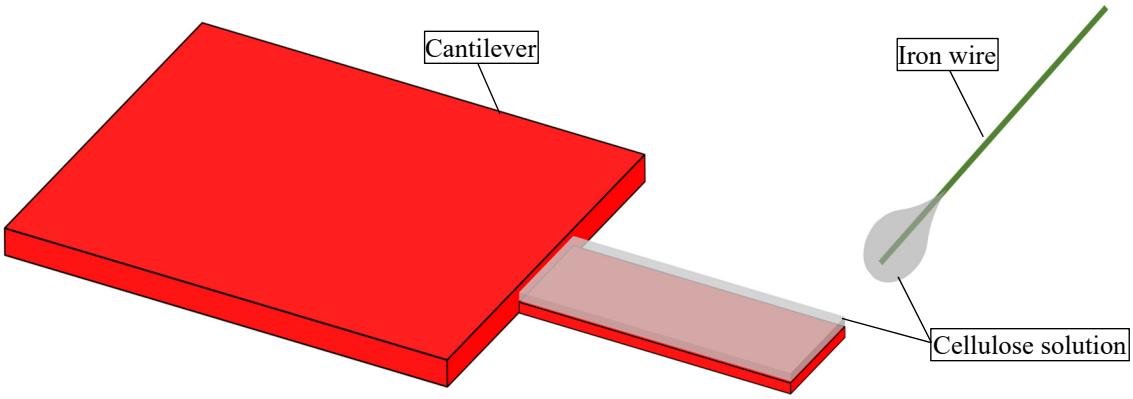

Figure 3-9. Schematic diagram of brush coating technique (cantilever shown flipped).

After the cellulose solution is brushed onto the microcantilever, it is placed into DI-water for the cellulose to crystallize into a film on the microcantilever. This brush coating method usually resulted in the complete coverage of cellulose on the microcantilever. Compared with spin coating, the cellulose solution does not undergo spreading, and the uniformity of the film obtained from brush coating technique was still of concern.

To ensure a uniform, flattened model film, the brush coating method was optimized by adding a spinning step before the microcantilever with cellulose coating was placed into DI-water. The microcantilever was taped to the petri dish and spun on a

spin coater while. The spinning helped to level out the cellulose solution on the microcantilever, it did also sacrifice the thickness of the coating.

3.6 Results

3.6.1 AFM Images of Microcantilevers

Representative AFM images of microcantilevers are shown in Figure 3-10, including: 1) no coating (clean microcantilever); 2) PVAm coating; 3) blocked side of microcantilever after cellulose coating; and 4) coated side of microcantilever after cellulose coating. After the cleaning process, the microcantilever was freed of contamination (Figure 3-10A) and ready for PVAm coating. The PVAm was then dip-coated onto the surface of the microcantilever (Figure 3-10B). With the PVAm coating as an anchor layer, the cellulose solution was then coated onto the microcantilever. The blocked side was free of cellulose (Figure 3-10C) and the coated side was covered by a uniform layer of cellulose. Ideally, the coated side of the microcantilever must be completely and uniformly covered with cellulose.

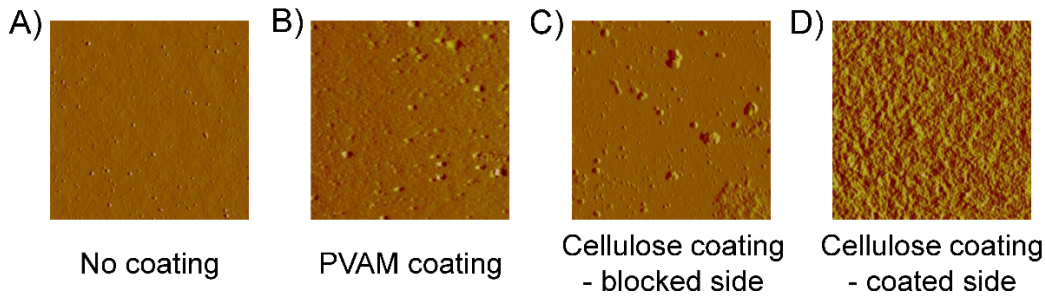

Figure 3-10. Images of the microcantilever from the AFM.
(A) no coating (clean microcantilever), (B) PVAm coating, (C) blocked side of microcantilever after cellulose coating, (D) coated side of microcantilever after cellulose coating.

3.6.2 Characterization of Non-hydrolytic Cellulase

Palladium compounds irreversibly inhibit CBH I and EG II from *Trichoderma reesei*, EG from *A. niger* (EglA), and β-glucosidases[178,179,192]. Different concentrations of $(NH_4)_2PdCl_6$ were employed to inactivate native cellulase. Although the native cellulase used is a mixture of CBH (~70%, 40 – 60% CBH I), EG (~25%), and β-glucosidases (~2%)[193], all components have similar specific activities as tested with p-nitrophenyl-β-D-cellobioside (pNPC) used in the current study's assay[194]. The percentage activities of NH cellulase are shown in Table 3-1 and Figure 3-11. It was determined that 200-μM $(NH_4)_2PdCl_6$ could decrease the relative activity to less than 3% after incubation with native cellulase for 40 minutes. Since the relative error for these measurements is about 1%, activities are considered virtually halted with 200-μM $(NH_4)_2PdCl_6$ after 40 minutes. Thus, inactivation in the current study was carried out under these conditions. A possible explanation for the observed inhibition of cellulase activity may be the disruption of disulfide bonds, which serve to stabilize the active site tunnel of cellulase.[179]

Table 3-1. % Activities of non-hydrolytic cellulase

Time (min)	30 mM $(NH_4)_2PdCl_6$	100 mM $(NH_4)_2PdCl_6$	200 mM $(NH_4)_2PdCl_6$
0	74.50 ± 6.74	40.60 ± 5.72	30.99 ± 4.97
10	40.62 ± 5.25	6.36 ± 1.77	3.82 ± 2.03
20	38.96 ± 1.61	5.70 ± 1.87	2.74 ± 1.76
40	28.27 ± 3.05	4.04 ± 1.13	2.62 ± 1.10
60	26.44 ± 0.76	2.96 ± 0.54	0.93 ± 0.59

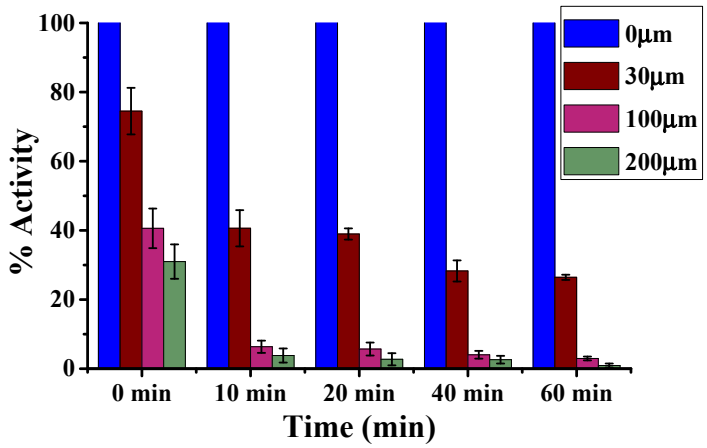

Figure 3-11. % Activity of cellulase after treated with $(NH_4)_2PdCl_6$ with different concentrations at different durations.

3.6.3 Use of a Cellulose-coated Microcantilever for CBM Binding Assay

The microcantilever coated with cellulose was first treated with cellulase binding module (CBM), a partial enzyme isolated from the cellulase enzyme. The bending of the microcantilever was monitored and is shown in Figure 3-12. This modular domain, which anchors cellulase to cellulose, does not generate hydrolysis activity on cellulose, but still maintains the ability to bind to cellulose. Figure 3-12 clearly shows that exposing the cellulose substrate on the microcantilever to the CBM does not generate any measurable deflection over 120 minutes.

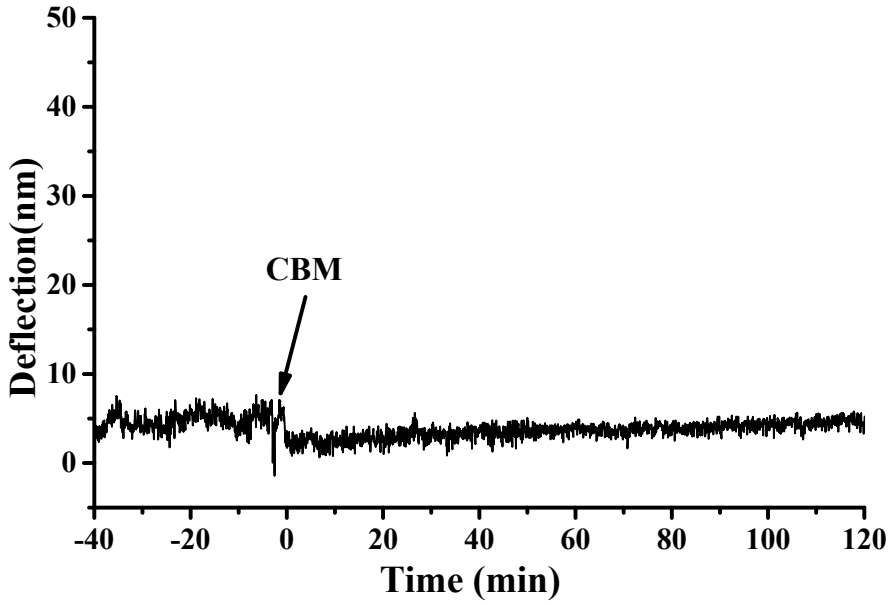

Figure 3-12. The deflection curve of CBM actions on cellulose measured by the microcantilever sensor.

3.6.4 Use of a Cellulose-coated Microcantilever for Enzyme Activity Assays

Then, a cellulose-coated microcantilever was treated with native cellulase. The results are shown in Figure 3-13. Immediately after the injection of native cellulase (0.010 mg/mL), the microcantilever deflection increased, reached a peak, and then decreased within a period of 10 hours. This suggests that native cellulase is capable of inducing bending of the cellulose-coated microcantilever. The observed curve typically indicates two counteractive activities, discussed in greater detail later.

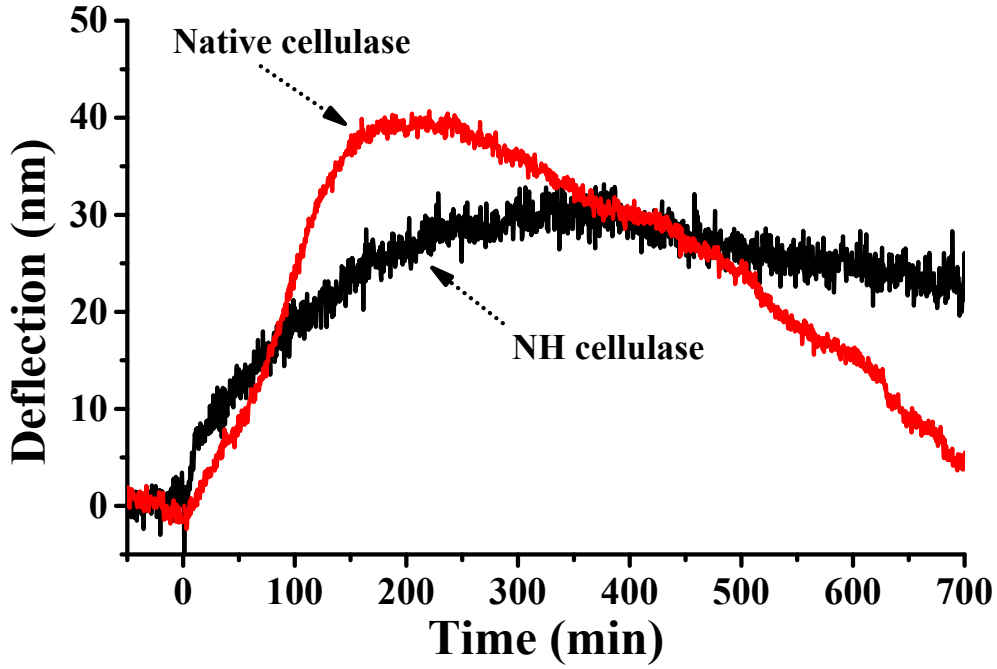

Figure 3-13. The deflection curves measured by the microcantilever sensor, probing native cellulase and NH cellulase induced structural change of cellulose.

The same microcantilever assay was performed with NH cellulase instead of native cellulase (NH cellulase has lost its ability to cause hydrolysis of cellulose). The result is also shown in Figure 3-13. The deflection of the microcantilever increased immediately after injection of the NH cellulase, similiarly to the behavior of cantilever in the native cellulase environment. However, unlike that for native cellulase, the deflection after the peak has been reached decreases neither rapidly nor extensively; on the contrary, the deflection decreases very slowly. These differences are discussed in detail in the discussion.

3.7 Discussion

As shown in Figure 3-12, binding of CBM (binding module of cellulase) on cellulose surface does not result in any bending of the cantilever. Although CBM is smaller compared with cellulase, of the three steps of the overall hydrolysis process effected on solid cellulose by native cellulase, the initial binding step does not likely result in any bending of the cantilever (Figure 3-12). The bending observed can be assumed to be due to the two other activities: decrystallization and hydrolysis (Figure 1-12). In the microcantilever bending curve in the presence of native cellulase, the deflection of the microcantilever increases at the beginning and decreases after approximately 200 minutes, suggesting the occurrence of two processes of cellulase activity, producing two counteracting effects on the microcantilever: upward bending followed by a return to the unbent state at the molecular level (Figure 3-13). These two processes are assumed to be decrystallization and hydrolysis. On the other hand, the NH cellulase was able to generate upward bending at the beginning in similar manner to native cellulase. This increase upward deflection, as for native cellulase, shows the preservation by NH cellulase of the enzymatic activity responsible for the bending during the early phase (Figure 3-13).

For quantification of aspects of the bending curves, a curve fitting procedure was conducted on each experimental curve shown in Figure 3-14. This fitting procedure used both linear and exponential terms in order to accommodate the whole range of each experimental curve over the 700 minutes of data collected. The resultant fitting parameters as per Equation 3-2 are shown in Table 3-2. For native cellulase, the intial rise covered 0 to 200 minutes, and the decline phase covered 200 to 700 minutes. For NH

cellulase, the intial rise covered 0 to 300 minutes, and the decline phase covered 300 to 700 minutes.

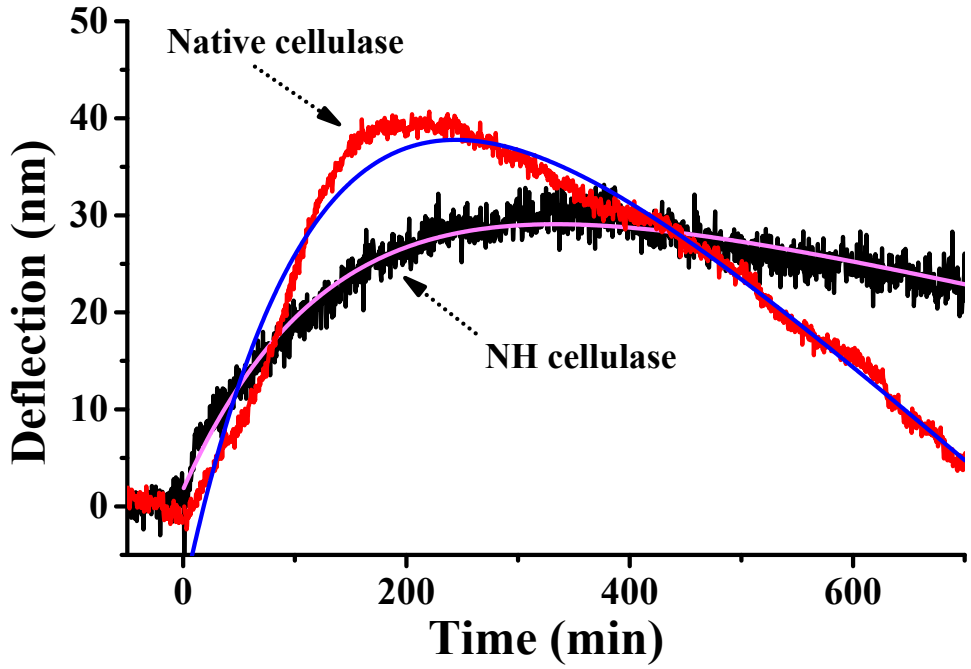

Figure 3-14. Curves fitted based on microcantilever bending data for native cellulase and NH cellulose.

Table 3-2. Fitting parameters of native cellulase and NH cellulase

	Initial rise phase ($k_1 \times 10^{-3}$ min^{-1}) (± SE)	Decline phase ($k_2 \times 10^{-1}$ min^{-1}) (± SE)	R-Squared
Native cellulase	7.7 (± 0.11)	1.0 (± 0.01)	0.97
NH cellulase	7.1 (± 0.11)	0.26 (± 0.01)	0.94

In this fitting process, the quantity R^2 in the last column of Table 3-2 is used as an indicator of the goodness of fit of the computed line to the experimental data. The high

values of R^2 indicate that, in both native cellulase and NH cellulase, the computed lines fit the data well.

Figure 3-13 and Figure 3-14 show that the deflections of micocantilever for both native cellulase and NH cellulase increased immediately in a similar pattern at the beginning. After that, for the NH cellulase, in which the hydrolytic cleavage activity has been abolished, the declining phase of the induced bending of microcantilever was substantially suppressed. By contrast, the decline of microcantilever bending in the case of native cellulase is not suppressed. This result suggests that the decline of the microcantilever bending and its return to a nearly unbent condition is most likely caused by hydrolytic cleavage of the cellulose coating.

The initial rise of the bending curve may result from cellulase actions before hydrolytic cleavage, such as initial binding and/or enzymatic decrystallization. However, since the initial binding did not produce immediate and measurable microcantilever bending (Figure 3-12), the initial rise of the bending curve would seem to be caused solely by the decrystallization step. This is the first experimental evidence of decrystallization as one of the steps of the overall process of hydrolysis of cellulose.

Figure 3-15 is the diagram of the response of the top-coated microcantilever exposed to cellulase. The explanation for the observed bending is posited as follows. Cellulose, as it is deposited on the microcantilever in crystalline form, is in the extended chain conformation, the chain axis being parallel to the long axis of the microcantilever. When, during decrystallization, the extended chains in the top layer of the cellulose film and released by cellulase from their positions in the crystal. They immediately assume a random coil conformation. The end-to-end distance of a random coil is much less than

the end-to-end distance of an extended chain. Thus, the freed cellulose chains behave as entropic springs and shorten. These shortened chains, in turn, shorten the top layer of cellulose, creating a tension parallel to the long axis of the microcantilever that causes the microcantilever to bend upward. Only when the continuity of these randomly coiled cellulose chains is broken by hydrolysis of cellulose by native cellulase, the tension is relieved, allowing the microcantilever to unbend and return closer to its original flat geometry. In the case of NH cellulase, little or no hydrolysis occurs. And the upwardly bent microcantilever cannot unbend to a significant extent.

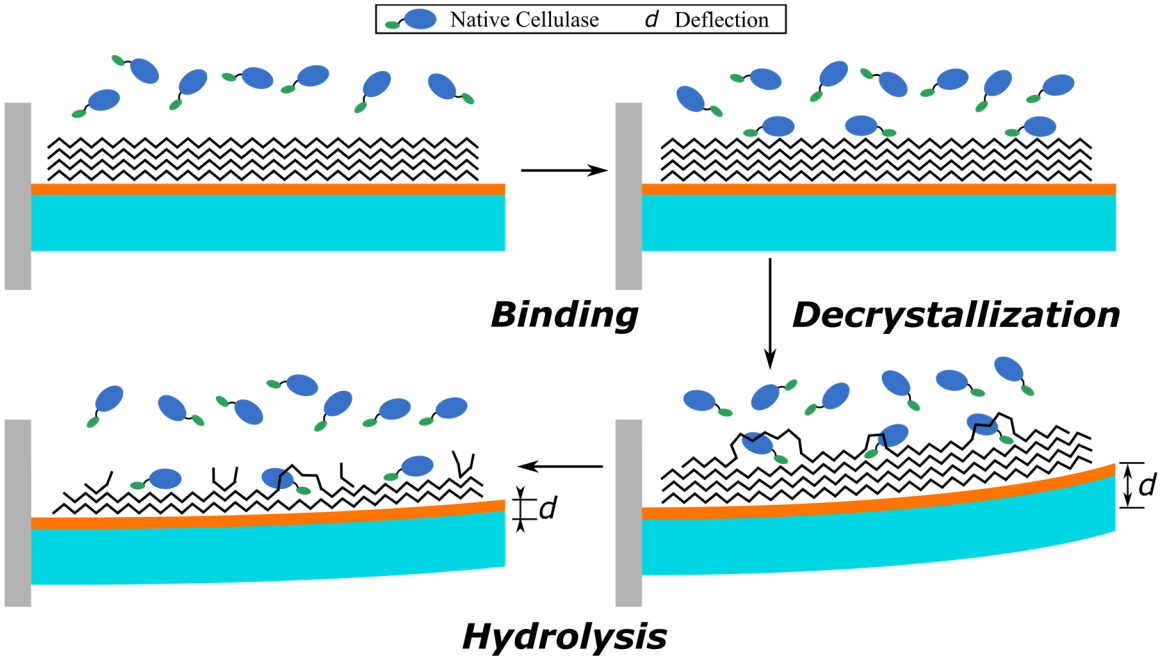

Figure 3-15. Schematic diagram depicting how cellulose–cellulase interactions may cause a microcantilever to bend upon decrystallization and then unbent upon hydrolysis of the top layer of cellulose.

By comparing deflection curves from native cellulase with those obtained from NH cellulase (Figure 3-13), it can be seen that the maximum deflection induced by the decrystallization from NH cellulase is slightly smaller (30 nm vs 38 nm) than that induced by cellulase. It can be concluded that the majority of deflection is caused by the decrystallization or related processes. This deflection provides strong experimental evidence confirming that decrystallization is an important step and has a large impact on the overall enzymatic hydrolysis of cellulose.

3.8 Conclusion

The study details the successful coating of a microcantilever with a cellulose model film and the investigation of the enzymatic activities of cellulase with this novel nanomechanical sensor. The bending curves of the microcantilever provide physical evidence for the decrystallization. This is consistent with the notion that the decrystallization may play a crucial role in overall enzymatic hydrolysis by cellulase. Future experiments will investigate the effects of temperature, degree of crystallinity, and other factors on the decrystallization and hydrolysis of cellulose by cellulase. These studies may provide novel perspectives into the mechanisms of stress development in enzymatic hydrolysis, which has broad implications for the studies of biochemical interfaces. To better verify the effect of initial binding of cellulase on the cantilever bending, a cellulase mutant, which could bind on cellulose surface without doing decrystallization and hydrolytic cleavage actions, is needed as a control in future experiments. Additionally, this technical approach could serve as a useful screening tool for the optimization of cellulase enzymes which are of great importance for the modern green chemical industry.

Chapter 4: Cellulase Activity on Cellulose: Topographical Evidence

4.1 Introduction

As discussed earlier, cellulose is the most abundant biopolymer, and biofuel products from lignocellulosic sources have great potential in serving as substitute energy sources. Before it becomes a conventional form of energy, as is petroleum fuel, a number of challenges have to be overcome. One of them is the low efficiency of enzymatic hydrolysis of cellulose. Cellulose is an insoluble, semi-crystalline polymer, held together by inter- and intra- molecular hydrogen bonding, that is resistant to degradation[43,48–52]. Cellulase is the enzyme responsible for the overall hydrolysis of cellulose. This hydrolysis occurs in three sequential steps: binding, decrystallization, and hydrolytic cleavage. Cellulase with higher enzymatic efficiency is urgently needed, if the cost of biofuel production is to be lowered. The decrystallization step is believed by many researchers to be the rate-limiting step.[48,111–114]. However, currently the mechanism of the decrystallization is not fully understood, and there is no experimental approach to examine it directly or indirectly.

Many studies have indicated that the topography of cellulose undergoes noticeable changes as a result of treatment with many different types of cellulase[106,124,127,170,181,195–204]. In one of these studies, Nidetzky and colleagues[205] monitored the surface modification of a model film of cellulose by cellulase. They suggested that the change of roughness during enzymatic hydrolysis was a step-wise rather than continuous process[195].

In another study, Liu *et al.* found that the surface roughness of cellulose increased upon the addition of CBH I, one type of cellulase[198]. They confirmed that the change in

roughness was due to the activity of CBH I. In another study, Jiang *et al.* examined the change in roughness of cellulose before and after hydrolysis and observed an increase in the roughness after hydrolysis[127]. They suggested that this increase was due to two processes, the partial erosion of the cellulose substrate during hydrolysis and adsorption of cellulase on the substrate. In another study, Wang *et al.* monitored the height profile of cellulose before and after hydrolysis, and also observed an increase in the surface roughness of the cellulose[199]. Maurer *et al.* also found that the surface roughness of cellulose increased from 24.3 ± 3.1 nm to 47.2 ± 2.2 nm after enzymatic hydrolysis by cellulase[163]. In examining the surface morphology of cellulose model films, Jaušovec *et al.* utilized AFM topographical imaging and reported an increase in roughness of the substrate as a result of treatment with cellulase[197].

While by far the majority of studies have shown an increase in roughness upon the cellulase treatment, some groups have also reported inconsistent findings that suggested a decrease in surface roughness[106,206]. Using Celluclean®, a brand new cellulase enzyme developed by Novozymes, Calvimontes *et al.* observed an increase in roughness of cellulose film at low cellulase concentrations and a decrease at high cellulase concentrations[207]. The rarity of cases where roughness of cellulose has been found to decrease could be attributed to the properties of the cellulose substrate (crystallinity, polymorph, and distribution of amorphous and crystalline areas) and the details (concentration and composition) of the cellulases used.

In view of the prior findings, it is likely that changes in the surface roughness of cellulose, as a result of treatment with cellulase, are closely related to cellulase action on cellulose. Thus, assessing changes of surface roughness of cellulose may be a feasible

method to investigate the action of cellulase on cellulose.

4.2 Objective of the Current Study

This section of the dissertation reports a study of cellulase in which the time-dependent change in surface roughness of a cellulose substrate was monitored. The study aims to compare the surface topography of cellulose after exposure to native cellulase and native CBH I (another form of native cellulase) with the surface topography of cellulose after exposure to the non-hydrolytic forms of these cellulases (chemically inactivated, as described below). It is hoped that this comparasion will establish experimental evidence for the decrystallization activity of cellulase.

4.3 Materials and Methods

4.3.1 Preparation of Cellulose Model Films for Roughness and QCM-D Studies

Microcrystalline cellulose (Sigma-Aldrich, Inc., St. Louis, MO) was added to 10 mL of 50-wt.% water/N-methylmorpholine N-oxide (NMMO, Alfa Aesar, Ward Hill, MA) and was stirred on a hot plate at 110°C until the solution was transparent. Then, this solution was diluted by the addition of 10 mL dimethyl sulfoxide (DMSO, VWR, West Chester, PA). A solution of cellulose in the above mixed solvent was freshly prepared before each spin coating. For binding experiments monitored by means of QCM-D, a 0.50% (w/w) solution of cellulose in the mixed solvent was used for coating the sensor disc. For roughness experiments monitored by means of AFM, two concentrations of cellulose in the mixed solvent were used: the low concentration of cellulose (LCC) was 1.0% (w/w), while the high concentration of cellulose (HCC) was 3.0% (w/w).

Round cover glasses (12-mm micro-cover glasses, VWR, West Chester, PA) and QCM-D sensors (Q-sense, Gothenburg, Sweden) were soaked in DI-water (Milli-Q,

resistivity > 18 MΩ·cm) for 30 min and then in ethanol for 30 min, followed by a UV-ozone (ProCleaner™) treatment for 30 min. To improve the attachment of cellulose to the surface, the round cover glasses and QCM-D sensors were immersed in 0.22% (wt.%) polyvinyl amine (PVAm) solution for 20 min and were rinsed with DI-water. The PVAm coating was repeated three times, and the round cover glasses and QCM-D sensors were air-dried before they were spin coated. This thin layer of PVAm worked as an anchoring layer, improving the attachment of cellulose to the surface.

After pretreatment with PVAm, cellulose model films were prepared by spin coating the cellulose solution onto the round cover glasses and QCM-D sensors. For the round cover glasses, LCC and HCC cellulose solutions were used; the spin speed was initially 1000 rpm for 10 seconds and then 3000 rpm for 1 min. For QCM-D sensors, 0.50%-wt.% cellulose solution was used and the spin speed was 3000 rpm for 1 min. The round cover glasses and QCM-D sensors were then soaked in DI-water for 12 hours, were air-dried at room temperature, and were oven-dried at 80°C for 1 hour.

The solid cellulose derived from solution is termed regenerated cellulose. The crystalline portion of the regenerated cellulose is termed cellulose II.

4.3.2 Preparation and Characterization of Cellulase

In the current study, 50-mM sodium acetate buffer (NaOAc, pH 5.5, VWR, West Chester, PA) was used to prepare a 0.10-mg/mL solution of native cellulase (*Trichoderma reesei*, Sigma-Aldrich, Inc., St. Louis, MO), a 0.10-mg/mL solution of native CBH I (Sigma-Aldrich, Inc., St. Louis, MO), another form of native cellulase, and a 0.10-mg/mL solution of bovine serum albumin (BSA, Sigma-Aldrich, Inc., St. Louis, MO). In a separate procedure, some of the native cellulase and native CBH I were

inactivated with $(NH_4)_2PdCl_6$ (Sigma-Aldrich, Inc., St. Louis, MO) to form non-hydrolytic cellulase (NH cellulase) and non-hydrolytic CBH I (NH CBH I). The irreversible inhibition of both of these native cellulases was accomplished by incubation of a 0.30-mg/mL solution of each native cellulase with an equal volume of 200-μM $(NH_4)_2PdCl_6$ solution at 50°C for 1 hour[180,181,206,208]. The inactivated solutions of cellulases were then loaded separately onto Sephadex® G-25 gel (Sigma-Aldrich, Inc., St. Louis, MO) and were purified by centrifugation at 1000 rpm for 10 seconds. After this step, the $(NH_4)_2PdCl_6$ was removed from the solutions of cellulases, and NH cellulase and NH CBH I were obtained. The final concentration of all solutions of cellulases were 0.10-mg/mL. After inactivation, the solutions of cellulases were mixed with 5.0-mM p-nitrophenyl-β-D-cellobioside (pNPC, TCI America, Portland, OR) at 50°C for 40 minutes and then were quenched with 1.0-M Na_2CO_3. The amount of p-nitrophenol released after hydrolysis of pNPC by native cellulase, NH cellulase, native CBH I, and NH CBH I was calculated from the molar extinction coefficient of 18.5 ml/μmol/cm for p-nitrophenol at 410 nm (OD_{410}). Relative activity of NH cellulases was determined as the ratio of the amount of p-nitrophenol produced by NH cellulases to the amount of p-nitrophenol produced by native cellulases. In another procedure, BSA was also treated in the same manner with $(NH_4)_2PdCl_6$ and was termed Pd-treated BSA. Both BSA and Pd-treated BSA were used as blanks.

4.3.3 Cellulose Characterization

An AFM (Veeco NanoScope 3D multimode atomic force microscope) was used to measure the mean roughness (R_a) of surface. X-ray diffraction (XRD) was used to measure the crystallinity index (CI) of cellulose samples. The diffractometer (Rigaku

SmartLab, Tokyo, Japan) used 1.54-Å $Cu_{K\alpha}$ radiation, generated at 40 kV and 44 mA. Scans were taken from $5° \leq 2\theta \leq 50°$ in increments of 0.02°, at a rate of 1°/min.

4.3.4 Roughness Measurements

Round cover glasses coated with cellulose films were used for roughness measurements. Each round cover glass was split into 8–10 small triangular slices. One glass slice was immersed in the buffer as a blank and the others were placed in 0.1-mg/mL solution of cellulases. At time points of 10, 20, 30, 50, 100, 200, and 400 minutes, one glass slice was taken out from the solution of cellulases, rinsed in DI-water at 0°C, air dried, and used for AFM imaging (Figure 4-1).

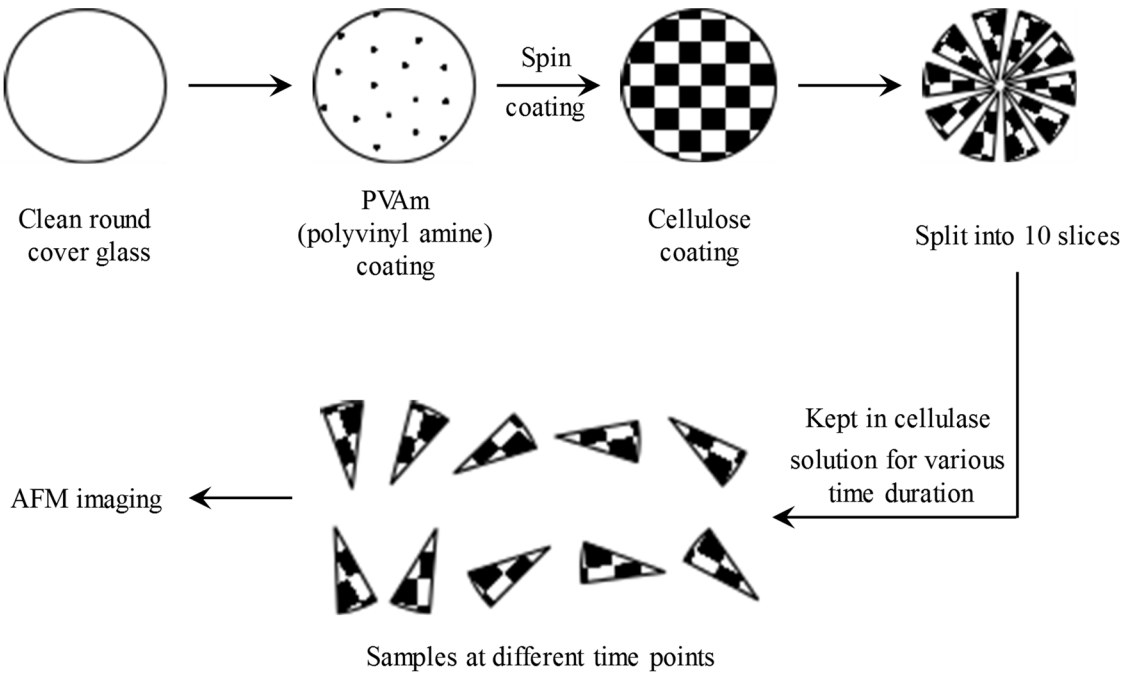

Figure 4-1. Sample preparation for the roughness measurements.

Usually, AFM imaging is not ideal for time-dependence measurement because the sample surface may alter during the time-consuming imaging process and samples from the same series of measurement may already differ in the first place. To alleviate this concern, the roughness measurements were carefully designed. At each time point when a sample was taken, it was immediately placed into an ice water (0°C). This action, followed by blow-drying the sample with N_2, quenched all enzymatic activity right after the sample was taken. To ensure the comparability of samples taken at different time points, samples were all selected from the same round cover glass (Figure 4-1). In addition, the AFM images were obtained only from the sharp angle of every triangle slice, as this part of the slice was the closest to the center of the original round cover glass. In this way, the possible variation of cellulose coatings between samples taken at different time points could be minimized. Furthermore, all roughness measurements at each time point were repeated at least three times to ensure reproducibility.

4.3.5 Enzyme-cellulose Binding Examined with QCM-D

A QCM-D (Q-Sense E4) was used for studying cellulase activity on the cellulose model films at 37°C. A highly sensitive sensor device, QCM-D is capable of simultaneously measuring changes in frequency and energy dissipation. The frequency change can be related to the change in mass of the adsorbed layer, and the dissipation factor change can be related to the change in viscoelasticity properties of the layer adsorbed to the surface of quartz crystal. QCM-D has been used previously to study the interactions between cellulose and cellulase[106,107,124–127,130,131,134].

The experiments in the current study were conducted in a static mode, where NaOAc buffer and solutions of cellulases were directly and manually added to the open

module of QCM-D. Before each experiment, the cellulose film on each sensor was allowed to swell in the buffer for about 2 hours until equilibrium was reached. The buffer was then carefully removed with a pipette that was not allowed to touch the sensor, and a 0.10-mg/mL solution of cellulases was added to the open module. Changes in the resonance frequency (Δf_n) and energy dissipation factor (ΔD) of vibrational mode number, n=3, were recorded as a function of time for approximately 4 hours.

4.4 Results

4.4.1 Preparation and Characterization of Cellulose Model Films

The AFM images of the model films on the round cover glasses and QCM-D sensors are shown in Figure 4-2. The thickness of cellulose coatings is about 50–100 nm on cover glass and 20–30 nm on QCM-D sensors. The mean roughness of the LCC sample is about 10 nm, and the mean roughness of the HCC sample is about 20 nm.

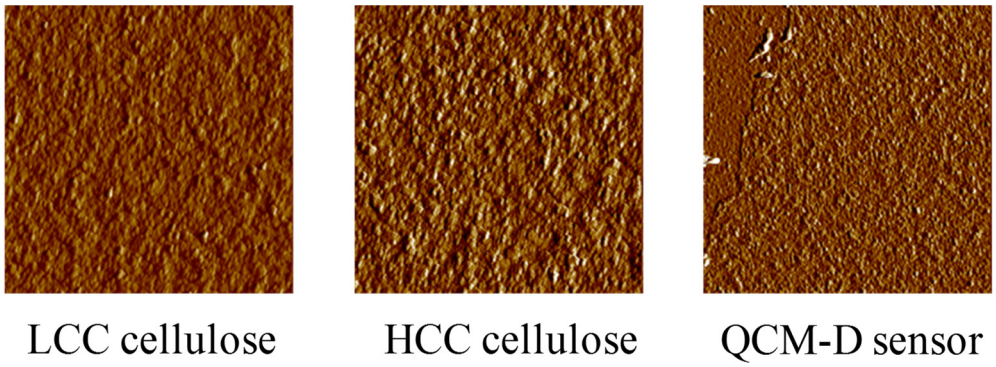

Figure 4-2. The AFM images for all three substrates, low concentration cellulose (LCC), high concentration cellulose (HCC), and cellulose coating on the QCM-D sensor.

The crystallinity of the cellulose sample has a significant effect on the activity of cellulase[175,209]. When the cellulose coating was prepared, the concentration of original

cellulose solution may have influenced the level of crystallinity of the cellulose. To measure the crystallinity of the cellulose substrate, X-ray diffraction (XRD) tests were performed. Results from the XRD tests are shown in Figure 4-3.

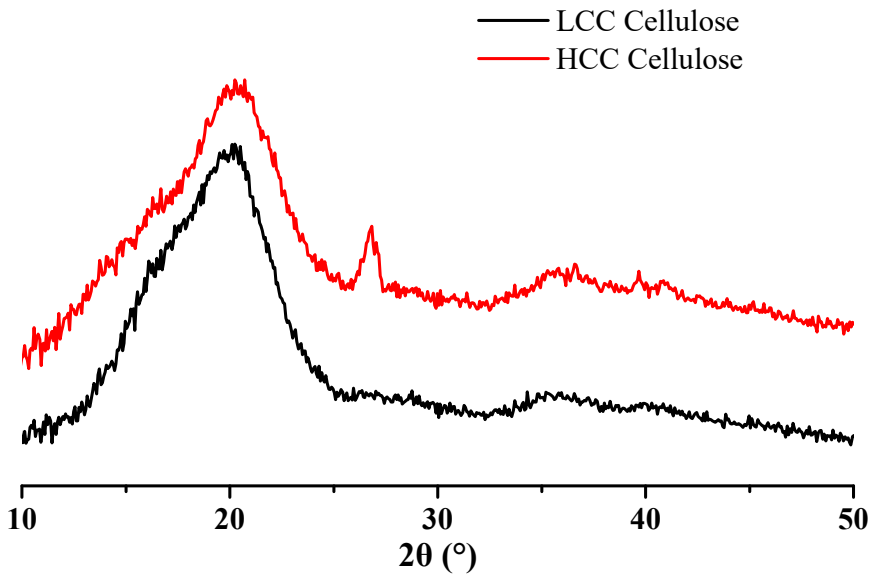

Figure 4-3. X-ray diffractions results from LCC and HCC cellulose.

The absence of sharp peaks in the XRD scans shows that both cellulose samples have limited crystallinity and are highly amorphous. However, the HCC cellulose sample showed a small peak at 27°, evidence for some crystallinity. There are many methods for CI% calculation[209]. Following the common practice in the field, the current study uses the following equation:

$$CI\% = \frac{I_{cr} - I_{am}}{I_{cr}} \times 100\% \qquad 4\text{-}1$$

where I_{cr} is the diffraction intensity at $2\theta° \approx 21.7°$ for cellulose II, and I_{am} is the intensity at $2\theta° \approx 16°$ for the amorphous background[210].

In general, the crystallinities for both HCC and LCC samples are low. By comparing the two samples, CI% of the HCC cellulose sample is almost twice that of LCC cellulose sample (Table 4-1).

Table 4-1. Crystallinity of LCC and HCC cellulose samples.

wt.%	Peak Intensity		CI%
	I_{cr} (21.7°)	I_{am} (16°)	
1.0% (LCC)	0.013389	0.011178	16.5
3.0% (HCC)	0.013775	0.009906	28.1

4.4.2 Characterization of Non-hydrolytic Cellulase and Non-hydrolytic CBH I

To prepare non-hydrolytic cellulases, in the current study, different concentrations of $(NH_4)_2PdCl_6$ were employed to inhibit the activity of native cellulase and native CBH I. To characterize the activity of these NH cellulase and NH CBH I, p-nitrophenyl-β-D-cellobioside (pNPC), a model for cellulose, was used as a substrate.[194]

The percentage activities of both types of cellulase after inactivation are shown in Table 4-2 and Figure 4-4. Similar to the results described in 3.6.2, the current study also found that 200-μM $(NH_4)_2PdCl_6$ reduced the activities of cellulase and CBH I to less than 3% of the native activities. Since the relative error for the measurement is about 2%, activity can be considered essentially quenched after 40 minutes of incubation with 200-μM $(NH_4)_2PdCl_6$. Since the removal of the activity was the goal, this procedure was used to inactivate all cellulases in the current study.

Table 4-2. % activities of 0.1 mg/mL non-hydrolytic cellulases.

Time (min)	Cellulase		CBH I	
	100 mM $(NH_4)_2PdCl_6$	200 mM $(NH_4)_2PdCl_6$	100 mM $(NH_4)_2PdCl_6$	200 mM $(NH_4)_2PdCl_6$
0	40.23 ± 5.71	30.75 ± 4.92	66.26 ± 3.74	57.22 ± 1.75
20	5.71 ± 1.82	2.71 ± 1.79	22.77 ± 4.86	6.60 ± 2.33
40	4.05 ± 1.15	2.60 ± 1.08	11.47 ± 2.57	2.32 ± 2.74

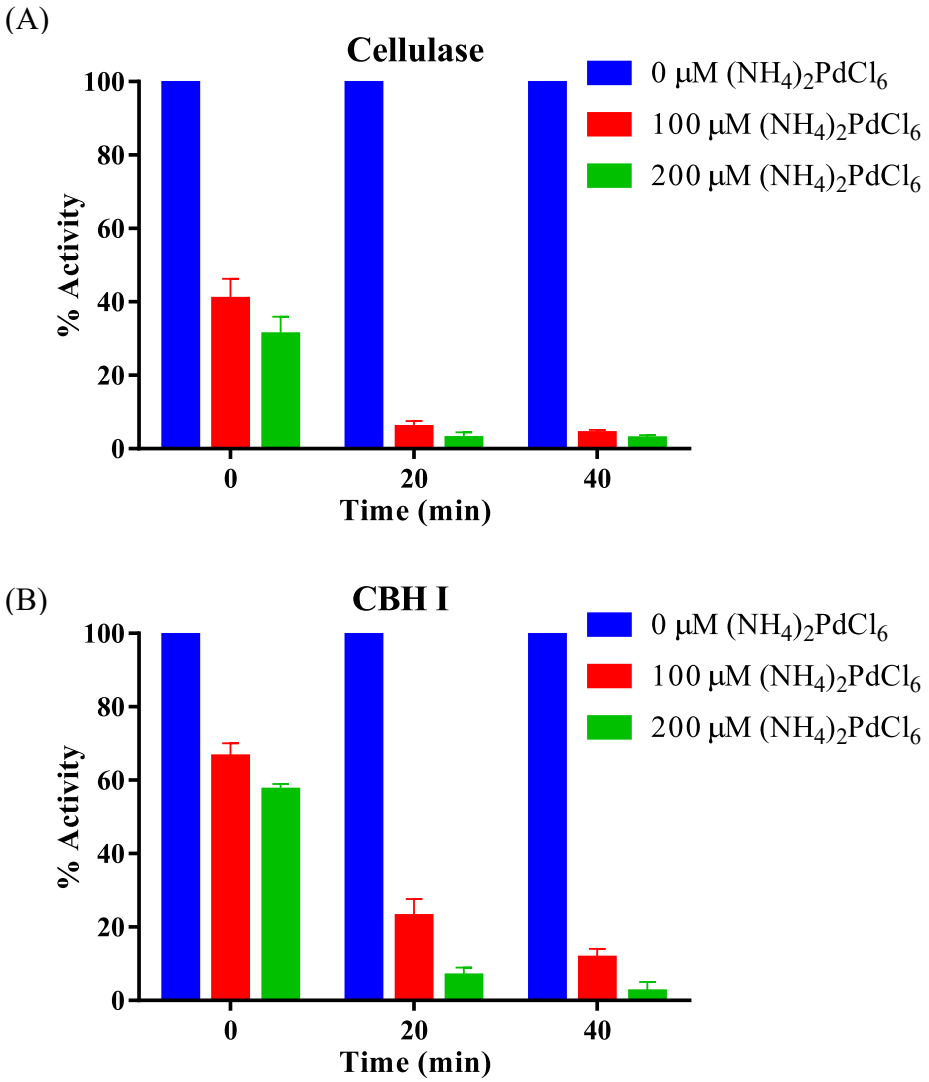

Figure 4-4. Percentage activity of 0.1 mg/mL cellulase and 0.1 mg/mL CBH I after being treated with $(NH_4)_2PdCl_6$ for different concentrations and with different time durations.

4.4.3 Results of Roughness Measurements

Percentage change of roughness R_a, ΔR%, can be calculated from:

$$\Delta R\% = \frac{R_{at} - R_{a0}}{R_{a0}} \times 100\% \qquad 4\text{-}2$$

where R_{a0} is the initial mean roughness (R_a) of the cellulose and R_{at} is the R_a of the cellulose at time *t*. Thus, a positive ΔR% indicates a rougher surface and a negative ΔR% indicates a smoother surface than at $t = 0$. All roughness measurements were repeated at least three times to ensure the reproducibility.

4.4.3.1 *Roughness Measurements of cellulose treated with Cellulases and CBH I*

Figure 4-5A and Figure 4-5B show the results for change in roughness (ΔR%) after treatment of LCC and HCC cellulose samples with 0.10-mg/mL solutions of native cellulase, NH cellulase, native CBH I, and NH CBH I at 25°C. Similar treatments affect LCC and HCC similarly, although different types of treatment differ from each other in their effects.

Figure 4-5C and Figure 4-5D show the results for change in roughness (ΔR%) after treatment of LCC and HCC cellulose samples with 0.10-mg/mL solutions of native cellulase, NH cellulase, native CBH I, and NH CBH I at 37°C. As found for lower temperature, similar treatments affect LCC and HCC similarly, although different types of treatment differ from each other in their effects.

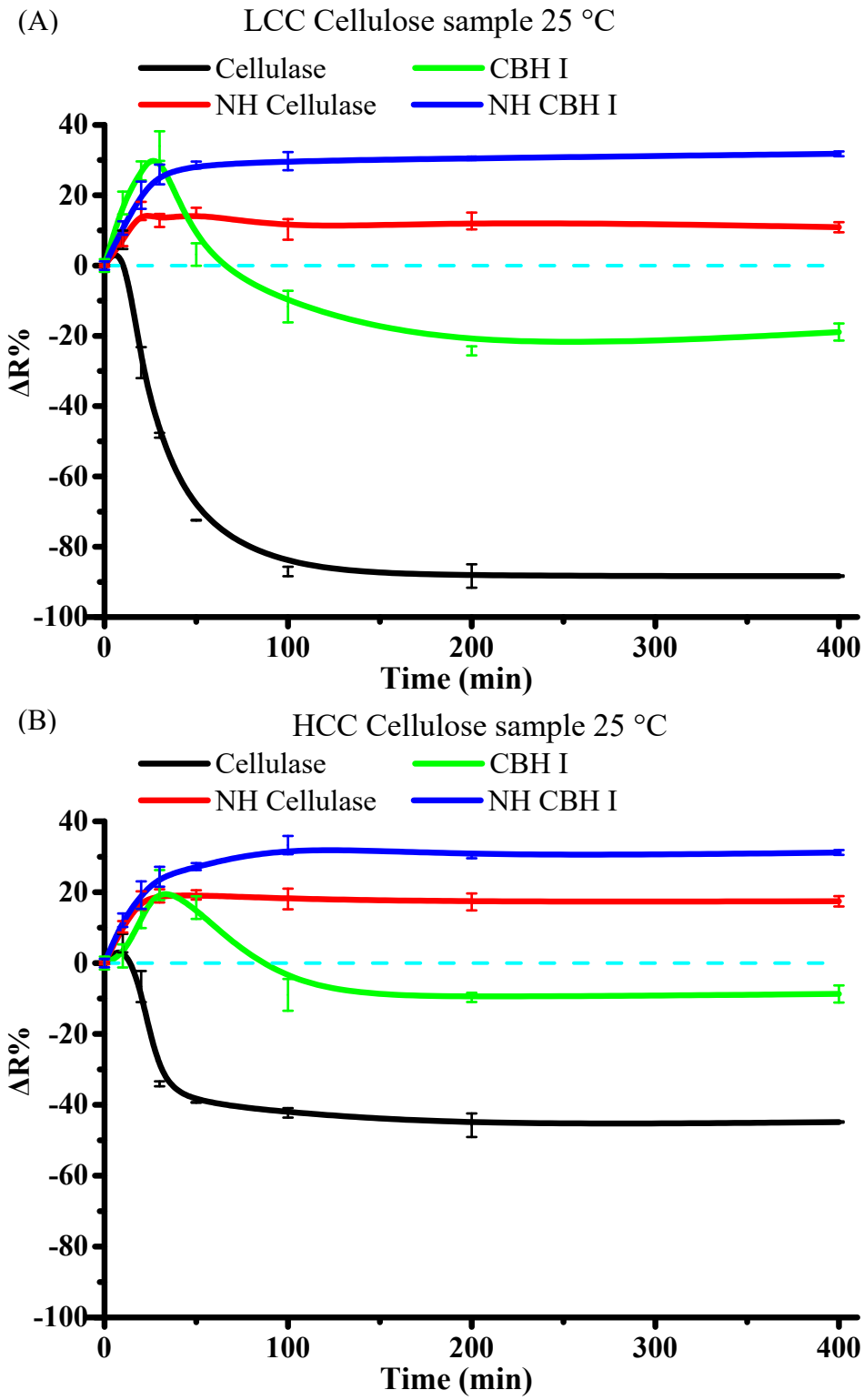

Figure 4-5. Roughness measurements results from 0.10-mg/mL native cellulase and non-hydrolytic (NH) cellulase, native CBH I and non-hydrolytic (NH) CBH I.
(A) LCC cellulose at 25°C. (B) HCC cellulose at 25°C. (C) LCC cellulose at 37°C. (D) HCC cellulose at 37°C.

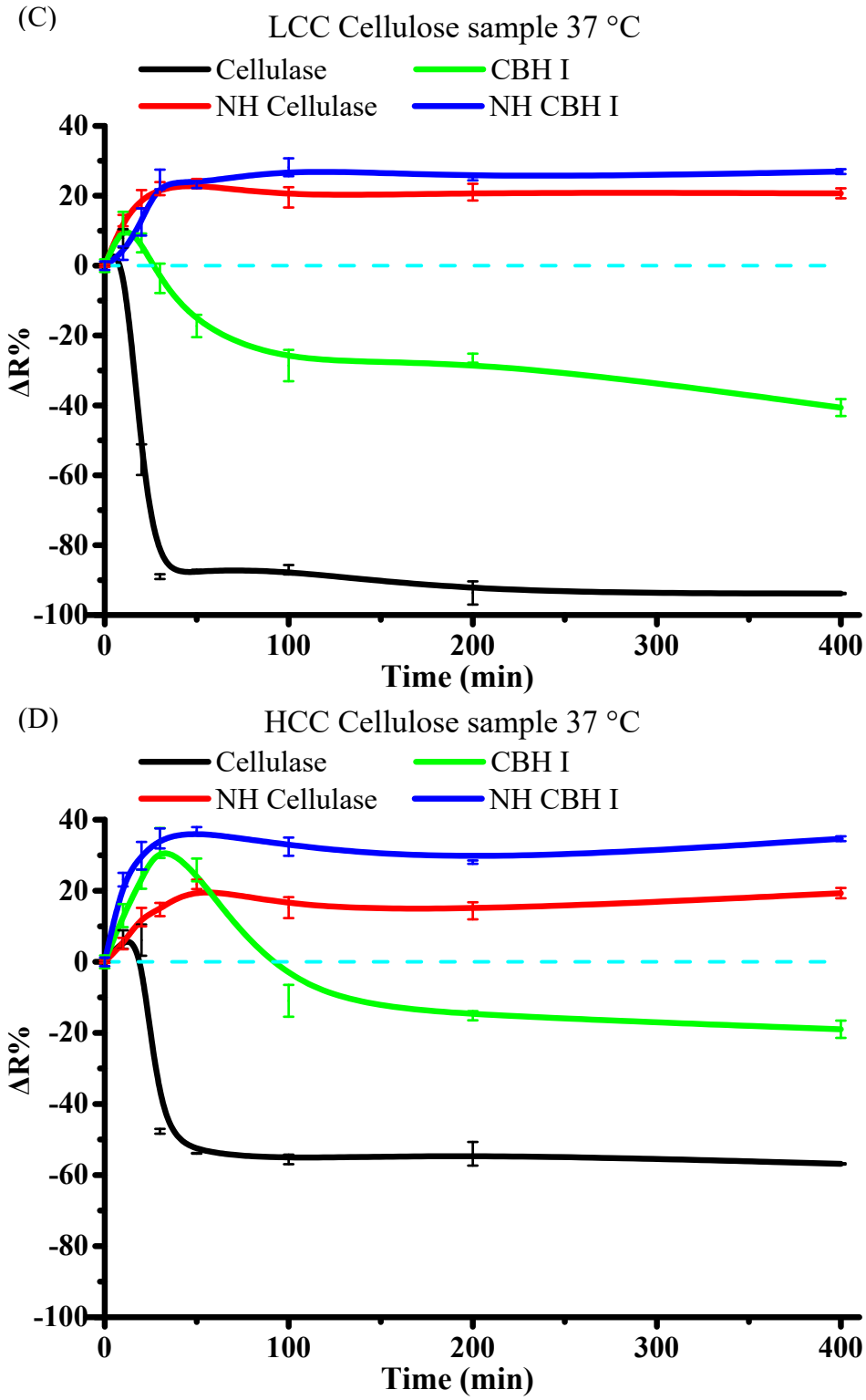

Figure 4-5 (continued). Roughness measurements results from 0.10-mg/mL native cellulase and NH cellulase, native CBH I and NH CBH I.
(a) LCC cellulose at 25°C. (b) HCC cellulose at 25°C. (d) LCC cellulose at 37°C. (d) HCC cellulose at 37°C.

4.4.3.2 *Roughness Measurements of BSA*

Cellulase adsorbs on the cellulose substrate through initial binding. The changes in surface topography of the substrate may be a result of cellulase adsorption. Any change in surface roughness due to the initial adsorption would complicate the interpretation of the changes in roughness being caused by cellulase activities. Thus, we decided to conduct a blank experiment with bovine serum albumin (BSA) as an adsorbate to evaluate the impact of physical adsorption on the surface roughness of cellulose. Both the size and molecular weight of BSA, a protein, are close to those of CBH I (66.5 kDa vs. 65.0 kDa, 15.0 nm vs. 18.0 nm)[46,211]. Bovine serum albumin is known to bind to cellulose[38,40,212–221], and it does not hydrolytic cleave the cellulose substrate. Therefore, it is a suitable blank for this study. Not only was BSA used as a blank but also BSA treated with $(NH_4)_2PdCl_6$ (Pd-treated BSA) in the manner described in section 4.3.2 was used as a blank. Roughness measurement results of HCC and LCC cellulose samples treated with 0.10-mg/mL BSA or Pd-treated BSA at 25°C and 37°C are shown in Figure 4-6. These ΔR% are all close to zero (~-5%–+5%), and negligible compared with the ΔR% for cellulase or CBH I (Figure 4-5).

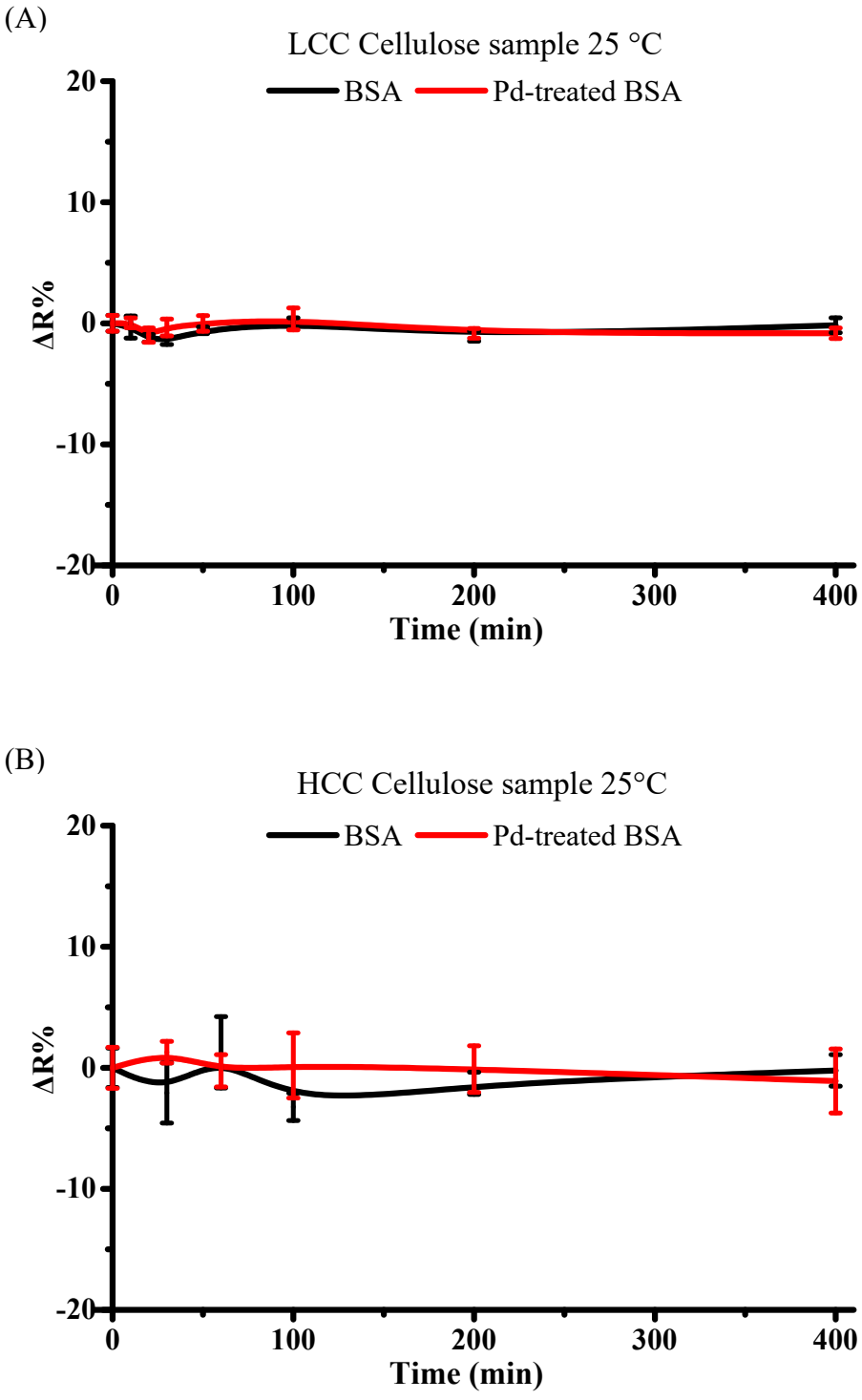

Figure 4-6. Roughness measurements results of 0.10-mg/mL BSA and Pd-treated BSA. (A) LCC cellulose sample at 25°C. (B) HCC cellulose sample at 25°C. (C) LCC cellulose sample at 37°C. (D) HCC cellulose sample at 37°C.

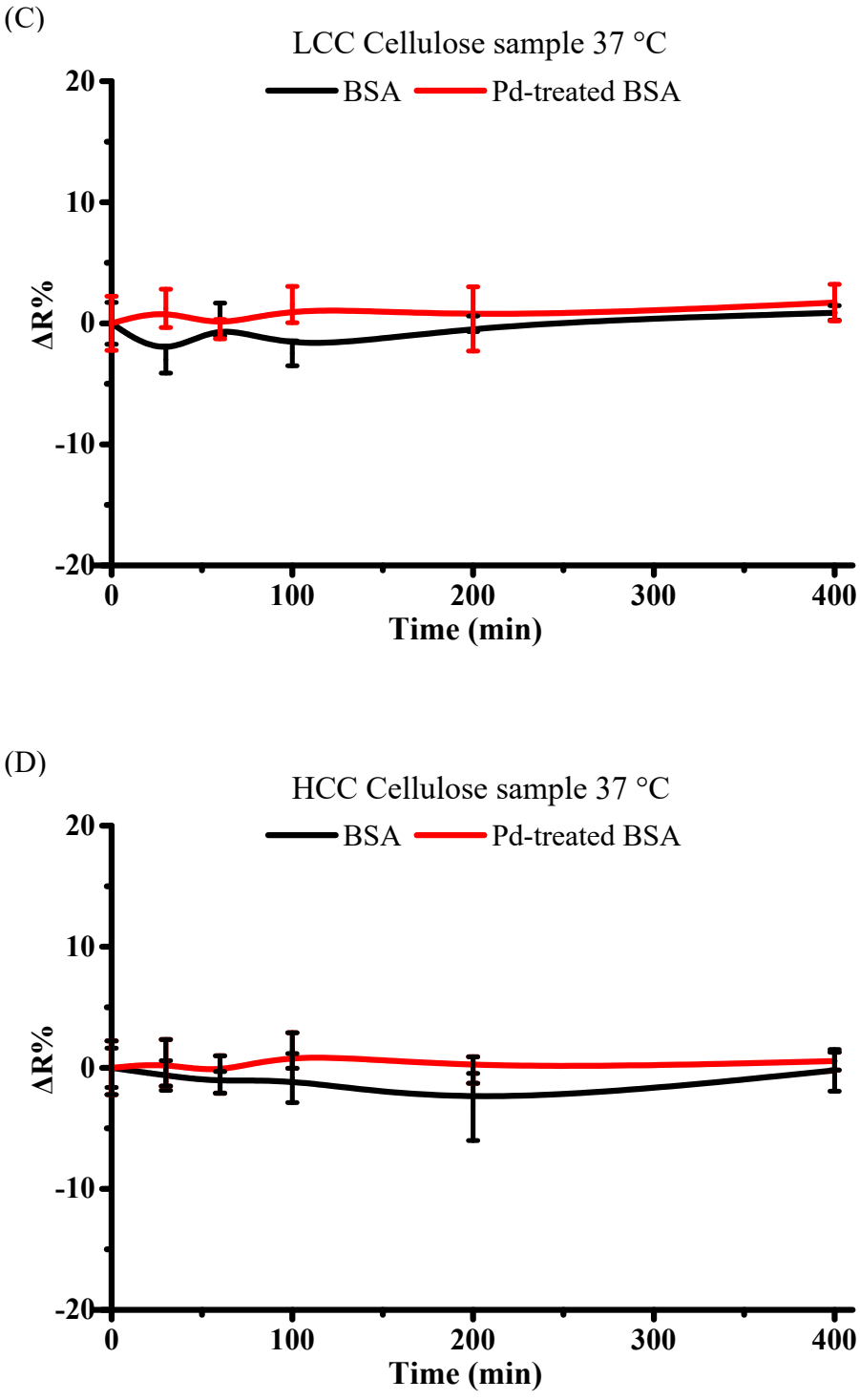

Figure 4-6 (continued). Roughness measurements 0.10-mg/mL results of BSA and Pd-treated BSA. (A) LCC cellulose sample at 25°C. (B) HCC cellulose sample at 25°C. (C) LCC cellulose sample at 37°C. (D) HCC cellulose sample at 37°C.

4.4.4 QCM-D Study of Cellulase and CBH I

In the study of hydrolysis of cellulose, it would be ideal if the first step — binding — occurred immediately and did not extend into the decrystallization step. Slow binding could interfere with a clear evaluation of the time-dependent change in roughness. To assess the kinetics of cellulase binding to cellulose, the QCM-D was used to measure the binding of cellulases to cellulose.

The results for native cellulase and NH cellulase are shown in Figure 4-7A. The initial decrease in the resonance frequency of the QCM-D crystal indicates a mass increase of the sensor. Application of both 0.10-mg/mL native cellulase and NH cellulase decreased the resonance frequencies of the sensors immediately. For native cellulase, the decrease was followed by an increase and then a plaeateu. By contrast, for NH cellulase, the decrease was followed simply by a plaeateu.

The results for native CBH I and NH CBH I are shown in Figure 4-7B. For both native CBH I and NH CBH I, the initial decreases were swift. For native CBH I, the decrease was followed by an increase and then a plaeateu. By contrast, for NH CBH I, the decrease was followed simply by a plaeateu.

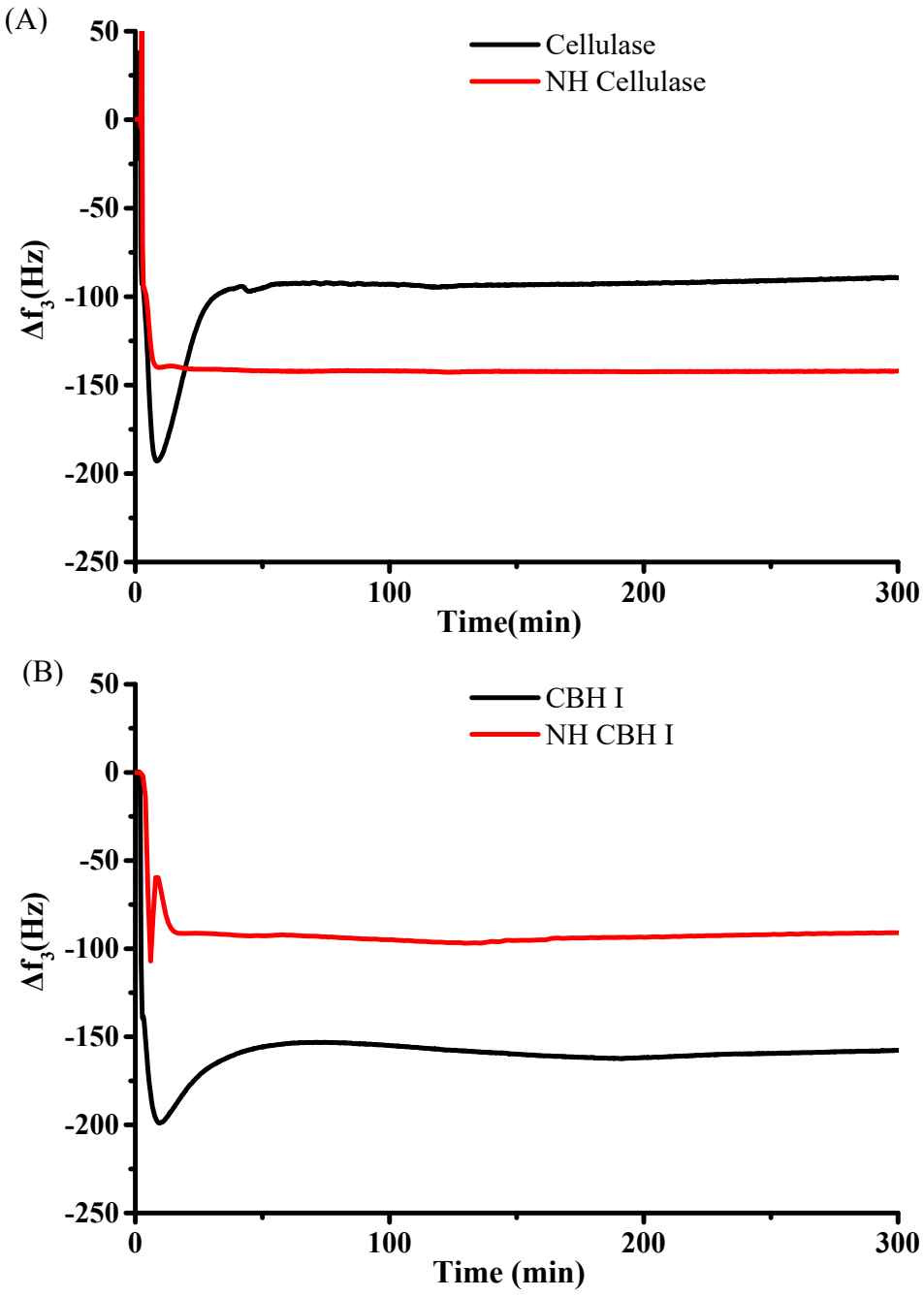

Figure 4-7. QCM-D study of 0.10-mg/mL native cellulase and NH cellulase, native cellulase and NH CBH I, and BSA and Pd-treated BSA at 37°C.
(A) Native cellulase and NH cellulase. (B) Native CBH I and NH CBH I. (C) BSA and Pd-treated BSA. (D) NaOAc buffer rinses after QCM-D study with native cellulase, native CBH I, and BSA.

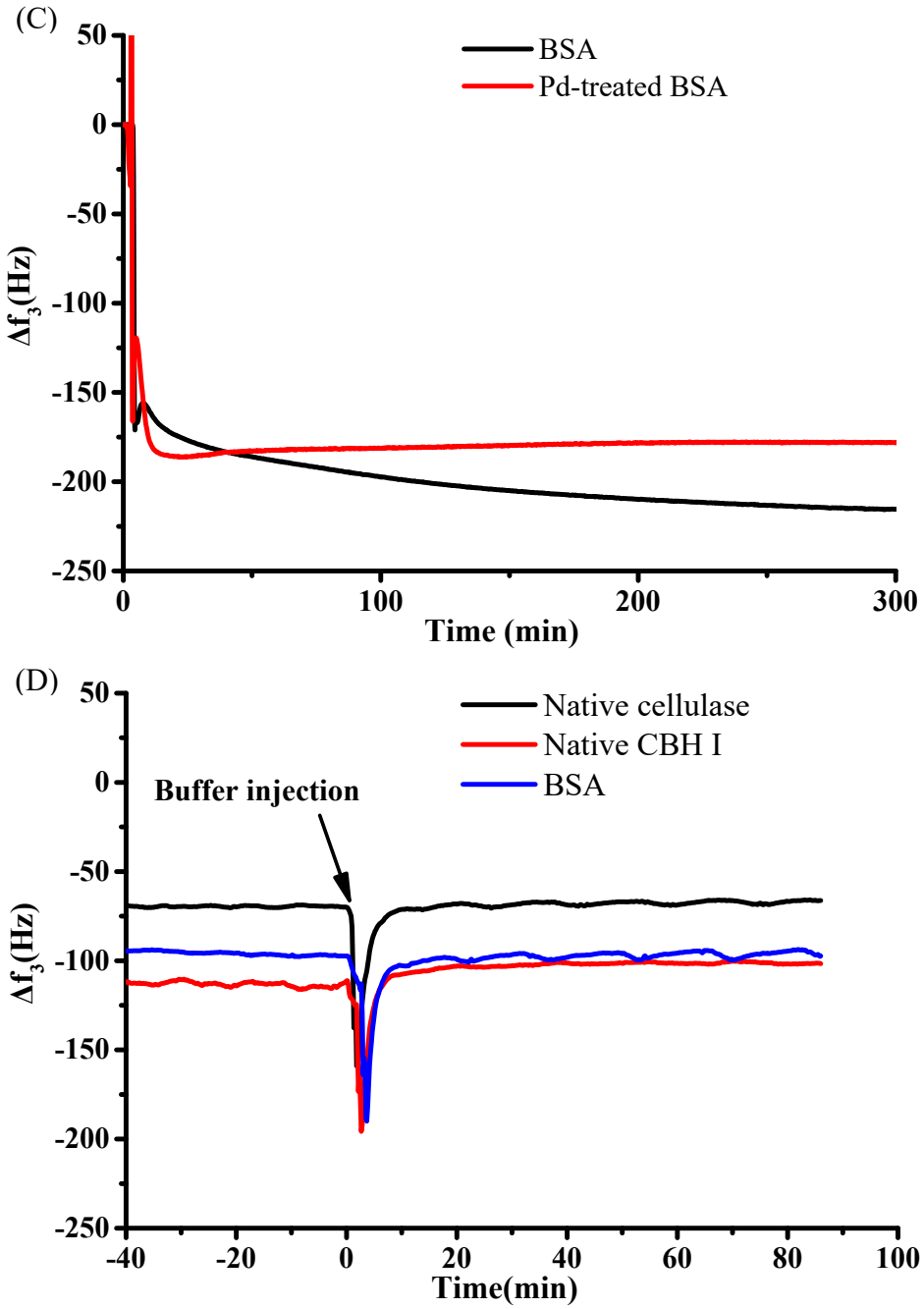

Figure 4-7 (continued) QCM-D study of 0.10-mg/mL native cellulase and NH cellulase, native CBH I and NH CBH I, and BSA and Pd-treated BSA at 37°C.
(A) Native cellulase and NH cellulase. (B) Native CBH I and NH CBH I. (C) BSA and Pd-treated BSA.
(D) NaOAc buffer rinses after QCM-D study with native cellulase, native CBH I, and BSA.

The results for BSA (the blank) and Pd-treated BSA are shown in Figure 4-7C. Similar to the cases of cellulase and CBH I, the frequency of the QCM-D sensor decreased immediately after additon of BSA and then reach a plateau. The Pd-treated BSA demonstrated a similar hehavior (Figure 4-7C).

In summary, all proteins (native cellulase, NH cellulase, native CBH I, NH CBH I, BSA, and Pd-treated BSA) used in the experiments adsorb rapidly to the cellulose surface. For all proteins, the plaeatues were reached within minutes, sometimes as little as 10 minutes.

The effect of a buffer rinse on the adsorbed proteins (native cellulase, native CBH I, and BSA) was also examined by means of QCM-D (Figure 4-7D). In the experiment, the buffer solution was used to rinse the sensor surfaces after protein binding. Except for the initial perturbation, no change of the resonance frequency caused by the rinse was observed.

4.5 Discussion

In this section of the dissertation, a study explored the use of surface topography (i.e., roughness) to examine the interaction between cellulase and cellulose is discussed.

Figure 4-5 shows that when native cellulase and native CBH I are applied, the roughness of the cellulose surface increases and then decreases, a behavior that suggests that there are two separate activities of the enzyme, producing two counteracting effects on roughness: a relatively fast process that increases the roughness and a slower one that decreases the roughness. By contrast, NH cellulase and NH CBH I only increased and did not decrease the roughness of cellulose (Figure 4-5), suggesting that the roughness-decreasing activity is absent from these non-hydrolytic (NH) cellulases. Since the

hydrolytic cleavage activity of NH cellulase and NH CBH I has been quenched (Figure 4-4), it can be assumed that it is hydrolytic cleavage that decreases the roughness of the cellulose surfaces.

In addition to hydrolytic cleavage, overall hydrolysis of cellulose by cellulase contains two steps: initial binding and decrystallization (Figure 1-10). As described before, BSA was chosen as a blank, because of its similar size and mass to those of cellulase and CBH I. The initial adsorption of BSA to cellulose, as indicated by means of QCM-D, was similar qualitatively and quantitatively, to the initial adsorption of native cellulase and native CBH I to cellulose. As shown in Figure 4-6, adsorption of BSA to cellulose does not show any significant effect on the surface roughness of the cellulose. Thus, the initial binding of cellulases and CBH Is to cellulose surface, a simple adsorption of a protein to cellulose, is not likely to cause any measurable change in the surface roughness.

Because the hydrolytic cleavage caused the decrease in roughness, the activity that generates the increase in roughness can be assumed to be the decrystallization. Comparisons of the topographic difference caused by native cellulase and NH cellulase, or native CBH I and NH CBH I established topographic evidence of the ability of decrystallization ability to increase the surface roughness of the cellulose substrate.

The effects of the following three factors on the ability of cellulase and CBH I to modify the surface of cellulose were also examined: reaction temperature, synergistic effect of the cellulase mixture, and CI% of the substrate.

The overall hydrolysis of both cellulase and CBH I increases as the temperate increases from 20°C to 50°C[222–226]. Thus, when the temperature of the experiments was

increased from 25°C to 37°C, the enzymatic activities of native cellulase and native CBH I would be expected to increase. The ΔR% curves confirmed this expectation. The results for the LCC cellulose samples at 37°C are shown in Figure 4-5C. Compared with roughness measurement results for the LCC cellulose samples at 25°C (Figure 4-5A), both native cellulase and native CBH I are capable of smoothing the cellulose surface to lower minimum ΔR%-values at 37°C, and those minima ΔR% are reached more quickly compared with those at 25°C. The extended decrease of ΔR% and the more rapid development of ΔR% clearly indicated that both native cellulase and native CBH I exbihit an enhanced modification of the surface at 37°C than at 25 °C. Similarly, for HCC cellulose samples, both native cellulase and native CBH I exhibit an enhanced modification of the surface at 37°C (Figure 4-5D) than at 25 °C (Figure 4-5B).

The native cellulase used in the experiment was a mixture of CBH (~70%, 40 – 60% CBH I), EG (~25%), and β-glucosidases (~2%)[193]. At the same concentration (0.1 mg/mL), the overall hydrolysis of native cellulase (mixture of multi-types of cellulase) is expected to be higher than that of individual cellulase (in this case, native CBH I) due to the synergism of the mixture. The results for the LCC cellulose samples at 25°C are shown in Figure 4-5A. Native cellulase is capable of smoothing the cellulose surface to a lower minimum ΔR%-value, and this minimum ΔR% is reached more quickly compared with that induced by native CBH I. The extended decrease of ΔR% and the more rapid development of ΔR% clearly indicated that native cellulase exbihits an enhanced modification of the surface than does native CBH I. Similarly, for HCC cellulose samples at 25°C (Figure 4-5B), LCC samples at 37°C (Figure 4-5C), and HCC samples at 37°C

(Figure 4-5D), native cellulase exhibits an enhanced modification of the surface compared with native CBH I.

The crystallinity of the cellulose substrate is a crucial factor in influencing the activity of cellulase. It is widely observed that the higher the crystallinity, the more difficult the hydrolysis[209,227]. High concentration cellulose (HCC) samples have higher CI% than low concentration cellulose (LCC) samples (Table 4-1), so the overall hydrolysis of native cellulase and native CBH I is expected to be higher on LCC cellulose samples than on HCC cellulose samples. The results for the LCC cellulose samples at 25°C are shown in Figure 4-5A. The roughness measurements for the LCC cellulose samples at 25°C (Figure 4-5B) show that both native cellulase and native CBH I are capable of smoothing the cellulose surface to a lower minimum ΔR%-value, and those minimum ΔR%-values are reached more quickly compared with those for HCC cellulose samples. The extended decrease of ΔR% and the more rapid development of ΔR% clearly indicate that both native cellulase and native CBH I exbihit an enhanced modification of the surface of LCC cellulose samples compared with that of HCC cellulose samples. Similarly, at 37°C, both native cellulase and native CBH I exhibit an enhanced modification of the surface of LCC cellulose samples (Figure 4-5C) compared with that of HCC cellulose samples (Figure 4-5D).

Overall, this series of experiments has shown that the increase in reaction temperature and the involvement of multi-types of cellulases (cellulase mixture as the native cellulase in current study) enhanced the ability of cellulases to modify cellulose surfaces both in rate and extent change in roughness. An increase in crystallinity reduced the effectiveness of the cellulases in modifying the surface of cellulose. In summary, this

approach has provided an effective tool for assessing the effect of cellulases on the surface topography of cellulose.

4.6 Conclusion

A surface-topography-based method was employed for characterizing the effect of cellulases on the surface topography of cellulose. With this approach, experimental evidence of the decrystallization, so far elusive to the cellulase research community, is successfully established. It is determined that the decrystallization can roughen the surface of the cellulose substrate and hydrolytic cleavage can then smooth this surface. It is the author's aspirations that these findings will inspire future efforts with the use of such approaches in the mechanistic study of cellulase actions on cellulose.

Chapter 5: Cellulose Bilayers

5.1 Introduction

Constituting the different forms of cellulose, are molecular chains which are tightly aggregated into microfibrils via strong intra- and inter- molecular hydrogen bonds and van der Waals forces. The hydrogen bonding network endows specific properties of cellulose I and II on both the macroscopic and nano scale, attracting the lively interest of researchers. In recent decades, nanotechnology has provided novel tools for researchers to study cellulose at nano and molecular scales. The most common method to obtain cellulose crystals in nanosize is through the hydrolysis of cotton, ramie, hemp, sisal, palm, bacterial cellulose, and Tunicates[228–234]. The resulting cellulose nanocrystal is in the form of cellulose I[18,41,62,235,236]. Cellulose fibers, one form of cellulose I crystal, with heights from 0.4 nm (a monolayer of cellulose) to 2.7 nm (multilayers of cellulose) can be prepared using a TEMPO/NaBr/NaClO oxidation system with ultrasonication[14,237,238]. Shingo Yokota *et al.* separated single cellulose chains by dissolving cotton cellulose in a cupri-ethylenediamine solution and characterized the single-chain cellulose by AFM[239].

Ionic liquid is a type of solvent capable of dissolving cellulose completely[118,205,240,241]. By varying the concentration of cellulose of a cellulose/ionic liquid solution, single chain fibers and nanodots of cellulose could be obtained[242]. The prepared cellulose nanocrystals could be used as a model for cellulose for studying the hydrolysis of cellulose by cellulases at a nanoscale. Igarashi *et al.* employed high-speed atomic force microscopy for a real-time visualization of hydrolysis of high crystalline cellulose by individual cellulase molecules[168,243]. Bubner *et al.*[195] prepared an especially

smooth cellulose substrate and studied the dynamics of enzymatic hydrolysis of cellulose according to the varying roughness of the cellulose substrate.

The crystal structure has been determined for a variety of cellulose allomorphs, such as I_α, I_β, II, III_I, IV_I, and IV_{II}[21,22,33,244,245]. In the past decade, a significant amount of modeling efforts, both quantum[246–248] and classic calculations[249–251], have been employed to study cellulose. There is no doubt that such endeavors have helped to advance the understanding of cellulose structure. At the same time, they have also led to some controversies (e.g., whether or not the cellulose microfibril is a twisted entity). The extension of such investigations, on both time scale and size scale, is necessary to provide an accurate description of the properties of cellulose.

Some simulations have demonstrated that removing one cellulose molecule or deconstruction of the crystalline cellulose I requires energy ranging from about 8.4 kJ/mol per glucose unit to about 46.02 kJ/mol per glucose unit depending on the environment surrounding the crystalline cellulose[240,252–254]. Cellulose chains mutually approach and form aggregates through hydrogen bonding in non-aqueous environments. In aqueous environments, such as a bio-system, cellulose molecules are separated by water molecules and there is no direct hydrogen bonding exists between the cellulose chain molecules. Therefore, the behavior of cellulose molecules in aqueous environments has drawn particular interest[255]. Heiner and Teleman[256] studied the interface between the crystal face of cellulose I and water by molecular dynamic simulations with cellulose coordinates obtained from electron diffraction data. They found that only the topmost surface layer of the crystalline cellulose is structurally affected by water outside the surface, reflecting the strength and rigidity of the cellulose crystal[257]. The structure of the

topmost surface layer of cellulose is only mildly different from that of the bulk. Aulin *et al.*[258] undertook a systematic study of cellulose by swelling different cellulose model films in water by the means of QCM-D. The results indicate that cellulose films can be swelled in water and the difference in both crystalline ordering and the mesostructure of films affects the swelling process of cellulose films. However, although these studies have shown that cellulose can be swelled in an aqueous environment, few experimental details at a molecular level have been reported.

Cellulase, a type of enzyme, could hydrolyze cellulose in 3 steps:[49] (a) initial binding of cellulase to cellulose; (b) decrystallization of cellulose aggregation; and (c) hydrolytic cleavage of cellulose molecule chain. The detailed molecular mechanisms of these enzymatic activities have still not been convincingly elucidated. Cellulose decrystallization is a free-energetically unfavorable process, cellulases must overcome a free energy barrier to decrystallize an individual cellulose chain from the surface of a crystalline fibril. Understanding how cellulase disrupts the cellulose crystallinity is still a challenge. One well-documented explanation is that the catalytic domain of cellulase contains hydrophobic and polar residues which form favorable interactions with a cellulose chain. This favorable ligand-binding free energy allows cellulase to form a catalytically active complex with cellulose despite a thermodynamic barrier to the removal of a cellulose chain from the crystal[49,259–261]. Further investigations are needed to explain the disruption of cellulose aggregation by cellulase at a molecular level.

There has been a growing interest in understanding the mechanism of cellulose breakdown and its interaction with water, acids, and cellulases in an effort to optimize the cellulose digestion process. Water, a solvent used in most biofuel production, may play a

major role in hydrolysis. To better study the effect of water molecules on the decrystallization, a type of cellulose particle was developed in the current study. This cellulose particle, termed as cellulose bilayer, consists of two cellulose layers. Typical dimensions of one cellulose bilayer are 20 nm long, 10 nm wide, and 0.8 nm height, thus, cellulose bilayer could be considered as nanoparticle. It is a promising model for studying the interactions between cellulose and water, as the height of the nanoparticle is equal to the sum of the height of two layers of cellulose. Any change in the bilayer structure can be measured with AFM imaging at a molecular level of sensitivity and resolution.

In the current study, molecular dynamics simulation and AFM imaging techniques are combined to study the structural changes of cellulose bilayer nanoparticles at the molecular level. Ionic liquids (ILs) were used to dissolve cellulose and prepare cellulose solution. Bilayer cellulose particles were prepared by regeneration of cellulose solid particles from cellulose solution on mica. The heights of the cellulose bilayer nanoparticles and the distances between two cellulose layers in the aqueous environment were characterized by means of AFM. Molecular dynamics simulation based on the bilayer cellulose in an aqueous environment was used to provide a semi-quantitative estimation of the energy required for separating cellulose bilayer.

5.2 Materials and Methods

5.2.1 Materials

Microcrystalline cellulose, 1-butyl-3-methylimidazolium chloride, sulfuric acid (H_2SO_4), and (3-glycidyloxypropyl)trimethoxysilanem were purchased from Sigma-Aldrich (St. Louis, MO).

5.2.2 Preparation of Cellulose Nanoparticles

To prepare nanoparticles, microcrystalline cellulose (MCC, 50 mg) was dissolved in the ionic liquid 1-butyl-3-methylimidazolium chloride (5g) with stirring at 80ºC for 4 hours to a concentration of 10 mg/g. This ionic liquid is not only a good solvent for microcrystalline cellulose, but also contains no water that could inadvertently hydrolyze the cellulose. Ionic liquids have excellent thermal stability, are liquid over a wide temperature range, and are good solvents for a range of polar and non-polar compounds,[118,205,241] including cellulose. Prior to deposition of cellulose, a freshly cleaved mica sheet (1cm × 1cm) was treated with an aqueous solution of (3-glycidyloxypropyl)trimethoxysilane (0.50% v/v) for 5 minutes, was rinsed thoroughly with DI-water, and was dried in air. The modified mica was then placed into the cellulose/ionic liquid solution (5.05 g), and then 1 μL H_2SO_4 was added and the solution was maintained at 80 ºC. After 1 hour, the mica sheet was removed from the cellulose solution. Gentle contact of the mica sheet with DI-water caused the residual cellulose to aggregate into crystalline cellulose nanoparticles. The mica sheet containing the cellulose nanparticles was air dried and kept at 60ºC for 4 hours for further drying.

5.2.3 Sample Treatment and Imaging

To characterize the morphology of cellulose nanoparticles on mica, AFM imaging was performed on a Nanoscope IIIA multimode atomic force microscope (Digital Instruments, Inc.). Samples were scanned in tapping mode in air with silicon nitride microcantilevers (model no.: MLCT) manufactured by Veeco (Camarillo, CA) with a nominal spring constant of 0.05 N/m. Both height images and amplitude modes were obtained. The height of cellulose nanoparticles was analyzed with image-processing

software. The mica sheet containing cellulose nanoparticles was affixed with double-sided tape to a steel sample mounting disk. The disk was placed on the atomic force microscope and was stabilized during the experiment. Cellulose nanoparticles were first characterized by AFM in the dry state. After this, the nanoparticles were check for evidence of hydration by exposure to water; a few drops of DI-water were placed on the test area and the region was kept in an aqueous environment for various durations. Following this, water droplets were removed with blown air. The resulting nanoparticles were again characterized with AFM imaging.

5.2.4 Molecular Dynamics Simulation Method

A bilayer of cellulose II (Figure 5-1) was built based on its crystal structure derived from a neutron diffraction experiment[33]. Each of the antiparallel *origin* and *center* layers contains six glucan chains in the *a*-direction of the crystalline lattice; there are 16 glucose residues in each chain. This bilayer was then placed at the center of a rectangular box filled with TIP3 water molecules[262]. The size of the box was chosen to allow a 10-Å solvation shell in every direction, except for a 24-Å solvation in the +z direction, as the center layer would be pulled in this direction during the steered molecular dynamics (SMD). Periodic boundary conditions were imposed on this system throughout the study. The C35 force field[263,264] was used for the cellulose II bilayer and the simulations were performed with the NAMD package[265]. In the molecular dynamics calculations, constraints were placed on the system to keep two cellulose II layers parallel to each other. With time-steps of 2 fs, the solvated system was heated to 300 K within 60 ps, followed by a 40-ps equilibration.

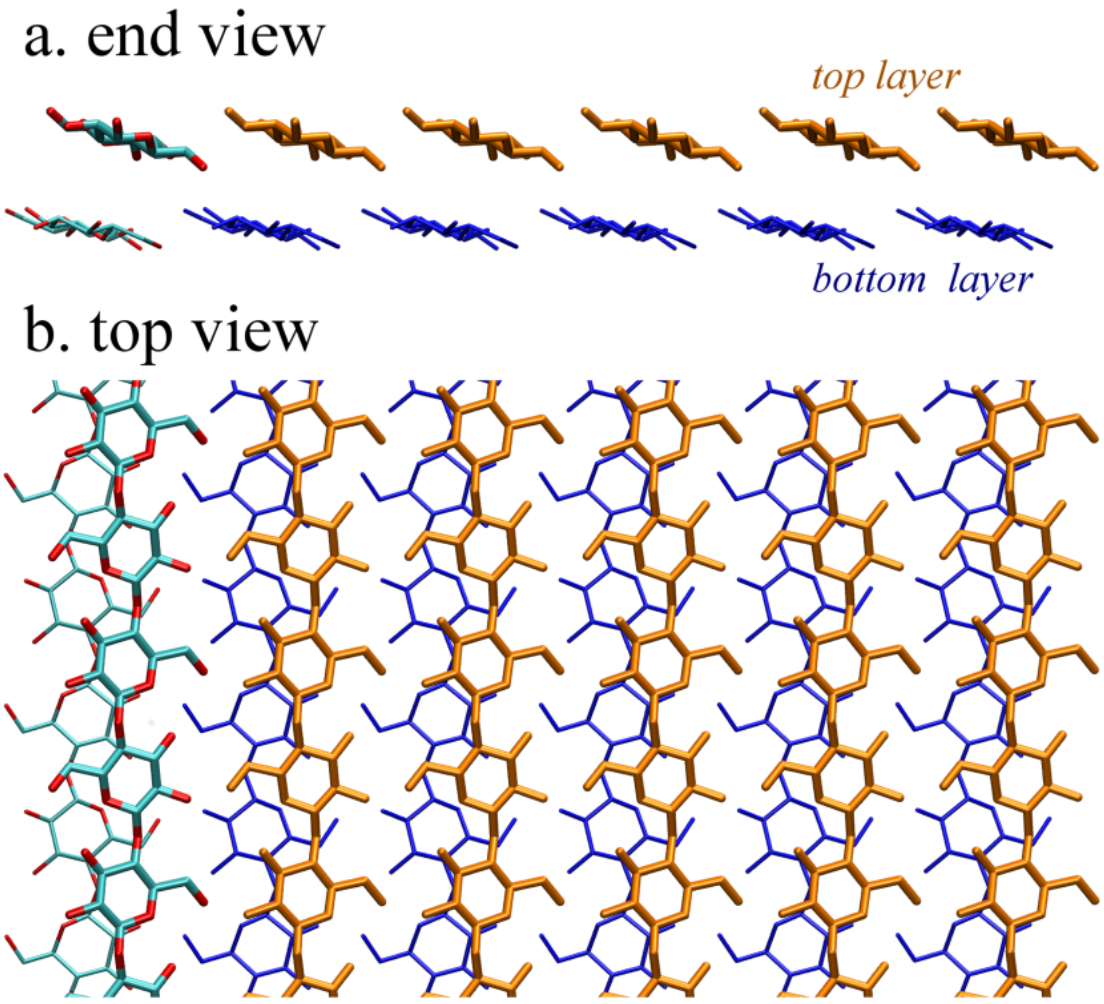

Figure 5-1. End (a) and top (b) view of the cellulose II bilayer model.
Water molecules and hydrogen atoms are omitted for clarity. The top layer was subject to constant velocity pull in the steered molecular dynamics (SMD), while the bottom layer was fixed.

After the system was equilibrated, an SMD procedure was performed on the center layer. All atoms in this layer were pulled with a spring in the +z direction at a constant speed of 0.001 Å/ps. The spring constant was set to 836.8 kJ/mol·Å^2 (140 N/m). The trajectory for the SMD simulation was collected for 12 ns (Figure 5-2).

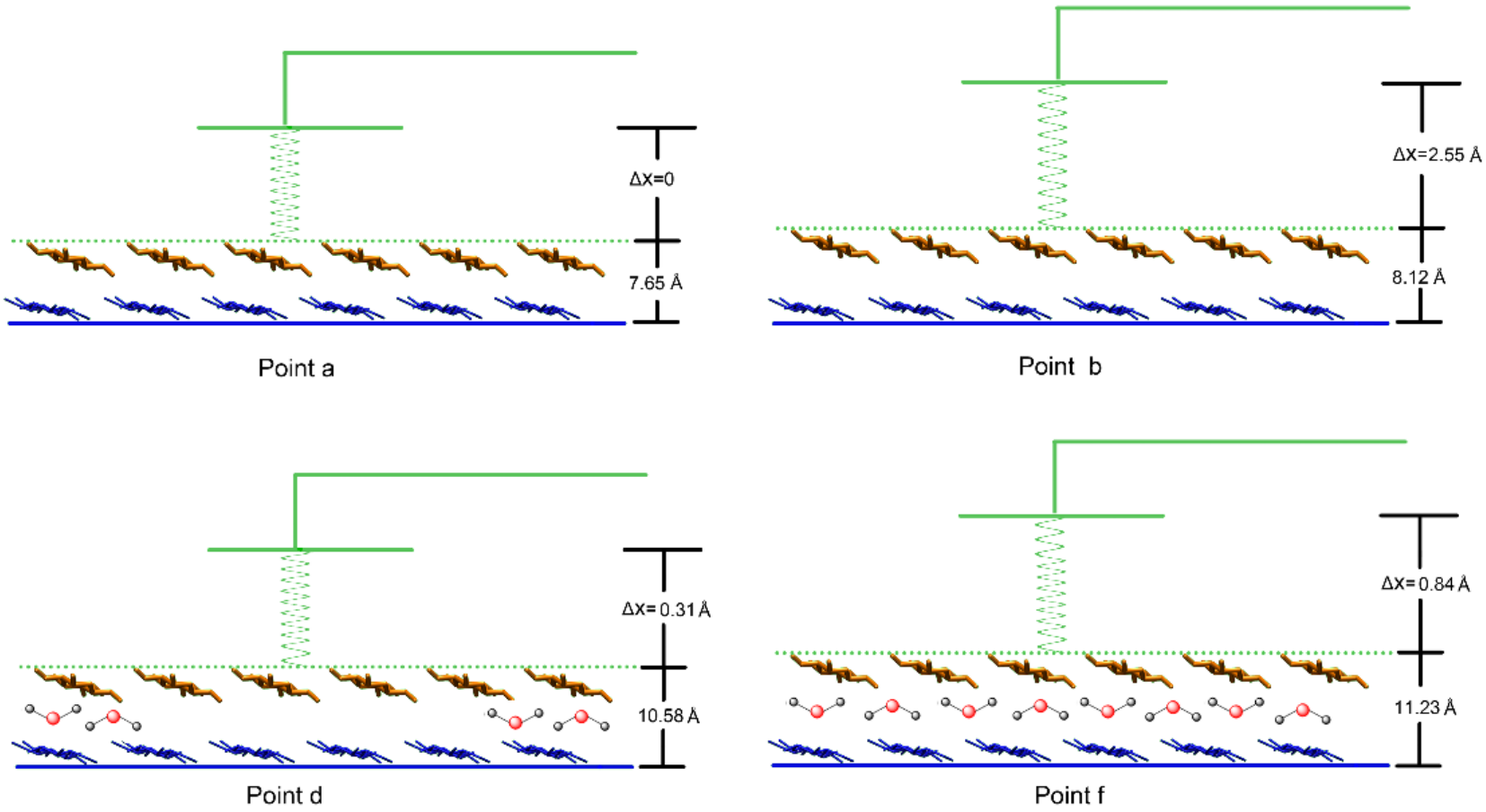

Figure 5-2. Scheme description of the steered molecular dynamics (SMD) procedure.
Point *a* shows the original state of cellulose II bilayers—*origin* (blue) and *center* (yellow). Points *b*–*f* show the process of water molecules entering between cellulose layers while the center layer is pulled from the origin layer.

Considering that one of the primary aims in the current study is to determine how water affects the cellulose bilayer separation process, a simulation *in vacuo* was generated as a control with the same parameters and configurations as in water.

5.2.5 Results of Calculation

The energy to separate cellulose bilayer, either in water or *in vacuo*, can be calculated by means of integral calculus:

$$E = \int_{x_1}^{x_2} F \, \mathrm{d}x + (U_{x1} - U_{x2}) \quad 5\text{-}1$$

where E is the energy to separate cellulose bilayer, x_1 is the start point in water or *in vacuo*, x_2 is the end point in water or *in vacuo*, F is the separating force, U_{x1} is the elastic energy of the spring at the start point, and U_{x2} is the elastic energy of the spring at the end point.

In the simulation, there are 6 × 16 glucose residues in one layer. The formula used to compute energy per mol glucose (E_0) is:

$$E_0 = \frac{EN_A}{6 \times 16} \quad 5\text{-}2$$

The elastic energy (U) of the spring can be calculated as:

$$U = \frac{1}{2} k \Delta x^2 \quad 5\text{-}3$$

where k is the spring constant of the spring and Δx is the deformation of the spring.

The kinetic energy (E_k) can be calculated as:

$$E_K = \frac{1}{2} m v^2 \quad 5\text{-}4$$

where m is the mass of the cellulose and v is the velocity of the top cellulose layer.

5.3 Results and Discussion

5.3.1 Morphology of Cellulose Nanoparticles

Atomic force microscope (AFM) is an effective tool to characterize cellulose nanoparticles when the particles are anchored to an extremely flat, smooth surface. In this study, the mica was first modified by (3-glycidyloxypropyl)trimethoxysilane, as described earlier. Figure 5-3 shows the proposed mechanism of (3-glycidyloxypropyl)trimethoxysilane binding to a surface, as envisioned by the manufacturer of the silane. Figure 5-4a and Figure 5-4b show the surface morphology of the mica sheet with and without modification of the silane. Clearly, the bare mica surface was smooth and the mean roughness was found to be 5.5×10^{-2} nm. The mean roughness of the mica sheet after modification increased to 11.3×10^{-2} nm. The results suggest that (3-glycidyloxypropyl)trimethoxysilane deposited on the mica and formed a film.

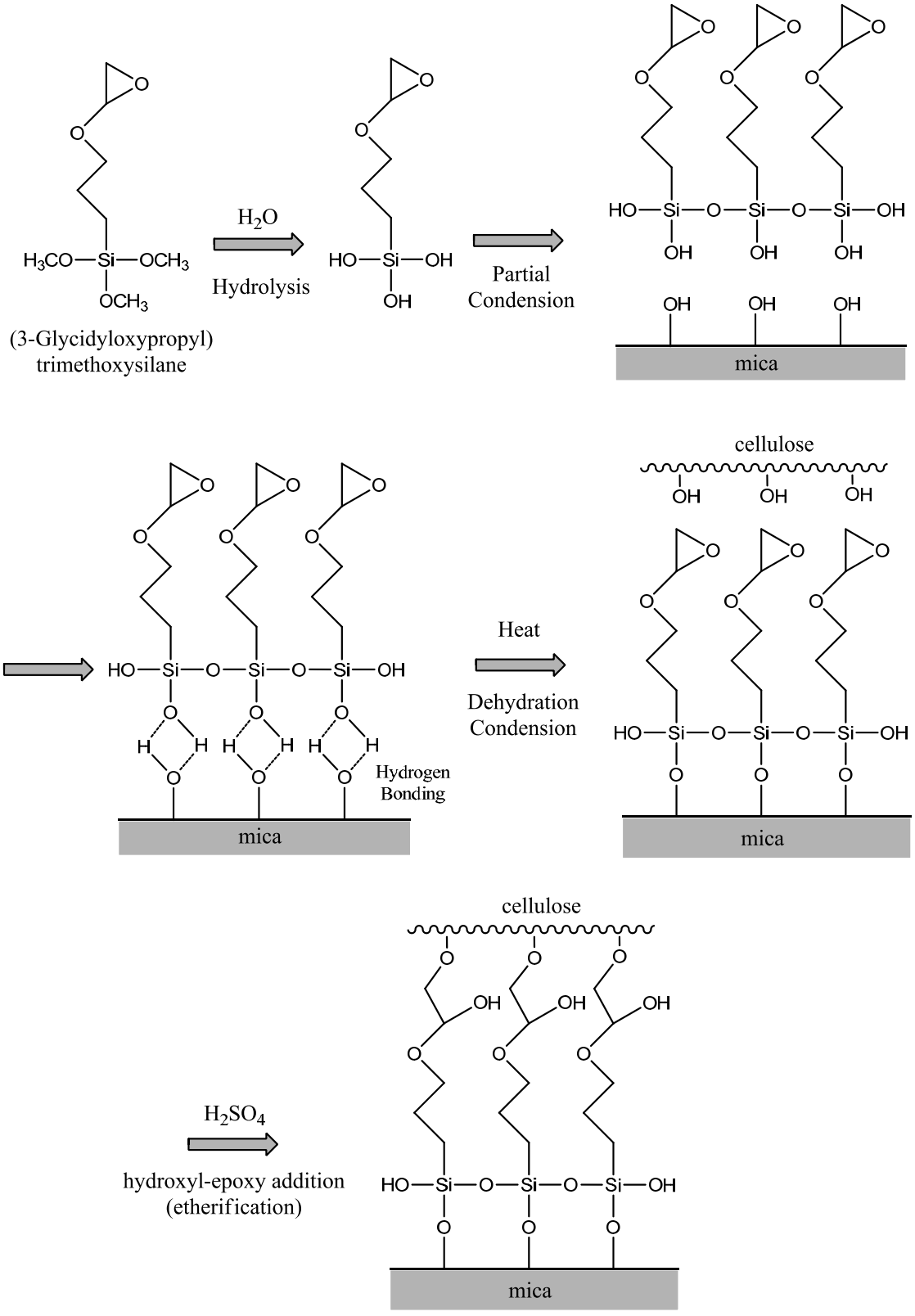

Figure 5-3. Suggested mechanism of action with (3-glycidyloxypropyl)trimethoxysilane as a coupling agent on mica.

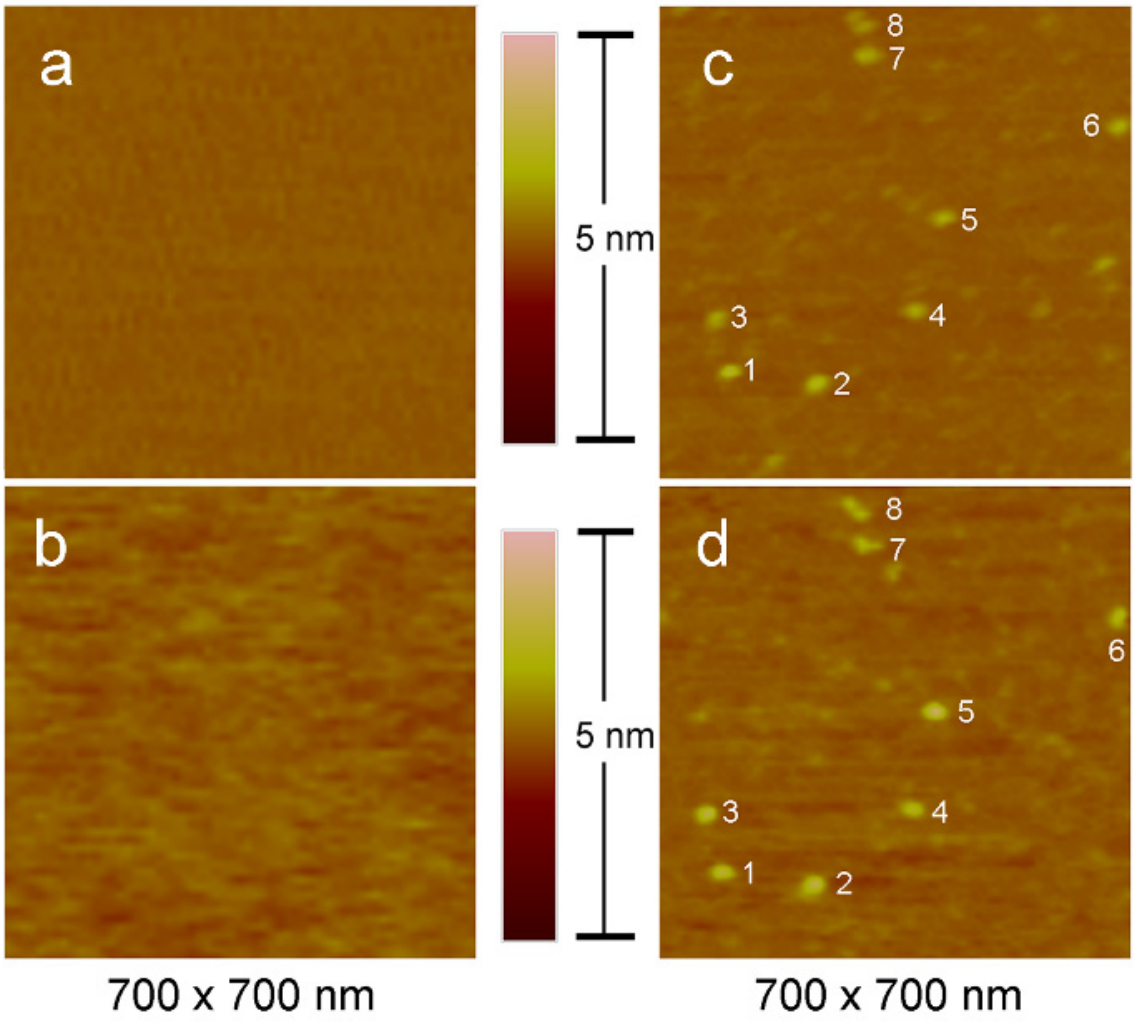

Figure 5-4. Atomic force microscope images of bilayer samples.
(a) Mica sheet surface. (b) Mica surface with modification. (c) Cellulose nanoparticles. (d) Cellulose nanoparticles treated with water for 10 min

The nanosize cellulose particles were obtained by regeneration of the cellulose/ionic liquid solution in water. After drying thoroughly, the morphology of dry cellulose nanoparticles was characterized by means of AFM (results shown in Figure 5-4c). The nanoparticles were generally ovoid, with dimensions of ~ 40 nm × 15 nm × 1 nm. The heights of these particles range from 4.35 Å to 12.42 Å (detailed data listed in Table 5-1). These values are comparable to the height of a cellulose monolayer (~4 Å), a

bilayer (~8 Å), or a trilayer (~12 Å), respectively[14,266]. After these nanoparticles were treated with water, the heights of some cellulose particles were changed significantly. Figure 5-4d shows the surface morphology of cellulose nanoparticles after hydration. For example, the height of the particle labeled as No. 5 in Figure 5-4 increased from 8.33 Å to 15.56 Å, with an increase of 7.23 Å. Meanwhile, particles No. 7 and 8 in Figure 5-4 showed almost no increase in height. According to some reported results[256,258], the variation in height of cellulose particles after exposure to water is related to variation in amount of water molecules diffused into the cellulose layers. The current study hypothesizes that water molecules can disrupt the Hydrogen bonding network between cellulose layers and this behavior would in turn decrease the energy required to separate the bilayer structure and promote deconstruction of the cellulose. To support this hypothesis, a molecular dynamics simulation of bilayer cellulose in a water environment was carried out to provide an estimate of the energy needed for the separation of the bilayer structure.

Table 5-1. Height before and after treatment of cellulose II particles with DI-water shown in Figure 5-4.

Sample	Initial Height/Å	After Treatment Height/Å	Increment/Å
1	12.42 ± 0.32	13.27 ± 0.50	0.85 ± 0.59
2	11.0 ± 0.45	15.25 ± 0.81	4.25 ± 0.93
3	7.43 ± 0.26	13.30 ± 0.29	5.87 ± 0.39
4	8.07 ± 0.24	10.51 ± 0.25	2.44 ± 0.35
5	8.33 ± 0.37	15.56 ± 0.48	7.23 ± 0.61
6	7.96 ± 0.26	10.62 ± 0.32	2.66 ± 0.41
7	7.71 ± 0.28	9.42 ± 0.49	1.71 ± 0.56
8	4.35 ± 0.10	4.47 ± 0.19	0.12 ± 0.21

5.3.2 Cellulose Bilayer Separation Process

After the constant velocity SMD trajectory was collected, the force-extension profile for this process was analyzed. Since the bottom center layer was fixed and the top origin layer was pulled, the extension of the top layer here represents how far it is from the bottom layer. For the purpose of an intuitive interpretation of the AFM monitoring results, the extension was converted into the height of these two layers. According to the data obtained, the initial heights of monolayer and bilayer cellulose in a stable state are 3.45 Å and 7.65 Å, respectively.

Figure 5-5 shows force vs. layer height and layer height vs. time profiles for the top layer as it was pulled further from the bottom layer in the simulation. Initially, the two layers were separated by 4.15 Å to be in a stable state and the height of the two layers was 7.65 Å (point *a* in Figure 5-5). Since the AFM was pulled at a constant velocity (1 Å/ns), a force gradually built in the spring attached to the AFM until the force accumulated to roughly 35,000 pN. At this moment, the top layer had moved upwards by 0.47 Å and the height of two layers reached 8.12 Å (point *b* in Figure 5-5). This height was maintained relatively unchanged. In stage I (from point *a* to *b*), the movement velocity of the top layer cellulose, calculated from the slope of the straight line *a*-*b* in Figure 5-5A, was 0.16 Å/ns. The velocity of the top layer was lower than that of the spring (1 Å/ns) because of the attractive force between the two layers of cellulose bilayer. When the force reached 35, 000 pN, the energy barrier of the attractive force between the two layers of cellulose bilayer was overcome. This led to swift movement in the top layer, covering a distance of 1.43 Å (to point *c*) in 0.14 ns. This suggests that the spring recovered from the deformation quickly with a speed of 10.21 Å/ns at this stage (stage II,

from point *b* to *c*). When the height of bilayer cellulose reached 9.55 Å (point *c*), the separation allowed for some initial diffusion of water molecules into the space between the layers. Both the large force acting on the top layer and the initial water diffusion led to fast cellulose layer separation at this stage (stage III, from point *c* to point *d*); the speed of the top layer cellulose was 11.88 Å/ns. The rapid, upward movement of the top cellulose layer was accompanied by a 10-fold decrease in the SMD force, from 35,000 pN to 3,500 pN. Simultaneously, the quick separation facilitated even swifter water diffusion. This rapid separation stage was followed by another slow separation process (stage IV, from point *d* to *e*) in which a monolayer of water fully filled the gap. Consequently, the height was further stretched to 10.75 Å to form a stable single hydration layer, sandwiched between the two layers of cellulose bilayer. The separation speed in stage IV is lower than that in stage III because the water layer functions like an adhesive that joins two layers of cellulose bilayer together. However, the strength of this adhesion is weaker than the interaction between the two layers of cellulose bilayer in their initial configuration. As a result, it took a shorter time for the two layers of cellulose bilayer to begin separating again at the end of stage V (0.32ns, from point *e* to *f*), and the SMD force peaked at 11,000 pN compared to 35,000 pN in stage I. With further separations, more water molecules diffused between the cellulose layers (stage VI, from point *f* to *g*) and formed the second hydration layer (stage VII, from point *g* to *h*). The adhesive effect of the double hydration layer greatly diminished compared to that of the single hydration layer. After a short period of negative SMD force, hardly any interaction held the cellulose bilayer together (stage VIII, from point *h* to *i*). The top layer moved at

the same speed as prescribed by the SMD (stage IX, from *j* to *k*). Hence, the AFM force merely fluctuated around zero pN.

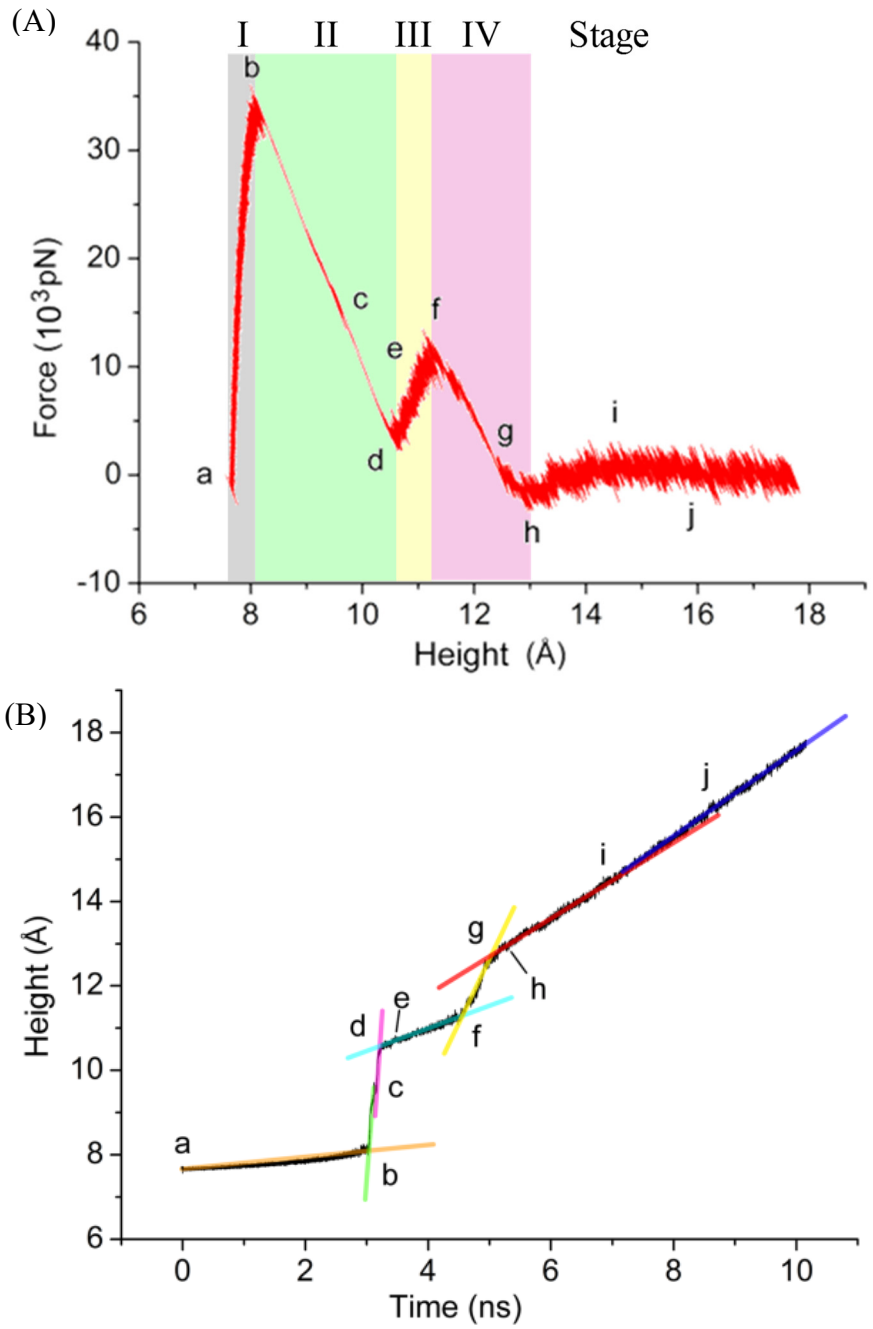

Figure 5-5. Force with bilayer height (A) and bilayer height with time (B) profiles from the SMD simulation.

The results indicate that the heights of bilayer cellulose, the heights of bilayer cellulose filled with a single hydration layer, and the heights of bilayer cellulose filled with a double hydration layer, are 7.65 Å, 10.75 Å, and 12.93 Å, respectively (diameter of a water molecule is about 2.75 Å). Compared to the height of particles shown in Figure 5-4, particles No. 3, No. 4, No. 5, No. 6, and No. 7 are likely bilayer cellulose particles. The particle No. 8 is probably a monolayer cellulose particle and the others are cellulose particles with multilayer of cellulose. After treatment with water, the height of all bilayer cellulose particles were increased. Based on these heights, it appears that particle No. 4 and No. 6 are filled with one layer of water molecule and particle No. 3 is filled with two layers of water molecule. The particle No. 5 is filled with more than two layers of water molecule. The particle No. 7 is likely in stage III, a fast cellulose layer separation stage. The height distributions of 100 particles treated for different time duration with water were compared and are shown in Figure 5-6. The initial heights of cellulose particles are around 5 Å, 8 Å, and 11.5 Å, corresponding to monolayers of cellulose, bilayers of cellulose, and trilayers of cellulose, respectively (Figure 5-6a)[14,266]. Upon hydration for 10 minutes, the height of bilayer cellulose was obviously increased and most of the heights were found to be around 11 Å, which is likely the height of bilayer cellulose plus one layer of water molecule (Figure 5-6b). Moreover, there were many particles with heights around 13.5 Å, which is likely the height of bilayer cellulose plus two layers of water molecule. When the duration of incubation with water increased, the number of particles with a height around 11 Å decreased while the number of particles with a height around 13.5 Å increased, suggesting the continuation of diffusion of water molecules into the space between two layers of cellulose bilayer. In summary, it is evident that cellulose

nanoparticles are able to absorb water to form either single or double hydration layers of water molecule between two layers of cellulose bilayer. More double hydration layers form with a longer incubation time. Throughout the entire experiment, the number of monolayer cellulose nanoparticles remained constant. This is consistent with the idea that hydration layers are formed between the layers of cellulose, not on the outer surface of cellulose or underneath the bottom layer of cellulose.

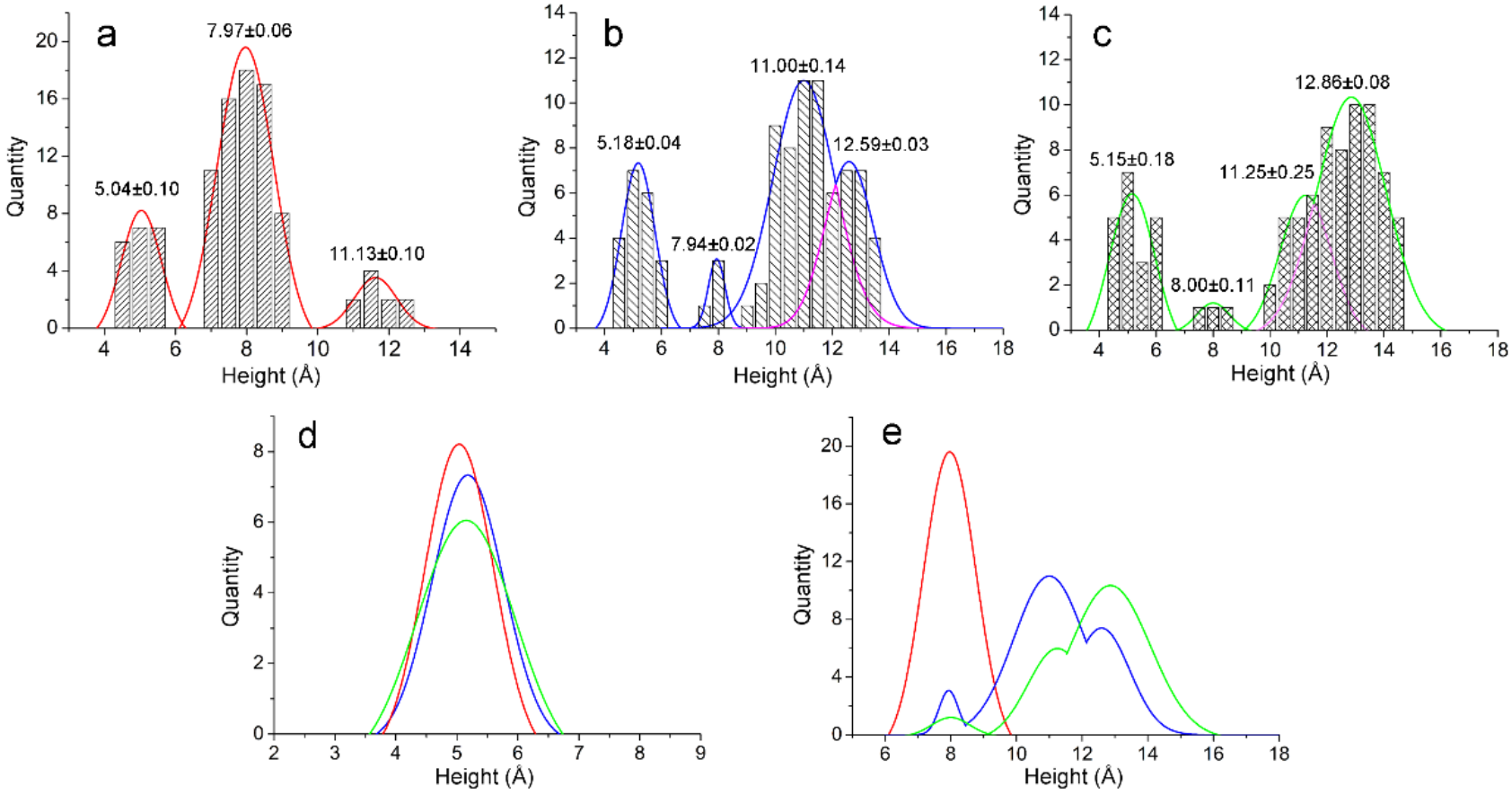

Figure 5-6. Height distributions of 100 particles with different treatment durations with water.
(a) Initial height distribution. (b) Height distribution after 10 min hydration. (c) Final height distribution after hydration. (d) Quantity change of cellulose monolayer structure. (e) Quantity change of cellulose bilayer and trilayer structures.

In order to explore how water affects the cellulose bilayer separation process, simulation results *in vacuo* were examined. The relationship between force and layer height *in vacuo* and in water are compared in Figure 5-7. *In vacuo*, the energy barrier of the attractive force at point *b* was the same as in water, about 35000 pN. However, from point *b* to point *d*, the force decreased faster in water than *in vacuo*, which is likely due to water molecules diffused in cellulose bilayers and supported the separation of two layers of cellulose bilayer. In the snapshot of the stage between point *b* and point *d*, it is shown that water molecules diffused into the cellulose layers (Figure 5-8 *b* to *d*). Nevertheless, as more water fills in and the adhesive effect of water increases, the support of water molecules to the separation of cellulose layers lessens (Figure 5-7 point *d*). At the same height, the attractive force between cellulose-water-cellulose in water gradually exceeds the attractive force between cellulose-cellulose *in vacuo* (from point *d* to point *f*), and the separation of cellulose-water-cellulose in water requires an stronger force (point *f* in water) than *in vacuo* at this time. After the height of cellulose bilayer reached 13 Å, the attractive force between the cellulose layers is almost zero both in water and *in vacuo*. As stable hydrated cellulose-water-cellulose structure readily formed in water, the separation of cellulose bilayer in water starts from stage III, rather than stage I *in vacuo*, thus, it requires far less force in water compared with *in vacuo*. The energy to separate cellulose bilayer was also assessed by means of integration. The area under the curve *in vacuo* between *a* and *j* is the energy needed to separate cellulose bilayer *in vacuo*. The area under the curve in water between *e* and *j* is the energy needed to separate cellulose bilayer in water.

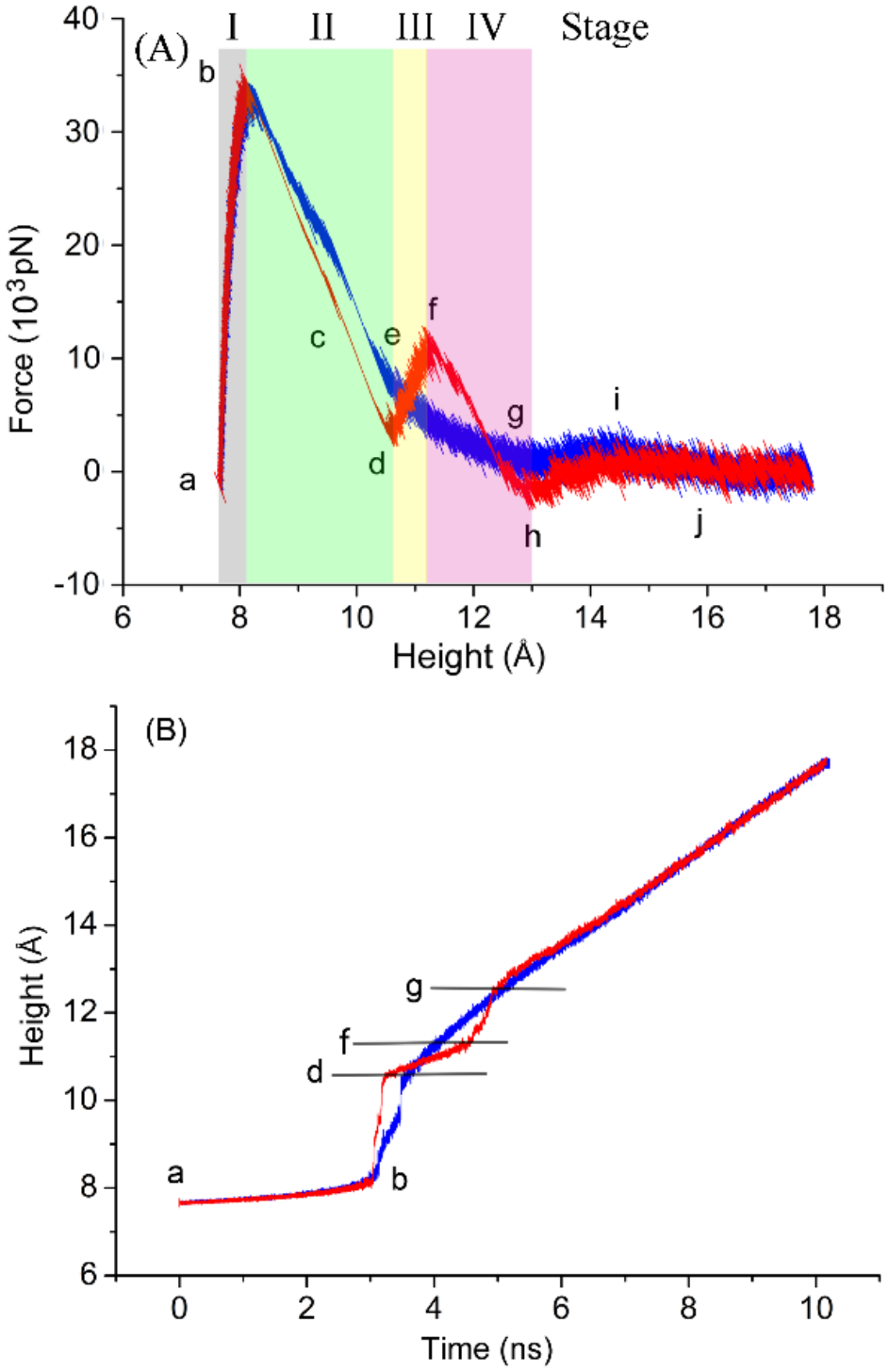

Figure 5-7. Force with bilayer height (A) and bilayer height with time (B) profiles from SMD simulation: in water (red) and *in vacuo* (blue).

The energy barrier of attractive force at point *b* was the same for *vacuo* and water experiments. From point *b* to point *d*, the force decreased faster in water than *in vacuo*. For point *f*, more force is required to separate cellulose chains in water than *in vacuo*.

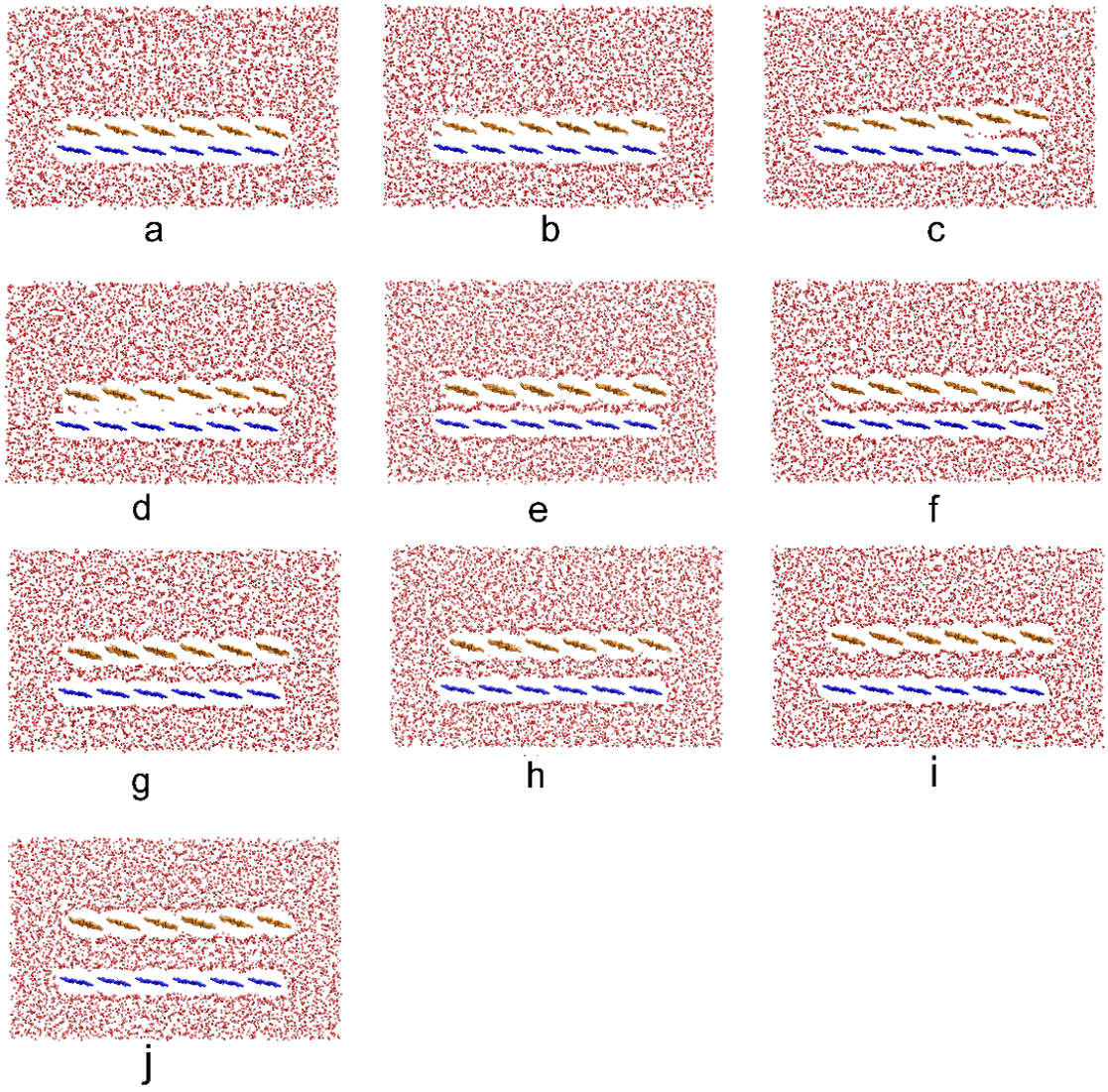

Figure 5-8. Snapshot of the SMD simulation at different durations in water.
Both the center layer (yellow) and origin layer (blue) of cellulose contain 6 glucan chains. When the center layer is pulled from the origin layer, water molecules (red) enter the gap between two layers.

The energy for separating cellulose bilayer is less than 7.34 kJ/mol per glucose in water and 46.08 kJ/mol per glucose *in vacuo*. These values are similar to those reported in recent simulation works[240,253,254]. The stacking of two units results in stabilization energies of 38.37 to 61.63 kJ/mol in cellulose I_β[254]. To peel off the corner glucan chain

from the cellulose microfibril, the free-energy cost of deconstructing a glucan from crystalline cellulose in water is about 7.95 kJ/mol per glucose residue[240]. This suggests that the diffusion of water molecules into cellulose layers decreases the attractive force of two layers of cellulose bilayer by more than three-fold and the energy of separating two layers of cellulose bilayer by more than six-fold. When double hydration layers are formed between two layers of cellulose bilayer, the separation of two layers of cellulose bilayer needs only 0.27 kJ/mol per glucose. These results indicate that water molecules decrease the attractive force between cellulose and facilitate the separation of cellulose molecules.

Because simulation capabilities are currently limited by computer, the velocity of spring movement in an SMD simulation is still unrealistically high. Previous studies have shown that, in SMD simulations, a faster velocity leads to a higher rupture force[267]. Therefore, there may be concerns associated with the accuracy of the force estimated from this simulation. Guzmán *et al.* studied the effect of SMD velocity on the rupture force for peptidomimetic-sheets and found that the force remained the same when the velocity was 100 Å/ns or lower[267]. The velocity in the current study's simulation (1 Å/ns) is two orders of magnitude slower than 100 Å/ns. This is believed to be slow enough that approximates the relatively realistic scenarios. Even so, it is important to stress that the scope of the current study is to gain qualitative, rather than quantitative, understandings of the process of separation in cellulose bilayers.

5.3.3 Adhesive Effect of Water

Although termed as a *constant velocity* SMD simulation, only a dummy spring moves upwards at a constant velocity. The top cellulose layer is attached to the spring.

Because of the binding of the two layers of cellulose bilayer, as well as the adhesive effect of water between them, the velocity of the top layer will be different from the velocity of spring which gives rise to the elastic energy of the spring. In other words, the volume of the elastic energy reveals the binding of the two layers of cellulose bilayer and the adhesive effect of water between the two layers. The elastic energy calculation is illustrated in Equation 5-3.

The elastic energy of different points in Figure 5-5 is listed in Table 5-2. At point *a*, the spring remains the initial length and the elastic energy (U) is 0. The slopes of point *a* to *b*, point *d* to *f*, and point *g* to *i* in Figure 5-5 (distance vs. time) provide the velocity of the top layer movement. Between point *a* and *b*, the velocity of the top layer (0.16 Å/ns) is lower than the velocity of the spring (1 Å/ns) because the binding between the two layers of cellulose bilayer induces the deformation of the spring. The elastic energy (U) reaches to 28.33 kJ/mole per glucose at point *b*. Between point *b* and *d*, the energy barrier of the attractive force between the two layers of cellulose bilayer is broken, leading to a swift movement of the top layer of about 10 Å/ns. At this stage, the spring partly recovers its deformation and the elastic energy (U) decreases to 0.42 kJ/mol per glucose at point *d*. Some initial diffusion of water molecules into the space between layers occurs at point *c* and the water molecules act as an adhesive. The adhesive effect slows down the velocity of the top layer and again causes the deformation of the spring. Between point *d* and *f*, the velocity of the top layer is about 0.545 Å/ns and the elastic energy of the spring increases to 3.08 kJ/mole per glucose at point *f*. With the same distance of two layers of cellulose bilayer *in vacuo*, the elastic energy of the spring is 0.63 kJ/mole per glucose. The increment of the elastic energy is 2.45 kJ/mole per glucose

(increased from 0.63 kJ/mole per glucose *in vacuo* to 3.08 kJ/mole per glucose in water) in water compared with that *in vacuo*, which is due to the adhesive effect of the water monolayer between two layers of cellulose bilayer. Between point *f* and *g*, both the water adhesive effect and the interaction between two layers of cellulose bilayer are weak, thus, the velocity of the top layer increases to about 2.49 Å/ns. Although the second water layer forms at point *h*, the adhesive effect of two water layers is too weak to slow the velocity of the top cellulose layer. The velocity of the top cellulose layer is almost the same as the velocity of the spring in stages VII, VIII, and XI (shown in Table 5-2).

Table 5-2. Descriptive information of the SMD simulation in water.

Point	Time (ns)	Height (Å)	U kJ/mol per glucose	Stage	k (Å/ns)	$E = \frac{1}{2}mv^2$ (kJ/mol per glucose)
a	0	7.65	0			
b	3.02	8.12	28.33	I/a-b	0.16	1.97×10^{-5}
c	3.16	9.55	6.90	II/b-c	10.21	0.08
d	3.24	10.58	0.42	III/c-d	11.88	0.11
e	3.56	10.75	0.92	IV/d-e	0.53	2.28×10^{-4}
f	4.42	11.23	3.08	V/e-f	0.56	2.54×10^{-4}
g	4.97	12.60	1.74×10^{-3}	VI/f-g	2.49	5.02×10^{-3}
h	5.31	12.93	3.92×10^{-3}	VII/g-h	0.97	7.62×10^{-4}
i	6.96	14.53	0.03	VIII/h-i	0.97	7.62×10^{-4}
j	8.35	15.97	3.92×10^{-3}	IX/j-k	1.01	8.1×10^{-4}
k	10.00	17.63				

5.3.4 Expanding Effect of Water

In vacuo, the disruption takes the same amount of time as in water. Also, the rupture forces are the same (~35,000 pN). Both observations suggest that water does not play a role at stage I. However, without water, the rupture occurs at a height of about 10.58 Å. After exceeding this height, the top layer moves almost at the speed of the spring. When the height of two layers reaches about 12.60 Å for the simulation in water, the top layer moves almost at the speed of the spring. The difference is caused by water molecules that diffused into the space between two layers of cellulose bilayer after the height reaches 9.55 Å (point *c*). Before enough water molecules diffused into cellulose layers and the first water monolayer, which acts as an adhesive, was completely formed, the water generates an opposite effect — *expanding effect* — which facilitates the separation of the two layers of cellulose bilayer. This is not surprising considering what occurs when water is injected between two stacked glass plates. This *expanding effect* of water significantly decreases the SMD force from around 20,000 pN *in vacuo* to 15,000 pN in water at 9.55 Å (point *c*). It is likely that this process again occurs with two layers of water. If the SMD force is small enough, the expanding effect of water can dominate and make the SMD force below 0 pN (around point *h*). Therefore, it is proposed that the effect of water alternates between expanding and adhesive cycles. However, as the magnitude of the effect dramatically decreases after every cycle, it is not observable beyond two water layers.

Another interesting pattern worth noticing is that before any water diffusion, the height of the two cellulose layers was 7.65 Å. The separation increased the height to 10.75 Å after the first layer of water diffusion was complete. Therefore, the first water

layer increased the height by 3.10 Å. With the second water layer, the height became 12.93 Å. Thus, the second water layer increased the separation by 2.18 Å. This difference may be confusing at first. However, after considering the hydrophobic nature of the cellulose surfaces, the difference could be accounted for reasonably. When the first layer of water is present, due to the hydrophobic nature of the cellulose surfaces, there is a space — so-called *hydrophobic space* — between the water layer and each of the cellulose layers. As such, the 3.10 Å increase in the cellulose layer separation is the thickness of the water monolayer plus twice the thickness of the hydrophobic space. When another water layer is added, it is reasonable to assume that the two water layers are in close contact. Therefore, the 2.18 Å increase in the cellulose layer separation reflects the net thickness of a water monolayer. This value is smaller than the 3 Å that has been widely believed[268]. It is likely that the highly ordered water molecules between two layers of cellulose bilayer contribute to the smaller thickness of the water monolayer in the current study. Moreover, the 2.18 Å is the net thickness of the water monolayer, not the sum of the thickness of the water monolayer and the thickness of the hydrophobic space.

5.4 Conclusion

Cellulose nanoparticles with the size of bilayers were prepared on a mica sheet. Cellulose bilayer particles filled with a monolayer, bilayers, and trilayers of water were found by means of AFM. Moreover, SMD simulations of bilayer of cellulose II in a water environment and *in vacuo* were carried out to investigate the interaction between water molecules and cellulose layers. In the water environment, at the stage I, when two layers of cellulose bilayer are pulled apart in the SMD simulation, the initial structure is

maintained because of the strong direct interaction between cellulose layers. The force built up in the spring eventually leads to a rupture of cellulose-cellulose structure. Before a monolayer of water is formed completely, water molecules diffuse into the space between two layers of cellulose bilayer and aid in the expansion of two cellulose layers. Once a monolayer of water is completely formed, the monolayer of water generates an adhesive effect which stabilizes the two layers of cellulose bilayer. This process is repeated when the second layer of water diffuses into the space between cellulose layers. The direct interaction between two layers of cellulose bilayer is negligible at this point. Both expanding and adhesive effects of water layers disappear when the two layers of cellulose bilayer are further separated by more than two layers of water. The SMD simulation results indicate that water molecules can effectively decrease the internal energy between two layers of cellulose bilayer. The energy to separate two layers of water-hydrated cellulose bilayer is 6.92 kJ/mol per glucose for a stable bilayer cellulose filled with a monolayer of water, and 0.27 kJ/mol per glucose for a stable bilayer cellulose filled with a bilayer of water. Same simulation *in vacuo* shows that the energy to separate two layers of cellulose bilayer likely requires 46.08 kJ/mol per glucose *in vacuo*. Cellulose decrystallization is a free-energetically unfavorable process. Its thermodynamic barrier needs to be overcome for the removal of a cellulose chain from the crystal. Results from the current study suggest that the decrystallization could be considered as a process that separates cellulose layers and allows water molecules to diffuse in between the layers. Consequently, water filled cellulose is readily peeled off by cellulase. Thus, water molecules play an important role for cellulase in overcoming the thermodynamic barrier during enzymatic hydrolysis.

Chapter 6: A Mammalian Cell-based Nanomechanical Biosensor

6.1 Introduction

A biosensor is an analytic device that combines biological sensing elements, such as antibodies, nucleic acids, enzymes, and cells, with a physicochemical detector to detect analytes rapidly[269]. In recent years, a new trend has emerged that utilizes living cells as the sensing element in the biosensors, and these biosensors have been widely used in the field of environment, medine, toxicology, and defense[270,271]. Like other biosensors, cell-based biosensors have not only high selectivity and sensitivity, but also a rapid response to biological analytes. The advantage of cell-based biosensors is that they can uncover physiological and mechanistic information because they use living cells. Therefore, cell-based biosensors can provide further understanding towards the functional basis of the activities of analytes in protein synthesis, signaling transduction, cell apoptosis, migration, and metabolism.

Another fundamental component of biosensors is a transducer, which measures the interaction between an analyte and the sensing element and turns it into an electric signal. The efficiency of the transducer determines the sensitivity, stability, and reproducibility of the signal. Over the years, many types of transducers have been developed: optical[272], electrochemical[273], thermal[274], gravimetric/acoustic[275], and mechanical transducers[140].

Cantilevers[87,276,277] are highly sensitive mechanical transducers. They originated from atomic force microscopy probes and are usually made of silicon or silicon nitride in a variety of shapes. Their small size makes possible a faster response and the ability to explore microenvironments. When combined with a biosensing element, the

microcantilever can be used as a biosensor. For such application, the microcantilever responds to changes in the biosensing element and this response is converted into a measurable signal. The response could be the bending of the microcantilever or the change in oscillating frequency of the microcantilever.

Figure 6-1 is a schematic illustration that demonstrates the measurability of the bending of a cell-based microcantilever sensor. The biosensing element (cells) adhered to the surface of the microcantilever responds to the presence of an analyte. The analyte will cause a change in the mechanical properties of the cells, and the changes in the cells will bend the microcantilever. The deflection of the microcantilever can be monitored with a laser beam reflected from the tip of the microcantilever. The change in surface stress, $\Delta\sigma$, can be related to the deflection of the microcantilever through the Stoney equation.

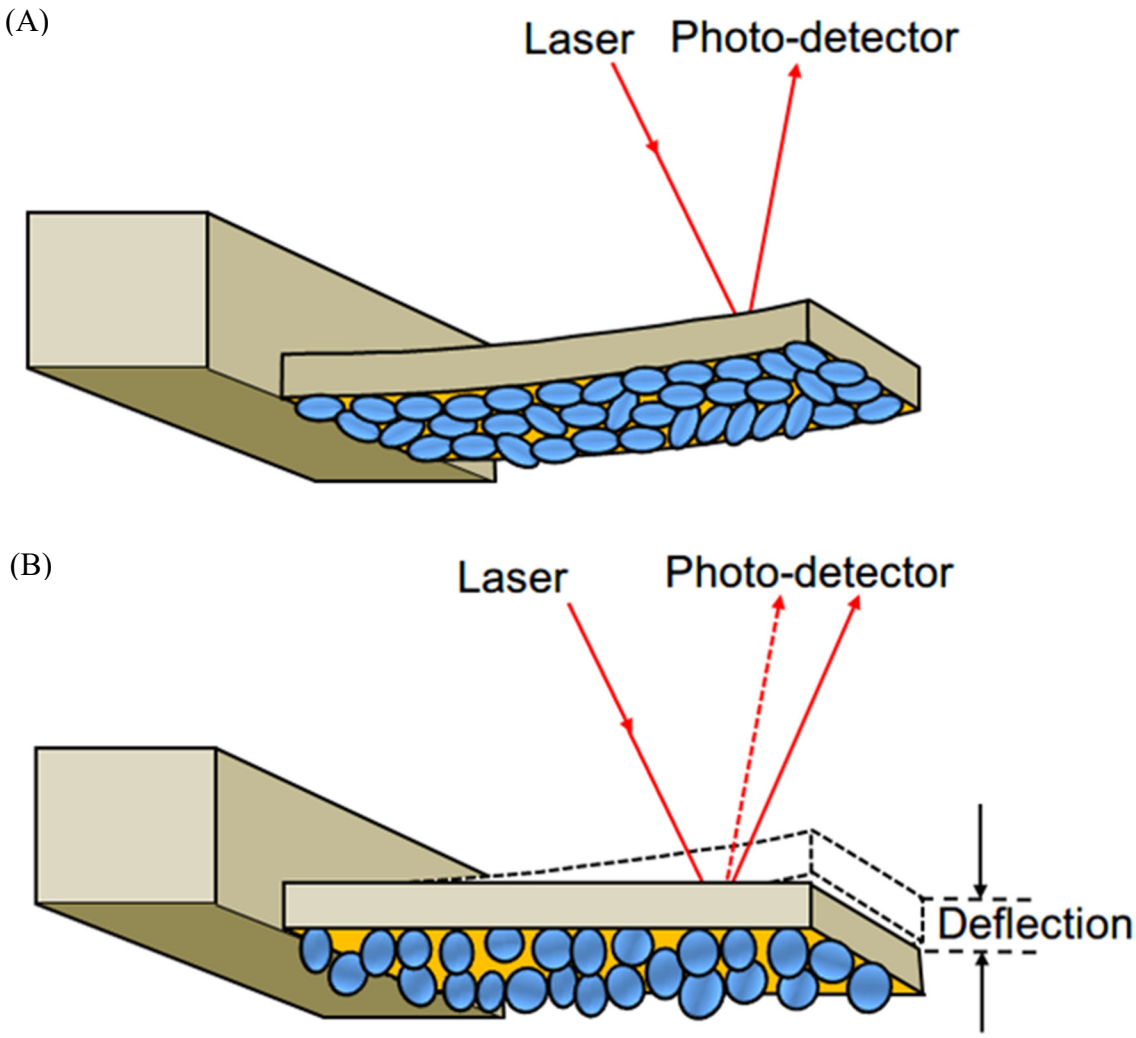

Figure 6-1. Schematic illustration of cell-based microcantilever sensing.
(A) The cells exhibit a flat morphology before exposure to an analyte. (B) The cells exhibit a more rounded morphology after exposure to an analyte. The deflection of the microcantilever upon the morphological change of the cells is indicated in (B).

Although there is an increasing number of papers reporting microcantilever biosensors[160,278–281], the development of cell-based microcantilever biosensors is still very limited. Antonik first proposed to use microcantilever sensors to detect the nanomechanical responses of living Madin–Darby canine kidney (MDCK) cells cultured on one side the microcantilevers[282]. The responses of cells to melittin and sodium azide

were observed by monitoring the deflection of microcantilever within several seconds of injection. Park *et al.* later cultured mice heart muscle cells on microcantilevers, and they found that the grooved surfaces of microcantilevers can produce more bending than flat surfaces of microcantilevers under the small contraction forces generated by mice heart muscle cells[283,284]. Xi *et al.* grew muscle cells on micromechanical structures to create cell-powered mechanical motors[285]. Das *et al.* integrated skeletal muscle with a silicon microcantilever array to develop a serum-free cell-based sensor[286,287]. This integration could allow high-throughput and real-time measurement of physiological properties of the myotubes and could become a micro-biomechanical platform for studying other complex biological phenomennons[288].

In the present research, we developed a protocol for preparing microcantilever biosensors by culturing human epidermoid carcinoma A431 cells on one side of the microcantilever. Using cell-adhered microcantilevers, we have observed distinct, real-time responses of adherent cells to α-cyclodextrin and methyl-β-cyclodextrin. With this work, we have revealed the possibility of cell-based microcantilevers in sensing the change of cells induced by an analyte and have provided some direct evidence to explain the biological cause of the microcantilever deflection.

6.2 Material and Methods

6.2.1 Reagents and Material

The human epidermoid carcinoma A431 cell line was obtained from American Type Tissue Collection (Manassas, VA). Microcantilevers (CSC38/Cr-Au, force constant 0.03 N/m, length / width / thickness = 350 μm / 35 μm / 1.0 μm) were purchased from MikroMasch (Wilsonville, OR). α-Cyclodextrin (αCD) and methyl-β-cyclodextrin

(MβCD) were obtained from Sigma-Aldrich (St. Louis, MO) (Figure 6-2). Antibiotics, Dulbecco's modified Eagle's medium (DMEM), HEPES buffer (4-(2-hydroxyethyl)-1-piperazineethanesulfonic acid), trypsin–EDTA, fetal bovine serum (FBS), and Hank's balanced salt solution (HBSS) buffer were purchased from Invitrogen (Carlsbad, CA).

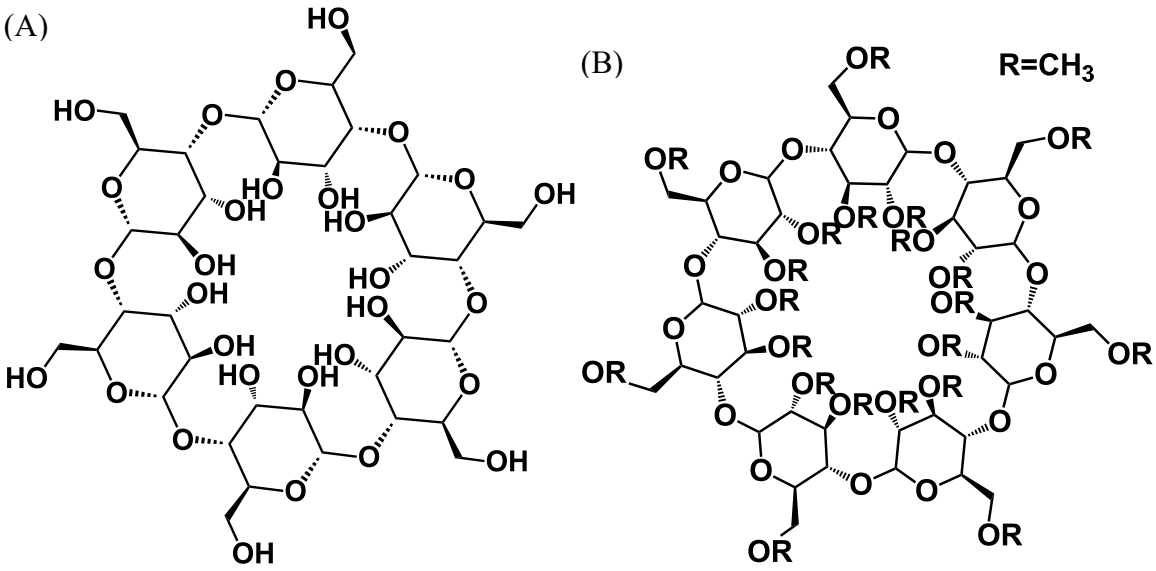

Figure 6-2. Molecule structure of (A) αCD and (B) methyl-β-CD.

6.2.2 Cell Culture

A431 cells were cultured under a humidified atmosphere at 37°C and 5% CO_2 in DMEM containing 100-IU/mL penicillin, 10% FBS, and 100-µg/mL streptomycin in T75 Corning culture flasks. The A431 cells were harvested at 95% confluency as usual. The microcantilevers were washed with DI-water and 200 proof ethanol, followed by exposure to ProCleaner™ UV-ozone for 20 minutes. They were then placed in a 12-well tissue culture plate along with A431 cells (1.60×10^6 cells/mL) in the buffer. The cells

adhere and grow on the gold-surfaced side of the microcantilevers under the same condition as cell culture. Once 80-90% coverage of cells were reached, the adherent cells on the microcantilevers were rinsed with phosphate-buffered saline and then were starved in serum-free medium for 18 hrs before assay.

6.2.3 Cantilever Assays

Before the assay on the same day, the cells on the microcantilever were rinsed carefully with assay buffer (20-mM HEPES in HBSS, pH 7.2). The microcantilever was then placed in a flow-through liquid cell with a volume of 0.30 mL. The microcantilever assay was then executed as described previously[289]. In brief, the assay buffer was injected into the flow cell at 1 mL/h with a syringe pump, so that the baseline fluctuations could be minimized. After the baseline had become stabile, the assay buffer with analyte dissolved in it was injected through the 0.50-mL sample loop into the liquid cell. The bending of the microcantilever was monitored by measuring the position of a laser beam reflected from the microcantilever tip to a photodiode (Figure 6-1). Each assay was repeated several times to ensure its reproducibility and reliability.

6.3 Results and Discussion

In this present study, we sought to test the possibility of cell-based microcantilevers as biosensors. First, we prepared a cell-adhered microcantilever by culturing human epidermoid carcinoma A431 cells onto its front side (non-reflective side) only (Figure 6-3). As strong adherent cells, A431 cells formed a nice monolayer, which is ideal for cell-based assay. Considering that the microcantilever deflection is caused by the imbalance in surface stress between the front and back sides of the microcantilever, it is critical to culture the cells on only one side of the microcantilever.

This was achieved by blocking the backside of the microcantilever (reflective side); the microcantilever was placed backside down during the cell-seeding. Another important contributing factor to sensitivity is the surface coverage of the microcantilever by the cells. Satisfactory results were obtained when a high density (1.60×10^6 cells/mL) of the cells was seeded.

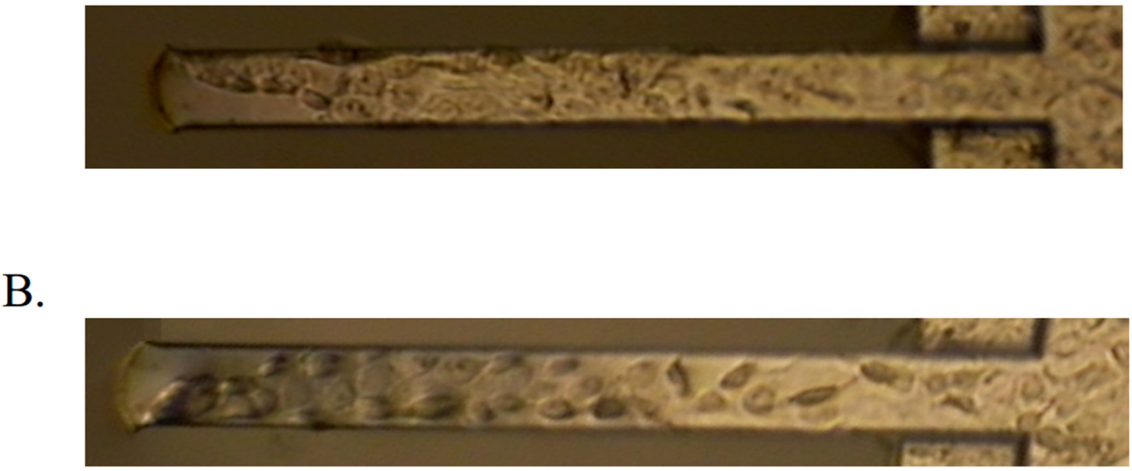

Figure 6-3. Microscope images of the cells cultured on a microcantilever before and after exposure to 8.0-mM MβCD.
The cells exhibit a flat morphology before exposure (A) and a more rounded morphology after exposure (B).

Next, we examined the sensing ability of cell-adhered microcantilevers. The study was focused on the detection of methyl-β-cyclodextrin (MβCD) and α-cyclodextrin (αCD) (see Figure 6-2A and Figure 6-2B). Both of them belong to cyclodextrins, a family of cyclic oligosaccharides composed of α-1, 4-linked glucopyranose subunits. The difference between these two compounds is that αCD has six glucopyranose subunits

whereas MβCD has seven, which results in different sizes of the hydrophobic cavities in these molecules[290]. First, the cell-adhered microcantilever was placed in the liquid cell and allowed to equilibrate at room temperature with a constant flow of the assay buffer at 1.0 mL/h. Once a stable baseline was obtained, an analyte was injected into the flow cell at the 25th min. For MβCD, the earliest bending response occurred at 40 min and remained the 0.27-nm/min deflection rate for 22 min. The deflection rate is defined as the change in the level of the microcantilever bending over time. The results of this study are summarized in Figure 6-4. At 62 min, the responses switched to a more drastic change in deflection (0.54 nm/min). This sudden switch could be an indication of the occurrence of a second cellular response at a higher concentration of MβCD. This switch was also observed for αCD. However, the overall deflection of αCD, which was barely above the baseline response established by the assay buffer (i.e., blank), was much smaller compared with that of MβCD. A more quantitative comparison shows that the rate of deflection for αCD is approximately 0.025 nm/min, which is about 20-fold lower than that for MβCD.

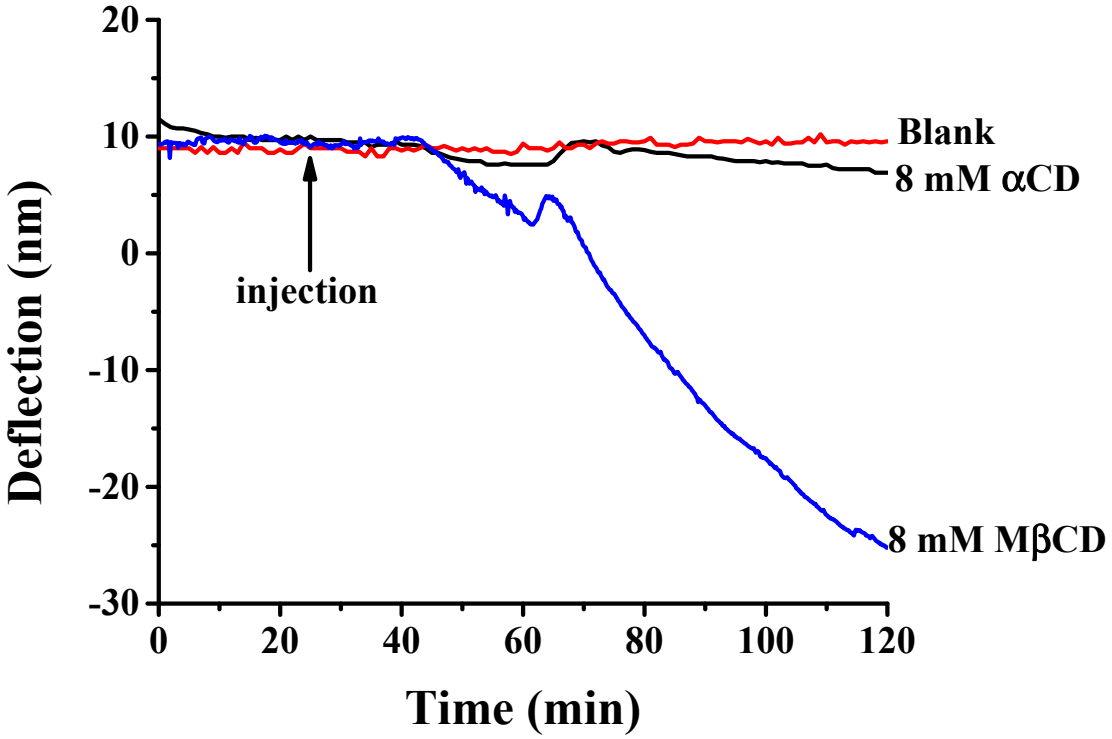

Figure 6-4. The results of the cell-based microcantilever assay.
The different profiles of the microcantilever bending caused by 8-mM αCD and 8-mM MβCD are shown, respectively. The baseline response was established with the blank.

We attribute the substantial bending of the microcantilever shown in Figure 6-4 to the MβCD-induced cell response. MβCD is known for the ability to extract cholesterol from the cell surface by forming inclusion complexes. One important function of cholesterol is to maintain the integrity and fluidity of cell membrane and secure important protein in the membrane. By disrupting the structure of cholesterol-rich microdomains, MβCD was able to change the cell morphology to a more rounded shape, which is evidenced in Figure 6-3. Consequently, the interaction between individual cells and the surface of the microcantilever was significantly altered, which conceivably led to the

significant change of the overall surface stress of the microcantilever and the subsequent substantial bending of the microcantilever. Apparently, the cell-adhered microcantilever was able to convert the MβCD-induced cellular response to a measurable mechanical response (bending).

Although both αCD and MβCD are cyclic oligosaccharides, αCD does not extract cholesterol from cells as efficiently as MβCD does[290,291], because αCD has a smaller hydrophobic cavity compared to that of MβCD. In fact, αCD is often used as a negative control for MβCD in studies involving cholesterol extraction[291]. αCD is incapable of producing a measurable change in cell morphology, which probably explains the 20-fold lower deflection rate compared with that of MβCD.

Overall, the present study has demonstrated for the first time the feasibility of cell-based microcantilever sensing, which capitalizes on the unique capability of the microcantilever to convert cellular response to a measurable mechanical response. Compared with other sensing technologies, cell-based microcantilever sensing is a label-free, noninvasive technology that can perform real-time monitoring based on induced cellular response. Also, it has high sensitivity and excellent specificity with a low production cost, low-power consumption, and a small size[138]. Cell-based microcantilever sensing has the potential to become a cost-effective and highly sensitive sensing platform for environmental, medical, toxicological, and defense applications.

Chapter 7: Summary

Chapter 1 provided the background on the energy crisis, which is a major concern for humanity. To avoid serious social and economic pitfalls, it is critical to find affordable, alternative, and renewable energy sources, as well as to reduce the world's dependence on petroleum. Cellulosic biofuel (bioethanol) is one of the most promising substitute energy sources. However, before bioethanol becomes a conventional form of energy as petroleum fuel is currently, some challenges have to be overcome. One of these challenges is the low efficiency of the enzymatic digestion of cellulose. The mechanism of cellulose-cellulase interactions is still not fully understood. One reason for this is because the interactions between cellulase and the cellulose substrate occurs on the liquid–solid interface and few techniques are sensitive enough to study it.

Chapter 2 provided background on nanomechanical sensors, including microcantilevers and QCM-D. These sensors have drawn increased attention due to the development of silicon micromachining techniques for integrated circuits (IC). Techniques using these sensors are sensitive enough to monitor surface-property changes of cellulose substrates. With these techniques, the study of the interfacial interactions between cellulase and cellulose became possible. Chapter 3 reported the use of a nanomechanical sensor (cantilever) to probe the interaction between cellulase and cellulose and described the discovery of experimental evidence for decrystallization. It was also shown that decrystallization plays a critical role during the degradation of cellulose aggregation. Chapter 4 reported the examination cellulase–cellulose interactions from a unique perspective—changes in topography during enzymatic hydrolysis. The topography was found to be a useful tool for studying enzymatic hydrolysis. Further

experimental proof of decrystallization was described. Chapter 5 described the computations and experiments designed to evaluate the interaction between water molecules and cellulose. Chapter 6 reported the use of a microcantilever sensor to explore the response of mammalian cells to chemicals.

The chapters as a whole examine topics related to the enzymatic hydrolysis of cellulose by cellulase, the possibility of utilizing nanomechanical sensing techniques to study interactions between cellulase and cellulose substrates, and provide valuable insight into understanding the mechanisms of enzymatic hydrolysis of cellulosic biomass.

Scientists are aware of the importance of the decrystallization, but few actual studies have been carried out due to a shortage of research methods for the decrystallization. In this dissertation, a nanomechanical sensor was developed that can monitor in real time the overall hydrolysis of cellulose by cellulase. With this nanomechanical sensor, the first experimental evidence of decrystallization was obtained. Topography was also successfully employed to explore the enzymatic activity of cellulase, and the approach is straightforward, easy to implement, and informative. These techniques provide researchers in related fields with useful tools to study enzymatic activities at liquid–solid interfaces.

Continued research should attempt to apply the methods developed in the research described in this dissertation to study the interactions between cellulose and different cellulase enzymes. More information about cellulose hydrolysis by cellulase, such as synergistic effects and the influence of pretreatment on biomass, can be thus obtained. In the future, genetically modified cellulase will be characterized by means of these novel

sensing techniques, such that the hydrolysis process can be optimized and the efficiency of biomass conversion improved.

List of References

1. *International Energy Outlook 2016 (IEO2016)*. Washington, DC: U.S. Energy Information Administration (EIA); 2016. http://www.eia.gov/forecasts/ieo/index.cfm. Accessed June 16, 2016.

2. Miller RG, Sorrell SR. The future of oil supply. *Philosophical Transactions of the Royal Society of London A: Mathematical, Physical and Engineering Sciences*. 2014;372(2006):20130179. doi:10.1098/rsta.2013.0179.

3. Hirsch RL, Bezdek R, Wendling R. Peaking of World Oil Production and Its Mitigation. *Driving Climate Change: Cutting Carbon from Transportation*. 2010:9.

4. FAO. The State of Food Insecurity in the World 2015. Food and Agriculture Organization of the United Nations. http://www.fao.org/hunger/en/. Published 2015. Accessed June 17, 2016.

5. Shimelmitz R, Kuhn SL, Jelinek AJ, Ronen A, Clark AE, Weinstein-Evron M. "Fire at will": The emergence of habitual fire use 350,000 years ago. *Journal of Human Evolution*. 2014;77:196-203. doi:10.1016/j.jhevol.2014.07.005.

6. EUBIA. European Biomass Industry Association - Bioethanol. http://www.eubia.org/index.php/about-biomass/biofuels-for-transport/bioethanol. Accessed November 28, 2016.

7. Biofuels: Ethanol and Biodiesel - Energy Explained, Your Guide To Understanding Energy - Energy Information Administration. http://www.eia.gov/energyexplained/?page=biofuel_home. Accessed November 28, 2016.

8. Energy Information Administration (EIA). Biofuels Issues and Trends. https://www.eia.gov/biofuels/issuestrends/. Published 2012. Accessed June 21, 2016.

9. Theis K. At $2.15 a Gallon, Cellulosic Ethanol Could Be Cost Competitive. *Continuum Magazine*. 2013;5:5-7.

10. Chen H. *Biotechnology of Lignocellulose*. Dordrecht: Springer Netherlands; 2014. http://link.springer.com/10.1007/978-94-007-6898-7. Accessed August 4, 2016.

11. Sticklen MB. Plant genetic engineering for biofuel production: towards affordable cellulosic ethanol. *Nat Rev Genet*. 2008;9(6):433-443. doi:10.1038/nrg2336.

12. Xi J, Du W, Zhong and L. *Probing the Interaction Between Cellulose and Cellulase with a Nanomechanical Sensor*. InTech; 2013. http://www.intechopen.com/books/cellulose-medical-pharmaceutical-and-electronic-applications/probing-the-interaction-between-cellulose-and-cellulase-with-a-nanomechanical-sensor. Accessed November 7, 2016.

13. Yang H, Yan R, Chen H, Lee DH, Zheng C. Characteristics of hemicellulose, cellulose and lignin pyrolysis. *Fuel*. 2007;86(12–13):1781-1788. doi:10.1016/j.fuel.2006.12.013.

14. Li Q, Renneckar S. Supramolecular Structure Characterization of Molecularly Thin Cellulose I Nanoparticles. *Biomacromolecules*. 2011;12(3):650-659. doi:10.1021/bm101315y.

15. Brown RM, Saxena IM, eds. *Cellulose: Molecular and Structural Biology*. Dordrecht: Springer Netherlands; 2007. http://link.springer.com/10.1007/978-1-4020-5380-1. Accessed June 21, 2016.

16. Postek MT, Vladár A, Dagata J, et al. Development of the metrology and imaging of cellulose nanocrystals. *Measurement Science and Technology*. 2010;22(2):24005.

17. Moon RJ. Nanomaterials in the forest products industry. In: *McGraw-Hill Yearbook of Science and Technology*. New York, NY, US: McGraw-Hill; 2008:225-228. http://www.treesearch.fs.fed.us/pubs/32715. Accessed November 26, 2016.

18. Habibi Y, Lucia LA, Rojas OJ. Cellulose Nanocrystals: Chemistry, Self-Assembly, and Applications. *Chem Rev*. 2010;110(6):3479-3500. doi:10.1021/cr900339w.

19. Pérez S, Samain D. Structure and Engineering of Celluloses. In: Horton D, ed. *Advances in Carbohydrate Chemistry and Biochemistry*. Vol 64. Academic Press; 2010:25-116. http://www.sciencedirect.com/science/article/pii/S0065231810640036. Accessed June 21, 2016.

20. Hayashi N, Sugiyama J, Okano T, Ishihara M. Selective degradation of the cellulose Iα component in Cladophora cellulose with Trichoderma viride cellulase. *Carbohydrate Research*. 1997;305(1):109-116. doi:10.1016/S0008-6215(97)00281-4.

21. Nishiyama Y, Langan P, Chanzy H. Crystal Structure and Hydrogen-Bonding System in Cellulose Iβ from Synchrotron X-ray and Neutron Fiber Diffraction. *J Am Chem Soc*. 2002;124(31):9074-9082. doi:10.1021/ja0257319.

22. Nishiyama Y, Sugiyama J, Chanzy H, Langan P. Crystal Structure and Hydrogen Bonding System in Cellulose Iα from Synchrotron X-ray and Neutron Fiber Diffraction. *J Am Chem Soc*. 2003;125(47):14300-14306. doi:10.1021/ja037055w.

23. O'Sullivan A. Cellulose: the structure slowly unravels. *Cellulose*. 1997;4(3):173-207. doi:10.1023/a:1018431705579.

24. Zugenmaier P. Conformation and packing of various crystalline cellulose fibers. *Progress in Polymer Science*. 2001;26(9):1341-1417. doi:10.1016/S0079-6700(01)00019-3.

25. Chundawat SPS, Bellesia G, Uppugundla N, et al. Restructuring the Crystalline Cellulose Hydrogen Bond Network Enhances Its Depolymerization Rate. *J Am Chem Soc*. 2011;133(29):11163-11174. doi:10.1021/ja2011115.

26. Zhang Y-HP, Cui J, Lynd LR, Kuang LR. A Transition from Cellulose Swelling to Cellulose Dissolution by o-Phosphoric Acid: Evidence from Enzymatic Hydrolysis and Supramolecular Structure. *Biomacromolecules*. 2006;7(2):644-648. doi:10.1021/bm050799c.

27. Igarashi K, Wada M, Samejima M. Activation of crystalline cellulose to cellulose III_I results in efficient hydrolysis by cellobiohydrolase. *FEBS Journal*. 2007;274(7):1785-1792. doi:10.1111/j.1742-4658.2007.05727.x.

28. Kobayashi K, Kimura S, Kim U-J, Tokuyasu K, Wada M. Enzymatic hydrolysis of cellulose hydrates. *Cellulose*. 2012;19(3):967-974. doi:10.1007/s10570-012-9696-2.

29. Kolpak FJ, Blackwell J. Determination of the Structure of Cellulose II. *Macromolecules*. 1976;9(2):273-278. doi:10.1021/ma60050a019.

30. Stipanovic AJ, Sarko A. Packing Analysis of Carbohydrates and Polysaccharides. 6. Molecular and Crystal Structure of Regenerated Cellulose II. *Macromolecules*. 1976;9(5):851-857. doi:10.1021/ma60053a027.

31. Langan P, Nishiyama Y, Chanzy H. X-ray Structure of Mercerized Cellulose II at 1 Å Resolution. *Biomacromolecules*. 2001;2(2):410-416. doi:10.1021/bm005612q.

32. Gessler K, Krauss N, Steiner T, Betzel C, Sandmann C, Saenger W. Crystal structure of beta-D-cellotetraose hemihydrate with implications for the structure of cellulose II. *Science*. 1994;266(5187):1027-1029. doi:10.1126/science.7973653.

33. Langan P, Nishiyama Y, Chanzy H. A Revised Structure and Hydrogen-Bonding System in Cellulose II from a Neutron Fiber Diffraction Analysis. *J Am Chem Soc*. 1999;121(43):9940-9946. doi:10.1021/ja9916254.

34. Šturcová A, His I, Wess TJ, Cameron G, Jarvis MC. Polarized Vibrational Spectroscopy of Fiber Polymers: Hydrogen Bonding in Cellulose II. *Biomacromolecules*. 2003;4(6):1589-1595. doi:10.1021/bm034295v.

35. Chang VS, Holtzapple MT. Fundamental Factors Affecting Biomass Enzymatic Reactivity. In: Finkelstein M, Davison BH, eds. *Twenty-First Symposium on Biotechnology for Fuels and Chemicals*. Applied Biochemistry and Biotechnology. Humana Press; 2000:5-37. http://link.springer.com/chapter/10.1007/978-1-4612-1392-5_1. Accessed November 21, 2016.

36. Berlin A, Balakshin M, Gilkes N, et al. Inhibition of cellulase, xylanase and β-glucosidase activities by softwood lignin preparations. *Journal of Biotechnology*. 2006;125(2):198–209.

37. Eriksson T, Börjesson J, Tjerneld F. Mechanism of surfactant effect in enzymatic hydrolysis of lignocellulose. *Enzyme and Microbial Technology*. 2002;31(3):353–364.

38. Lavenson DM, Tozzi EJ, McCarthy MJ, Powell RL, Jeoh T. Investigating adsorption of bovine serum albumin on cellulosic substrates using magnetic resonance imaging. *Cellulose*. 2011;18(6):1543-1554. doi:10.1007/s10570-011-9588-x.

39. Wang H, Kobayashi S, Hiraide H, Cui Z, Mochidzuki K. The Effect of Nonenzymatic Protein on Lignocellulose Enzymatic Hydrolysis and Simultaneous Saccharification and Fermentation. *Appl Biochem Biotechnol*. 2014;175(1):287-299. doi:10.1007/s12010-014-1242-2.

40. Yang B, Wyman CE. BSA treatment to enhance enzymatic hydrolysis of cellulose in lignin containing substrates. *Biotechnol Bioeng*. 2006;94(4):611-617. doi:10.1002/bit.20750.

41. Lynd LR, Weimer PJ, van Zyl WH, Pretorius IS. Microbial Cellulose Utilization: Fundamentals and Biotechnology. *Microbiology and Molecular Biology Reviews*. 2002;66(3):506-577. doi:10.1128/mmbr.66.3.506-577.2002.

42. Mosier N, Hall P, Ladisch C, Ladisch M. Reaction Kinetics, Molecular Action, and Mechanisms of Cellulolytic Proteins Recent Progress in Bioconversion of Lignocellulosics. In: Tsao G, Brainard A, Bungay H, et al., eds. Vol 65. Advances in Biochemical Engineering/Biotechnology. Springer Berlin / Heidelberg; 1999:23-40. http://dx.doi.org/10.1007/3-540-49194-5_2.

43. Payne CM, Knott BC, Mayes HB, et al. Fungal Cellulases. *Chem Rev*. 2015;115(3):1308-1448. doi:10.1021/cr500351c.

44. Bayer EA, Chanzy H, Lamed R, Shoham Y. Cellulose, cellulases and cellulosomes. *Current Opinion in Structural Biology*. 1998;8(5):548-557. doi:10.1016/S0959-440X(98)80143-7.

45. Bornscheuer U, Buchholz K, Seibel J. Enzymatic Degradation of (Ligno)cellulose. *Angew Chem Int Ed*. 2014;53(41):10876-10893. doi:10.1002/anie.201309953.

46. Esterbauer H, Hayn M, Abuja PM, Claeyssens M. Structure of Cellulolytic Enzymes. In: *Enzymes in Biomass Conversion*. Vol 460. ACS Symposium Series. American Chemical Society; 1991:301-312. http://dx.doi.org/10.1021/bk-1991-0460.ch023. Accessed April 29, 2016.

47. Juturu V, Wu JC. Microbial cellulases: Engineering, production and applications. *Renewable and Sustainable Energy Reviews*. 2014;33:188-203. doi:10.1016/j.rser.2014.01.077.

48. Wilson DB. Cellulases and biofuels. *Current Opinion in Biotechnology*. 2009;20(3):295-299. doi:10.1016/j.copbio.2009.05.007.

49. Chundawat SPS, Beckham GT, Himmel ME, Dale BE. Deconstruction of Lignocellulosic Biomass to Fuels and Chemicals. *Annual Review of Chemical and Biomolecular Engineering*. 2011;2(1):121-145. doi:10.1146/annurev-chembioeng-061010-114205.

50. Hasunuma T, Okazaki F, Okai N, Hara KY, Ishii J, Kondo A. A review of enzymes and microbes for lignocellulosic biorefinery and the possibility of their application to consolidated bioprocessing technology. *Bioresource Technology*. 2013;135:513-522. doi:10.1016/j.biortech.2012.10.047.

51. Sun Y, Cheng J. Hydrolysis of lignocellulosic materials for ethanol production: a review. *Bioresource Technology*. 2002;83(1):1-11. doi:10.1016/S0960-8524(01)00212-7.

52. Zhang Y-HP, Lynd LR. Toward an aggregated understanding of enzymatic hydrolysis of cellulose: Noncomplexed cellulase systems. *Biotechnol Bioeng*. 2004;88(7):797-824. doi:10.1002/bit.20282.

53. Dwivedi P, Alavalapati JRR, Lal P. Cellulosic ethanol production in the United States: Conversion technologies, current production status, economics, and emerging developments. *Energy for Sustainable Development*. 2009;13(3):174-182. doi:10.1016/j.esd.2009.06.003.

54. Martin S. Protein engineering of cellulases. *Biochimica et Biophysica Acta (BBA) - Protein Structure and Molecular Enzymology*. 2000;1543(2):239-252. doi:10.1016/s0167-4838(00)00247-8.

55. Guillén D, Sánchez S, Rodríguez-Sanoja R. Carbohydrate-binding domains: multiplicity of biological roles. *Applied Microbiology and Biotechnology*. 2010;85(5):1241-1249. doi:10.1007/s00253-009-2331-y.

56. Lehtio J, Sugiyama J, Gustavsson M, Fransson L, Linder M, Teeri TT. The binding specificity and affinity determinants of family 1 and family 3 cellulose binding modules. *Proc Natl Acad Sci U S A*. 2003;100(2):484-489. doi:10.1073/pnas.212651999.

57. Zhong L, Matthews J, Crowley M, et al. Interactions of the complete cellobiohydrolase I from Trichodera reesei with microcrystalline cellulose Iβ. *Cellulose*. 2008;15(2):261-273. doi:10.1007/s10570-007-9186-0.

58. Himmel ME, Ding S-Y, Johnson DK, et al. Biomass Recalcitrance: Engineering Plants and Enzymes for Biofuels Production. *Science*. 2007;315(5813):804-807. doi:10.1126/science.1137016.

59. Himmel ME, Vinzan T, Bower S, Jechura J. *BSCL Use Plan: Solving Biomass Recalcitrance*. Place of publication not identified: BiblioGov; 2012.

60. Himmel ME, Picataggio SK. Our Challenge is to Acquire Deeper Understanding of Biomass Recalcitrance and Conversion. In: Scientist MEHP, ed. *Biomass Recalcitrance*. Blackwell Publishing Ltd.; 2008:1-6. http://onlinelibrary.wiley.com/doi/10.1002/9781444305418.ch1/summary. Accessed November 26, 2016.

61. Cosgrove DJ. Growth of the plant cell wall. *Nature Reviews Molecular Cell Biology*. 2005;6(11):850-861. doi:10.1038/nrm1746.

62. Zhao X, Zhang L, Liu D. Biomass recalcitrance. Part I: the chemical compositions and physical structures affecting the enzymatic hydrolysis of lignocellulose. *Biofuels, Bioprod Bioref*. 2012;6(4):465-482. doi:10.1002/bbb.1331.

63. Iiyama K, Lam T, Stone BA. Covalent Cross-Links in the Cell Wall. *Plant Physiol*. 1994;104(2):315-320.

64. Himmel ME, Ruth MF, Wyman CE. Cellulase for commodity products from cellulosic biomass. *Current Opinion in Biotechnology*. 1999;10(4):358-364. doi:10.1016/S0958-1669(99)80065-2.

65. Wyman CE, Dale BE, Elander RT, Holtzapple M, Ladisch MR, Lee YY. Coordinated development of leading biomass pretreatment technologies. *Bioresource Technology*. 2005;96(18):1959-1966. doi:10.1016/j.biortech.2005.01.010.

66. Akin DE. Plant cell wall aromatics: influence on degradation of biomass. *Biofuels, Bioprod Bioref*. 2008;2(4):288-303. doi:10.1002/bbb.76.

67. The Nobel Prize in Physics 1986. https://www.nobelprize.org/nobel_prizes/physics/laureates/1986/. Accessed November 28, 2016.

68. Bennig GK. Atomic force microscope and method for imaging surfaces with atomic resolution. *US patent 4724318 A*. February 1988. http://www.google.com/patents/US4724318. Accessed October 29, 2016.

69. Binnig G, Gerber C, Stoll E, Albrecht TR, Quate CF. Atomic Resolution with Atomic Force Microscope. *EPL*. 1987;3(12):1281. doi:10.1209/0295-5075/3/12/006.

70. Binnig G, Quate CF, Gerber C. Atomic Force Microscope. *Phys Rev Lett*. 1986;56(9):930-933. doi:10.1103/PhysRevLett.56.930.

71. Bhushan B, Marti O. Scanning Probe Microscopy — Principle of Operation, Instrumentation, and Probes. In: Bhushan PB, ed. *Nanotribology and Nanomechanics*. Springer Berlin Heidelberg; 2005:41-115. http://link.springer.com/chapter/10.1007/3-540-28248-3_2. Accessed November 28, 2016.

72. Vahabi S, Nazemi Salman B, Javanmard A. Atomic force microscopy application in biological research: a review study. *Iran J Med Sci*. 2013;38(2):76-83.

73. nanoScience Instruments, inc. Atomic Force Microscopy overview. http://www.teachnano.com/education/AFM.html. Accessed November 28, 2016.

74. Maver U, Velnar T, Gaberšček M, Planinšek O, Finšgar M. Recent progressive use of atomic force microscopy in biomedical applications. *TrAC Trends in Analytical Chemistry*. 2016;80:96-111. doi:10.1016/j.trac.2016.03.014.

75. Bhushan B. *Springer Handbook of Nanotechnology*. 3rd ed. 2010 edition. New York, NY, US: Springer; 2010.

76. Wilfinger RJ, Bardell PH, Chhabra DS. The Resonistor: A Frequency Selective Device Utilizing the Mechanical Resonance of a Silicon Substrate. *IBM J Res Dev*. 1968;12(1):113–118. doi:10.1147/rd.121.0113.

77. Heng TMS. Trimming of Microstrip Circuits Utilizing Microcantilever Air Gaps (Correspondence). *IEEE Transactions on Microwave Theory and Techniques*. 1971;19(7):652-654. doi:10.1109/TMTT.1971.1127595.

78. Petersen KE. Micromechanical membrane switches on silicon. *IBM Journal of Research and Development*. 1979;23(4):376–385.

79. Berger R, Delamarche E, Lang HP, et al. Surface stress in the self-assembly of alkanethiols on gold probed .by a force microscopy technique. *Appl Phys A*. 66(1):S55-S59. doi:10.1007/s003390051099.

80. Datskos PG, Sauers I. Detection of 2-mercaptoethanol using gold-coated micromachined cantilevers. *Sensors and Actuators B: Chemical*. 1999;61(1–3):75-82. doi:10.1016/S0925-4005(99)00251-8.

81. Bai X, Hou H, Zhang B, Tang J. Label-free detection of kanamycin using aptamer-based cantilever array sensor. *Biosensors and Bioelectronics*. 2014;56:112-116. doi:10.1016/j.bios.2013.12.068.

82. Godin M, Tabard-Cossa V, Miyahara Y, et al. Cantilever-based sensing: the origin of surface stress and optimization strategies. *Nanotechnology*. 2010;21(7):75501. doi:10.1088/0957-4484/21/7/075501.

83. Arroyo-Hernández M, Tamayo J, Costa-Krämer JL. Stress and DNA Assembly Differences on Cantilevers Gold Coated by Resistive and E-Beam Evaporation Techniques. *Langmuir*. 2009;25(18):10633-10638. doi:10.1021/la900696f.

84. Ghatkesar MK, Lang H-P, Gerber C, Hegner M, Braun T. Comprehensive Characterization of Molecular Interactions Based on Nanomechanics. *PLOS ONE*. 2008;3(11):e3610. doi:10.1371/journal.pone.0003610.

85. Stachowiak JC, Yue M, Castelino K, Chakraborty A, Majumdar A. Chemomechanics of Surface Stresses Induced by DNA Hybridization. *Langmuir*. 2006;22(1):263-268. doi:10.1021/la0521645.

86. Mukhopadhyay R, Sumbayev VV, Lorentzen M, Kjems J, Andreasen PA, Besenbacher F. Cantilever Sensor for Nanomechanical Detection of Specific Protein Conformations. *Nano Lett*. 2005;5(12):2385-2388. doi:10.1021/nl051449z.

87. Wu G, Datar RH, Hansen KM, Thundat T, Cote RJ, Majumdar A. Bioassay of prostate-specific antigen (PSA) using microcantilevers. *Nat Biotech*. 2001;19(9):856-860. doi:10.1038/nbt0901-856.

88. Wu G. Origin of nanomechanical cantilever motion generated from biomolecular interactions. *Proceedings of the National Academy of Sciences*. 2001;98(4):1560-1564. doi:10.1073/pnas.031362498.

89. Fritz J, Baller MK, Lang HP, et al. Translating Biomolecular Recognition into Nanomechanics. *Science*. 2000;288(5464):316-318. doi:10.1126/science.288.5464.316.

90. Lavrik NV, Sepaniak MJ, Datskos PG. Cantilever transducers as a platform for chemical and biological sensors. *Review of Scientific Instruments*. 2004;75(7):2229-2253. doi:10.1063/1.1763252.

91. Thundat T, Warmack RJ, Chen GY, Allison DP. Thermal and ambient-induced deflections of scanning force microscope cantilevers. *Applied Physics Letters*. 1994;64(21):2894–2896.

92. Berger R, Lang HP, Gerber C, et al. Micromechanical thermogravimetry. *Chemical Physics Letters*. 1998;294(4–5):363-369. doi:10.1016/S0009-2614(98)00817-3.

93. Fricke J, Obermeier E. Cantilever beam accelerometer based on surface micromachining technology. *J Micromech Microeng*. 1993;3(4):190. doi:10.1088/0960-1317/3/4/005.

94. Puers R, Lapadatu D. Electrostatic forces and their effects on capacitive mechanical sensors. *Sensors and Actuators A: Physical*. 1996;56(3):203-210. doi:10.1016/S0924-4247(96)01310-6.

95. Brunt TA, Rayment T, O'Shea SJ, Welland ME. Measuring the Surface Stresses in an Electrochemically Deposited Metal Monolayer: Pb on Au(111). *Langmuir*. 1996;12(24):5942-5946. doi:10.1021/la960564+.

96. Barnes JR, Stephenson RJ, Welland ME, Gerber C, Gimzewski JK. Photothermal spectroscopy with femtojoule sensitivity using a micromechanical device. *Nature*. 1994;372(6501):79-81. doi:10.1038/372079a0.

97. Lack FR, Willard GW, Fair IE. Some Improvements in Quartz Crystal Circuit Elements. *Bell System Technical Journal*. 1934;13(3):453-463. doi:10.1002/j.1538-7305.1934.tb00674.x.

98. Hewlett Packard®. Fundamentals of Quartz Oscillators. In: *Hewlett Packard Application Note 200.2*. Electronic Counters Series. ; 1997.

99. Rodahl M, Kasemo B. Frequency and dissipation-factor responses to localized liquid deposits on a QCM electrode. *Sensors and Actuators B: Chemical*. 1996;37(1):111–116.

100. Xi J, Chen J, Garcia M, Penn L. Quartz crystal microbalance in cell biology studies. *J Biochip Tissue chip S*. 2013;5:2153–777.

101. Sauerbrey G. Verwendung von Schwingquarzen zur Wägung dünner Schichten und zur Mikrowägung. *Zeitschrift für physik*. 1959;155(2):206–222.

102. Voinova MV, Jonson M, Kasemo B. On dissipation of quartz crystal microbalance as a mechanical spectroscopy tool. *Spectr-Int J*. 2004;18(4):537-544.

103. Rojas OJ, Jeong C, Turon X, Argyropoulos DS. Measurement of Cellulase Activity with Piezoelectric Resonators. In: *Materials, Chemicals, and Energy from Forest Biomass*. Vol 954. ACS Symposium Series. American Chemical Society; 2007:478-494. http://dx.doi.org/10.1021/bk-2007-0954.ch030. Accessed October 18, 2016.

104. Hu G, Heitmann JA, Rojas OJ. In Situ Monitoring of Cellulase Activity by Microgravimetry with a Quartz Crystal Microbalance. *J Phys Chem B*. 2009;113(44):14761-14768. doi:10.1021/jp907155v.

105. Liu Z, Choi H, Gatenholm P, Esker AR. Quartz Crystal Microbalance with Dissipation Monitoring and Surface Plasmon Resonance Studies of Carboxymethyl Cellulose Adsorption onto Regenerated Cellulose Surfaces. *Langmuir*. 2011;27(14):8718-8728. doi:10.1021/la200628a.

106. Turon X, Rojas OJ, Deinhammer RS. Enzymatic Kinetics of Cellulose Hydrolysis: A QCM-D Study. *Langmuir*. 2008;24(8):3880-3887. doi:10.1021/la7032753.

107. Cheng G, Liu Z, Murton JK, et al. Neutron Reflectometry and QCM-D Study of the Interaction of Cellulases with Films of Amorphous Cellulose. *Biomacromolecules*. 2011;12(6):2216-2224. doi:10.1021/bm200305u.

108. Kumagai A, Lee S-H, Endo T. Thin Film of Lignocellulosic Nanofibrils with Different Chemical Composition for QCM-D Study. *Biomacromolecules*. 2013;14(7):2420-2426. doi:10.1021/bm400553s.

109. Höök F, Kasemo B. The QCM-D technique for probing biomacromolecular recognition reactions. In: *Piezoelectric Sensors*. Springer; 2006:425–447. http://link.springer.com/chapter/10.1007/5346_034. Accessed November 28, 2016.

110. Cruys-Bagger N, Tatsumi H, Ren GR, Borch K, Westh P. Transient Kinetics and Rate-Limiting Steps for the Processive Cellobiohydrolase Cel7A: Effects of Substrate Structure and Carbohydrate Binding Domain. *Biochemistry*. 2013;52(49):8938-8948. doi:10.1021/bi401210n.

111. Beckham GT, Matthews JF, Peters B, Bomble YJ, Himmel ME, Crowley MF. Molecular-Level Origins of Biomass Recalcitrance: Decrystallization Free Energies for Four Common Cellulose Polymorphs. *J Phys Chem B*. 2011;115(14):4118-4127. doi:10.1021/jp1106394.

112. Fox JM, Levine SE, Clark DS, Blanch HW. Initial- and Processive-Cut Products Reveal Cellobiohydrolase Rate Limitations and the Role of Companion Enzymes. *Biochemistry*. 2012;51(1):442-452. doi:10.1021/bi2011543.

113. Gao D, Chundawat SPS, Sethi A, Balan V, Gnanakaran S, Dale BE. Increased enzyme binding to substrate is not necessary for more efficient cellulose hydrolysis. *PNAS*. 2013;110(27):10922-10927. doi:10.1073/pnas.1213426110.

114. Payne CM, Jiang W, Shirts MR, Himmel ME, Crowley MF, Beckham GT. Glycoside Hydrolase Processivity Is Directly Related to Oligosaccharide Binding Free Energy. *J Am Chem Soc*. 2013;135(50):18831-18839. doi:10.1021/ja407287f.

115. Das K, Ray D, Bandyopadhyay NR, Sengupta S. Study of the Properties of Microcrystalline Cellulose Particles from Different Renewable Resources by XRD, FTIR, Nanoindentation, TGA and SEM. *J Polym Environ*. 2010;18(3):355-363. doi:10.1007/s10924-010-0167-2.

116. Gao Q, Shen X, Lu X. Regenerated bacterial cellulose fibers prepared by the NMMO·H2O process. *Carbohydrate Polymers*. 2011;83(3):1253-1256. doi:10.1016/j.carbpol.2010.09.029.

117. O'Dell PJ, Mudinoor AR, Parikh SJ, Jeoh T. The effect of fibril length and architecture on the accessibility of reducing ends of cellulose Iα to Trichoderma reesei Cel7A. *Cellulose*. 2015;22(3):1697-1713. doi:10.1007/s10570-015-0618-y.

118. Ganner T, Aschl T, Eibinger M, et al. Tunable mixed amorphous–crystalline cellulose substrates (MACS) for dynamic degradation studies by atomic force microscopy in liquid environments. *Cellulose*. 2014;21(6):3927-3939. doi:10.1007/s10570-014-0419-8.

119. Schenzel K, Fischer S, Brendler E. New Method for Determining the Degree of Cellulose I Crystallinity by Means of FT Raman Spectroscopy. *Cellulose*. 12(3):223-231. doi:10.1007/s10570-004-3885-6.

120. Ahola S, Salmi J, Johansson L-S, Laine J, Österberg M. Model Films from Native Cellulose Nanofibrils. Preparation, Swelling, and Surface Interactions. *Biomacromolecules*. 2008;9(4):1273-1282. doi:10.1021/bm701317k.

121. Fardim P, Gustafsson J, von Schoultz S, Peltonen J, Holmbom B. Extractives on fiber surfaces investigated by XPS, ToF-SIMS and AFM. *Colloids and Surfaces A: Physicochemical and Engineering Aspects*. 2005;255(1–3):91-103. doi:10.1016/j.colsurfa.2004.12.027.

122. Yokota S, Kitaoka T, Wariishi H. Surface morphology of cellulose films prepared by spin coating on silicon oxide substrates pretreated with cationic polyelectrolyte. *Applied Surface Science*. 2007;253(9):4208-4214. doi:10.1016/j.apsusc.2006.09.037.

123. Zhang J, Zhang B, Zhang J, Lin L, Liu S, Ouyang P. Effect of phosphoric acid pretreatment on enzymatic hydrolysis of microcrystalline cellulose. *Biotechnology Advances*. 2010;28(5):613-619. doi:10.1016/j.biotechadv.2010.05.010.

124. Ahola S, Turon X, Österberg M, Laine J, Rojas OJ. Enzymatic Hydrolysis of Native Cellulose Nanofibrils and Other Cellulose Model Films: Effect of Surface Structure. *Langmuir*. 2008;24(20):11592-11599. doi:10.1021/la801550j.

125. Cerclier CV, Guyomard-Lack A, Cousin F, et al. Xyloglucan–Cellulose Nanocrystal Multilayered Films: Effect of Film Architecture on Enzymatic Hydrolysis. *Biomacromolecules*. 2013;14(10):3599-3609. doi:10.1021/bm400967e.

126. Hu G, Heitmann JA, Rojas OJ. Quantification of Cellulase Activity Using the Quartz Crystal Microbalance Technique. *Anal Chem*. 2009;81(5):1872-1880. doi:10.1021/ac802318t.

127. Jiang F, Kittle JD, Tan X, Esker AR, Roman M. Effects of Sulfate Groups on the Adsorption and Activity of Cellulases on Cellulose Substrates. *Langmuir*. 2013;29(10):3280-3291. doi:10.1021/la3040193.

128. Josefsson P, Henriksson G, Wågberg L. The Physical Action of Cellulases Revealed by a Quartz Crystal Microbalance Study Using Ultrathin Cellulose Films and Pure Cellulases. *Biomacromolecules*. 2008;9(1):249-254. doi:10.1021/bm700980b.

129. Kittle JD, Du X, Jiang F, et al. Equilibrium Water Contents of Cellulose Films Determined via Solvent Exchange and Quartz Crystal Microbalance with Dissipation Monitoring. *Biomacromolecules*. 2011;12(8):2881-2887. doi:10.1021/bm200352q.

130. Martín-Sampedro R, Rahikainen JL, Johansson L-S, et al. Preferential Adsorption and Activity of Monocomponent Cellulases on Lignocellulose Thin Films with Varying Lignin Content. *Biomacromolecules*. 2013;14(4):1231-1239. doi:10.1021/bm400230s.

131. Maurer SA, Bedbrook CN, Radke CJ. Competitive Sorption Kinetics of Inhibited Endo- and Exoglucanases on a Model Cellulose Substrate. *Langmuir*. 2012;28(41):14598-14608. doi:10.1021/la3024524.

132. Maurer SA, Brady NW, Fajardo NP, Radke CJ. Surface kinetics for cooperative fungal cellulase digestion of cellulose from quartz crystal microgravimetry. *Journal of Colloid and Interface Science*. 2013;394:498-508. doi:10.1016/j.jcis.2012.12.022.

133. Mohan T, Kargl R, Doliška A, Ehmann HMA, Ribitsch V, Stana-Kleinschek K. Enzymatic digestion of partially and fully regenerated cellulose model films from trimethylsilyl cellulose. *Carbohydrate Polymers*. 2013;93(1):191-198. doi:10.1016/j.carbpol.2012.02.033.

134. Suchy M, Linder MB, Tammelin T, Campbell JM, Vuorinen T, Kontturi E. Quantitative Assessment of the Enzymatic Degradation of Amorphous Cellulose by Using a Quartz Crystal Microbalance with Dissipation Monitoring. *Langmuir*. 2011;27(14):8819-8828. doi:10.1021/la2014418.

135. Thakur G, Jiang K, Lee D, Prashanthi K, Kim S, Thundat T. Investigation of pH-Induced Protein Conformation Changes by Nanomechanical Deflection. *Langmuir*. 2014;30(8):2109-2116. doi:10.1021/la403981t.

136. Longo G, Alonso-Sarduy L, Rio LM, et al. Rapid detection of bacterial resistance to antibiotics using AFM cantilevers as nanomechanical sensors. *Nat Nano*. 2013;8(7):522-526. doi:10.1038/nnano.2013.120.

137. Tamayo J, Kosaka PM, Ruz JJ, Paulo ÁS, Calleja M. Biosensors based on nanomechanical systems. *Chem Soc Rev*. 2013;42(3):1287-1311. doi:10.1039/C2CS35293A.

138. Buchapudi KR, Huang X, Yang X, Ji H-F, Thundat T. Microcantilever biosensors for chemicals and bioorganisms. *Analyst*. 2011;136(8):1539-1556. doi:10.1039/C0AN01007C.

139. Boisen A, Dohn S, Keller SS, Schmid S, Tenje M. Cantilever-like micromechanical sensors. *Rep Prog Phys*. 2011;74(3):36101. doi:10.1088/0034-4885/74/3/036101.

140. Arlett JL, Myers EB, Roukes ML. Comparative advantages of mechanical biosensors. *Nat Nano*. 2011;6(4):203-215. doi:10.1038/nnano.2011.44.

141. Braun T, Ghatkesar MK, Backmann N, et al. Quantitative time-resolved measurement of membrane protein–ligand interactions using microcantilever array sensors. *Nat Nano*. 2009;4(3):179-185. doi:10.1038/nnano.2008.398.

142. Ndieyira JW, Watari M, Barrera AD, et al. Nanomechanical detection of antibiotic–mucopeptide binding in a model for superbug drug resistance. *Nat Nano*. 2008;3(11):691-696. doi:10.1038/nnano.2008.275.

143. Shekhawat GS, Dravid VP. Biosensors: Microcantilevers to lift biomolecules. *Nat Nano*. 2015;10(10):830-831. doi:10.1038/nnano.2015.187.

144. Ndieyira JW, Kappeler N, Logan S, et al. Surface-stress sensors for rapid and ultrasensitive detection of active free drugs in human serum. *Nat Nano*. 2014;9(3):225-232. doi:10.1038/nnano.2014.33.

145. Huber F, Lang HP, Backmann N, Rimoldi D, Gerber C. Direct detection of a BRAF mutation in total RNA from melanoma cells using cantilever arrays. *Nat Nano*. 2013;8(2):125-129. doi:10.1038/nnano.2012.263.

146. Shekhawat GS, Tark S-H, Dravid VP. MOSFET-Embedded Microcantilevers for Measuring Deflection in Biomolecular Sensors. *Science*. 2006;311(5767):1592-1595. doi:10.1126/science.1122588.

147. Zhang J, Lang HP, Huber F, et al. Rapid and label-free nanomechanical detection of biomarker transcripts in human RNA. *Nat Nano*. 2006;1(3):214-220. doi:10.1038/nnano.2006.134.

148. Wu G, Ji H, Hansen K, et al. Origin of nanomechanical cantilever motion generated from biomolecular interactions. *PNAS*. 2001;98(4):1560-1564. doi:10.1073/pnas.98.4.1560.

149. Wasisto HS, Merzsch S, Waag A, Uhde E, Salthammer T, Peiner E. Airborne engineered nanoparticle mass sensor based on a silicon resonant cantilever. *Sensors and Actuators B: Chemical*. 2013;180:77-89. doi:10.1016/j.snb.2012.04.003.

150. Sharma H, Mutharasan R. Rapid and sensitive immunodetection of Listeria monocytogenes in milk using a novel piezoelectric cantilever sensor. *Biosensors and Bioelectronics*. 2013;45:158-162. doi:10.1016/j.bios.2013.01.068.

151. Sharma H, Mutharasan R. hlyA Gene-Based Sensitive Detection of Listeria monocytogenes Using a Novel Cantilever Sensor. *Anal Chem*. 2013;85(6):3222-3228. doi:10.1021/ac303561c.

152. Yin T-I, Zhao Y, Horak J, et al. A micro-cantilever sensor chip based on contact angle analysis for a label-free troponin I immunoassay. *Lab on a Chip*. 2013;13(5):834. doi:10.1039/c2lc40767a.

153. Steffens C, Manzoli A, Oliveira JE, Leite FL, Correa DS, Herrmann PSP. Bio-inspired sensor for insect pheromone analysis based on polyaniline functionalized AFM cantilever sensor. *Sensors and Actuators B: Chemical*. 2014;191:643-649. doi:10.1016/j.snb.2013.10.053.

154. Okan M, Sari E, Duman M. Molecularly imprinted polymer based micromechanical cantilever sensor system for the selective determination of ciprofloxacin. *Biosensors and Bioelectronics*. 2016. doi:10.1016/j.bios.2016.08.047.

155. Kim D, Hong S, Jang J, Park J. Simultaneous determination of position and mass in the cantilever sensor using transfer function method. *Applied Physics Letters*. 2013;103(3):33108. doi:10.1063/1.4813839.

156. Chae M-S, Kim J, Yoo YK, Kang JY, Lee JH, Hwang KS. A Micro-Preconcentrator Combined Olfactory Sensing System with a Micromechanical Cantilever Sensor for Detecting 2,4-Dinitrotoluene Gas Vapor. *Sensors*. 2015;15(8):18167-18177. doi:10.3390/s150818167.

157. Rust P, Cereghetti D, Dual J. A micro-liter viscosity and density sensor for the rheological characterization of DNA solutions in the kilo-hertz range. *Lab on a Chip*. 2013;13(24):4794. doi:10.1039/c3lc50857a.

158. Johnson BN, Mutharasan R. Biosensing using dynamic-mode cantilever sensors: A review. *Biosensors and Bioelectronics*. 2012;32(1):1-18. doi:10.1016/j.bios.2011.10.054.

159. Fritz J. Cantilever biosensors. *Analyst*. 2008;133(7):855-863. doi:10.1039/B718174D.

160. Raiteri R, Grattarola M, Butt H-J, Skládal P. Micromechanical cantilever-based biosensors. *Sensors and Actuators B: Chemical*. 2001;79(2–3):115-126. doi:10.1016/S0925-4005(01)00856-5.

161. Vashist SK. A review of microcantilevers for sensing applications. *Journal of Nanotechnology Online*. 2007;3:1–18.

162. Cruys-Bagger N, Tatsumi H, Borch K, Westh P. A graphene screen-printed carbon electrode for real-time measurements of unoccupied active sites in a cellulase. *Analytical Biochemistry*. 2014;447:162-168. doi:10.1016/j.ab.2013.11.024.

163. Maurer SA, Bedbrook CN, Radke CJ. Cellulase Adsorption and Reactivity on a Cellulose Surface from Flow Ellipsometry. *Ind Eng Chem Res*. 2012;51(35):11389-11400. doi:10.1021/ie3008538.

164. Murphy L, Baumann MJ, Borch K, Sweeney M, Westh P. An enzymatic signal amplification system for calorimetric studies of cellobiohydrolases. *Analytical Biochemistry*. 2010;404(2):140-148. doi:10.1016/j.ab.2010.04.020.

165. Murphy L, Borch K, McFarland KC, Bohlin C, Westh P. A calorimetric assay for enzymatic saccharification of biomass. *Enzyme and Microbial Technology*. 2010;46(2):141-146. doi:10.1016/j.enzmictec.2009.09.009.

166. Olsen SN, Bohlin C, Murphy L, et al. Effects of non-ionic surfactants on the interactions between cellulases and tannic acid: A model system for cellulase–poly-phenol interactions. *Enzyme and Microbial Technology*. 2011;49(4):353-359. doi:10.1016/j.enzmictec.2011.06.015.

167. Murphy L, Bohlin C, Baumann MJ, et al. Product inhibition of five Hypocrea jecorina cellulases. *Enzyme and Microbial Technology*. 2013;52(3):163-169. doi:10.1016/j.enzmictec.2013.01.002.

168. Igarashi K, Koivula A, Wada M, Kimura S, Penttilä M, Samejima M. High Speed Atomic Force Microscopy Visualizes Processive Movement of Trichoderma reesei Cellobiohydrolase I on Crystalline Cellulose. *J Biol Chem*. 2009;284(52):36186-36190. doi:10.1074/jbc.M109.034611.

169. Fox JM, Jess P, Jambusaria RB, et al. A single-molecule analysis reveals morphological targets for cellulase synergy. *Nat Chem Biol*. 2013;9(6):356-361. doi:10.1038/nchembio.1227.

170. Ganner T, Bubner P, Eibinger M, Mayrhofer C, Plank H, Nidetzky B. Dissecting and reconstructing synergism: In situ visualization of cooperativity among cellulases. *J Biol Chem*. 2012;287(52):43215-43222. doi:10.1074/jbc.M112.419952.

171. Levine SE, Fox JM, Blanch HW, Clark DS. A mechanistic model of the enzymatic hydrolysis of cellulose. *Biotechnol Bioeng*. 2010;107(1):37-51. doi:10.1002/bit.22789.

172. Zhou W, Schüttler H-B, Hao Z, Xu Y. Cellulose hydrolysis in evolving substrate morphologies I: A general modeling formalism. *Biotechnol Bioeng*. 2009;104(2):261-274. doi:10.1002/bit.22389.

173. Zhou W, Xu Y, Schüttler H-B. Cellulose hydrolysis in evolving substrate morphologies III: Time-scale analysis. *Biotechnol Bioeng*. 2010;107(2):224-234. doi:10.1002/bit.22814.

174. Bansal P, Hall M, Realff MJ, Lee JH, Bommarius AS. Modeling cellulase kinetics on lignocellulosic substrates. *Biotechnology Advances*. 2009;27(6):833-848. doi:10.1016/j.biotechadv.2009.06.005.

175. Hall M, Bansal P, Lee JH, Realff MJ, Bommarius AS. Cellulose crystallinity – a key predictor of the enzymatic hydrolysis rate. *FEBS Journal*. 2010;277(6):1571–1582. doi:10.1111/j.1742-4658.2010.07585.x.

176. Igarashi K. Cellulases: Cooperative biomass breakdown. *Nat Chem Biol*. 2013;9(6):350-351. doi:10.1038/nchembio.1237.

177. Kostylev M, Wilson D. Synergistic interactions in cellulose hydrolysis. *Biofuels*. 2012;3(1):61-70. doi:10.4155/bfs.11.150.

178. Lassig JP, Shultz MD, Gooch MG, Evans BR, Woodward J. Inhibition of Cellobiohydrolase I from Trichoderma reesei by Palladium. *Archives of Biochemistry and Biophysics*. 1995;322(1):119-126. doi:10.1006/abbi.1995.1443.

179. Shultz MD, Lassig JP, Gooch MG, Evans BR, Woodward J. Palladium - A New Inhibitor of Cellulase Activities. *Biochemical and Biophysical Research Communications*. 1995;209(3):1046-1052. doi:10.1006/bbrc.1995.1603.

180. Lee I, Evans BR, Lane LM, Woodward J. Substrate-enzyme interactions in cellulase systems. *Bioresource Technology*. 1996;58(2):163-169. doi:10.1016/S0960-8524(96)00095-8.

181. Lee I, Evans BR, Woodward J. The mechanism of cellulase action on cotton fibers: evidence from atomic force microscopy. *Ultramicroscopy*. 2000;82(1–4):213-221. doi:10.1016/s0304-3991(99)00158-8.

182. Jenoptik. Roughness measuring systems from Jenoptik – Surface texture parameters in practice. 2015. https://www.jenoptik.com/cms/products.nsf/0/97AF514ED6DFF391C1257E12004E7E23/$File/surface_en_10037109_03_2015.pdf?Open.

183. Carlson PA, Gelb MH, Yager P. Zero-order interfacial enzymatic degradation of phospholipid tubules. *Biophys J*. 1997;73(1):230-238.

184. Skold CN, Gibbons I, Russell ME, Juaristi E, Rowley GL, Ullman EF. Action of β-galactosidase on novel synthetic macromolecular substrates. A processive enzymic reaction controlled by coulombic interactions. *Biochimica et Biophysica Acta (BBA) - Protein Structure and Molecular Enzymology*. 1985;830(1):64-70. doi:10.1016/0167-4838(85)90132-3.

185. Kostylev M, Wilson D. A Distinct Model of Synergism between a Processive Endocellulase (TfCel9A) and an Exocellulase (TfCel48A) from Thermobifida fusca. *Appl Environ Microbiol*. 2014;80(1):339-344. doi:10.1128/AEM.02706-13.

186. Kostylev M, Wilson D. Two-Parameter Kinetic Model Based on a Time-Dependent Activity Coefficient Accurately Describes Enzymatic Cellulose Digestion. *Biochemistry*. 2013;52(33):5656-5664. doi:10.1021/bi400358v.

187. Scriven LE. Physics and applications of dip coating and spin coating. In: *MRS Proceedings*. Vol 121. Cambridge Univ Press; 1988:717. http://journals.cambridge.org/abstract_S1946427400485180. Accessed November 28, 2016.

188. Lawrence CJ. The mechanics of spin coating of polymer films. *Physics of Fluids (1958-1988)*. 1988;31(10):2786–2795.

189. Hall DB, Underhill P, Torkelson JM. Spin coating of thin and ultrathin polymer films. *Polymer Engineering & Science*. 1998;38(12):2039–2045.

190. Bornside DE, Macosko CW, Scriven LE. Spin coating: One-dimensional model. *Journal of Applied Physics*. 1989;66(11):5185–5193.

191. Spin Coating: A Guide to Theory and Techniques. Ossila. https://www.ossila.com/pages/spin-coating. Accessed November 28, 2016.

192. Khademi S, Zhang D, Swanson SM, Wartenberg A, Witte K, Meyer EF. Determination of the structure of an endoglucanase from *Aspergillus niger* and its mode of inhibition by palladium chloride. *Acta Crystallographica Section D Biological Crystallography*. 2002;58(4):660-667. doi:10.1107/S0907444902003360.

193. Rosgaard L, Pedersen S, Langston J, Akerhielm D, Cherry JR, Meyer AS. Evaluation of Minimal Trichoderma reesei Cellulase Mixtures on Differently Pretreated Barley Straw Substrates. *Biotechnol Progress*. 2007;23(6):1270-1276. doi:10.1021/bp070329p.

194. Deshpande MV, Eriksson K-E, Göran Pettersson L. An assay for selective determination of exo-1,4,-β-glucanases in a mixture of cellulolytic enzymes. *Analytical Biochemistry*. 1984;138(2):481-487. doi:10.1016/0003-2697(84)90843-1.

195. Bubner P, Dohr J, Plank H, Mayrhofer C, Nidetzky B. Cellulases Dig Deep. *Journal of Biological Chemistry*. 2012;287(4):2759-2765. doi:10.1074/jbc.M111.257717.

196. Eibinger M, Bubner P, Ganner T, Plank H, Nidetzky B. Surface structural dynamics of enzymatic cellulose degradation, revealed by combined kinetic and atomic force microscopy studies. *FEBS Journal*. 2014;281(1):275–290. doi:10.1111/febs.12594.

197. Jaušovec D, Vončina B, Angelescu D, Nylander T, Lindman B. Enzymatic Degradation of Model Cellulose Film Pre-Treated with Antimicrobial Agent. *Journal of Dispersion Science and Technology*. 2009;30(6):929-936. doi:10.1080/01932690802646314.

198. Liu Y-S, Baker JO, Zeng Y, Himmel ME, Haas T, Ding S-Y. Cellobiohydrolase Hydrolyzes Crystalline Cellulose on Hydrophobic Faces. *J Biol Chem*. 2011;286(13):11195-11201. doi:10.1074/jbc.M110.216556.

199. Wang J, Quirk A, Lipkowski J, et al. Real-Time Observation of the Swelling and Hydrolysis of a Single Crystalline Cellulose Fiber Catalyzed by Cellulase 7B from Trichoderma reesei. *Langmuir*. 2012;28(25):9664-9672. doi:10.1021/la301030f.

200. Zhao L, Bulhassan A, Yang G, Ji H-F, Xi J. Real-time detection of the morphological change in cellulose by a nanomechanical sensor. *Biotechnology and Bioengineering*. 2010;107(1):190-194. doi:10.1002/bit.22754.

201. Akar E, Altınışık A, Seki Y. Preparation of pH- and ionic-strength responsive biodegradable fumaric acid crosslinked carboxymethyl cellulose. *Carbohydrate Polymers*. 2012;90(4):1634-1641. doi:10.1016/j.carbpol.2012.07.043.

202. Calvimontes A, Lant NJ, Dutschk V. Cooperative Action of Cellulase Enzyme and Carboxymethyl Cellulose on Cotton Fabric Cleanability from a Topographical Standpoint. *J Surfact Deterg*. 2011;14(3):307-316. doi:10.1007/s11743-011-1248-5.

203. Mazeau K. On the external morphology of native cellulose microfibrils. *Carbohydrate Polymers*. 2011;84(1):524-532. doi:10.1016/j.carbpol.2010.12.016.

204. Tébéka IRM, Silva AGL, Petri DFS. Hydrolytic Activity of Free and Immobilized Cellulase. *Langmuir*. 2009;25(3):1582-1587. doi:10.1021/la802882s.

205. Prasad K, Kaneko Y, Kadokawa J. Novel Gelling Systems of κ-, ι- and λ-Carrageenans and their Composite Gels with Cellulose Using Ionic Liquid. *Macromolecular Bioscience*. 2009;9(4):376–382. doi:10.1002/mabi.200800179.

206. Woodward J, Brown J, Evans B, Affholter K. Papain digestion of crude Trichoderma reesei cellulase: purification and properties of cellobiohydrolase I and II core proteins. *Biotechnology and Applied Biochemistry*. 1994;19(2):141-153. doi:10.1111/j.1470-8744.1994.tb00291.x.

207. Calvimontes A, Stamm M, Dutschk V. Effect of Cellulase Enzyme on Cellulose Nano-topography. *Tenside Surfactants Detergents*. 2009;46(6):368-372. doi:10.3139/113.110044.

208. Woodward J, Gooch MG, Shultz MD. *The Catalytic Inactivation of Cellulase Enzyme Components by Palladium Complexes*. Oak Ridge National Lab., TN (United States); 1993. http://www.osti.gov/scitech/biblio/10103749. Accessed April 28, 2016.

209. Park S, Baker JO, Himmel ME, Parilla PA, Johnson DK. Cellulose crystallinity index: measurement techniques and their impact on interpreting cellulase performance. *Biotechnology for Biofuels*. 2010;3(1):10. doi:10.1186/1754-6834-3-10.

210. Segal L, Creely JJ, Martin AE, Conrad CM. An Empirical Method for Estimating the Degree of Crystallinity of Native Cellulose Using the X-Ray Diffractometer. *Textile Research Journal*. 1959;29(10):786-794. doi:10.1177/004051755902901003.

211. Yohannes G, Wiedmer SK, Elomaa M, Jussila M, Aseyev V, Riekkola M-L. Thermal aggregation of bovine serum albumin studied by asymmetrical flow field-flow fractionation. *Analytica Chimica Acta*. 2010;675(2):191-198. doi:10.1016/j.aca.2010.07.016.

212. Sharon N, Lis H. History of lectins: from hemagglutinins to biological recognition molecules. *Glycobiology*. 2004;14(11):53R-62R. doi:10.1093/glycob/cwh122.

213. Wang H, Mochidzuki K, Kobayashi S, Hiraide H, Wang X, Cui Z. Effect of Bovine Serum Albumin (BSA) on Enzymatic Cellulose Hydrolysis. *Appl Biochem Biotechnol*. 2013;170(3):541-551. doi:10.1007/s12010-013-0208-0.

214. Nidetzky B, Steiner W, Claeyssens M. Cellulose hydrolysis by the cellulases from Trichoderma reesei: adsorptions of two cellobiohydrolases, two endocellulases and their core proteins on filter paper and their relation to hydrolysis. *Biochemical Journal*. 1994;303(3):817-823. doi:10.1042/bj3030817.

215. Medve J, Ståhlberg J, Tjerneld F. Isotherms for adsorption of cellobiohydrolase I and II fromtrichoderma reesei on microcrystalline cellulose. *Appl Biochem Biotechnol*. 1997;66(1):39-56. doi:10.1007/BF02788806.

216. Beldman G, Voragen AGJ, Rombouts FM, Searle-van Leeuwen MF, Pilnik W. Adsorption and kinetic behavior of purified endoglucanases and exoglucanases from Trichoderma viride. *Biotechnol Bioeng*. 1987;30(2):251-257. doi:10.1002/bit.260300215.

217. Su S, Pelton R. Bovine Serum Albumin (BSA) as an adhesive for wet cellulose. *Cellulose*. 2006;13(5):537-545. doi:10.1007/s10570-006-9064-1.

218. Woodward J. Synergism in cellulase systems. *Bioresource Technology*. 1991;36(1):67-75. doi:10.1016/0960-8524(91)90100-X.

219. Kumar R, Wyman CE. Does change in accessibility with conversion depend on both the substrate and pretreatment technology? *Bioresource Technology*. 2009;100(18):4193-4202. doi:10.1016/j.biortech.2008.11.058.

220. Wyman CE, ed. *Aqueous Pretreatment of Plant Biomass for Biological and Chemical Conversion to Fuels and Chemicals*. 1 edition. Chichester, West Sussex, United Kingdom: Wiley; 2013.

221. Ståhlberg J, Johansson G, Pettersson G. A New Model For Enzymatic Hydrolysis of Cellulose Based on the Two-Domain Structure of Cellobiohydrolase I. *Nat Biotech*. 1991;9(3):286-290. doi:10.1038/nbt0391-286.

222. Cavaco-Paulo A, Almeida L, Bishop D. Hydrolysis of Cotton Cellulose by Engineered Cellulases from Trichoderma reesei. *Textile Research Journal*. 1998;68(4):273-280. doi:10.1177/004051759806800405.

223. Hobdey SE, Knott BC, Momeni MH, et al. Biochemical and Structural Characterizations of Two Dictyostelium Cellobiohydrolases from the Amoebozoa Kingdom Reveal a High Level of Conservation between Distant Phylogenetic Trees of Life. *Appl Environ Microbiol*. 2016;82(11):3395-3409. doi:10.1128/AEM.00163-16.

224. Punsuvon V. Optimization of Delignification and Enzyme Hydrolysis of Steam Exploded Oil Palm Trunk for Ethanol Production by Response Surface Methodology. In: Chandel A, ed. *Sustainable Degradation of Lignocellulosic Biomass - Techniques, Applications and Commercialization*. InTech; 2013. http://www.intechopen.com/books/sustainable-degradation-of-lignocellulosic-biomass-techniques-applications-and-commercialization/optimization-of-delignification-and-enzyme-hydrolysis-of-steam-exploded-oil-palm-trunk-for-ethanol-p. Accessed August 19, 2016.

225. Ungurean M, Paul C, Peter F. Cellulase immobilized by sol–gel entrapment for efficient hydrolysis of cellulose. *Bioprocess Biosyst Eng*. 2012;36(10):1327-1338. doi:10.1007/s00449-012-0835-9.

226. Voutilainen SP, Puranen T, Siika-aho M, et al. Cloning, expression, and characterization of novel thermostable family 7 cellobiohydrolases. *Biotechnol Bioeng*. 2008;101(3):515-528. doi:10.1002/bit.21940.

227. Hall M, Bansal P, Lee JH, Realff MJ, Bommarius AS. Cellulose crystallinity – a key predictor of the enzymatic hydrolysis rate. *FEBS Journal*. 2010;277(6):1571-1582. doi:10.1111/j.1742-4658.2010.07585.x.

228. Anglès MN, Dufresne A. Plasticized Starch/Tunicin Whiskers Nanocomposite Materials. 2. Mechanical Behavior. *Macromolecules*. 2001;34(9):2921-2931. doi:10.1021/ma001555h.

229. Araki J, Wada M, Kuga S, Okano T. Birefringent Glassy Phase of a Cellulose Microcrystal Suspension. *Langmuir*. 2000;16(6):2413-2415. doi:10.1021/la9911180.

230. Bendahou A, Habibi Y, Kaddami H, Dufresne A. Physico-Chemical Characterization of Palm from Phoenix Dactylifera–L, Preparation of Cellulose Whiskers and Natural Rubber–Based Nanocomposites. *Journal of Biobased Materials and Bioenergy*. 2009;3(1):81-90. doi:10.1166/jbmb.2009.1011.

231. Cao X, Chen Y, Chang PR, Stumborg M, Huneault MA. Green composites reinforced with hemp nanocrystals in plasticized starch. *J Appl Polym Sci*. 2008;109(6):3804-3810. doi:10.1002/app.28418.

232. Habibi Y, Dufresne A. Highly Filled Bionanocomposites from Functionalized Polysaccharide Nanocrystals. *Biomacromolecules*. 2008;9(7):1974-1980. doi:10.1021/bm8001717.

233. Hirai A, Inui O, Horii F, Tsuji M. Phase Separation Behavior in Aqueous Suspensions of Bacterial Cellulose Nanocrystals Prepared by Sulfuric Acid Treatment. *Langmuir*. 2009;25(1):497-502. doi:10.1021/la802947m.

234. Siqueira G, Bras J, Dufresne A. Cellulose Whiskers versus Microfibrils: Influence of the Nature of the Nanoparticle and its Surface Functionalization on the Thermal and Mechanical Properties of Nanocomposites. *Biomacromolecules*. 2009;10(2):425-432. doi:10.1021/bm801193d.

235. Nishiyama Y. Structure and properties of the cellulose microfibril. *Journal of Wood Science*. 2009;55(4):241-249. doi:10.1007/s10086-009-1029-1.

236. Wang M, Liu K, Dai L, Zhang J, Fang X. The structural and biochemical basis for cellulose biodegradation. *J Chem Technol Biotechnol*. 2013;88(4):491-500. doi:10.1002/jctb.3987.

237. Li Q, Renneckar S. Molecularly thin nanoparticles from cellulose: isolation of sub-microfibrillar structures. *Cellulose*. 2009;16(6):1025-1032. doi:10.1007/s10570-009-9329-6.

238. Saito T, Nishiyama Y, Putaux J-L, Vignon M, Isogai A. Homogeneous Suspensions of Individualized Microfibrils from TEMPO-Catalyzed Oxidation of Native Cellulose. *Biomacromolecules*. 2006;7(6):1687-1691. doi:10.1021/bm060154s.

239. Yokota S, Ueno T, Kitaoka T, Wariishi H. Molecular imaging of single cellulose chains aligned on a highly oriented pyrolytic graphite surface. *Carbohydrate Research*. 2007;342(17):2593-2598. doi:10.1016/j.carres.2007.08.018.

240. Cho HM, Gross AS, Chu J-W. Dissecting Force Interactions in Cellulose Deconstruction Reveals the Required Solvent Versatility for Overcoming Biomass Recalcitrance. *J Am Chem Soc*. 2011;133(35):14033-14041. doi:10.1021/ja2046155.

241. Kuo C-H, Lee C-K. Enhancement of enzymatic saccharification of cellulose by cellulose dissolution pretreatments. *Carbohydrate Polymers*. 2009;77(1):41-46. doi:10.1016/j.carbpol.2008.12.003.

242. Wan Z, Li L, Cui S. Capturing the portrait of isolated individual natural cellulose molecules. *Biopolymers*. 2008;89(12):1170-1173. doi:10.1002/bip.21070.

243. Igarashi K, Uchihashi T, Koivula A, et al. Traffic Jams Reduce Hydrolytic Efficiency of Cellulase on Cellulose Surface. *Science*. 2011;333(6047):1279-1282. doi:10.1126/science.1208386.

244. Gardiner ES, Sarko A. Packing analysis of carbohydrates and polysaccharides. 16. The crystal structures of celluloses IVI and IVII. *Can J Chem*. 1985;63(1):173-180. doi:10.1139/v85-027.

245. Wada M, Chanzy H, Nishiyama Y, Langan P. Cellulose III_I Crystal Structure and Hydrogen Bonding by Synchrotron X-ray and Neutron Fiber Diffraction. *Macromolecules*. 2004;37(23):8548-8555. doi:10.1021/ma0485585.

246. Cintrón MS, Johnson GP, French AD. Young's modulus calculations for cellulose Iβ by MM3 and quantum mechanics. *Cellulose*. 2011;18(3):505-516. doi:10.1007/s10570-011-9507-1.

247. French AD, Johnson GP. Quantum mechanics studies of cellobiose conformations. *Can J Chem*. 2006;84(4):603-612. doi:10.1139/v06-050.

248. Kubicki JD, Mohamed MN-A, Watts HD. Quantum mechanical modeling of the structures, energetics and spectral properties of Iα and Iβ cellulose. *Cellulose*. 2013;20(1):9-23. doi:10.1007/s10570-012-9838-6.

249. Matthews JF, Skopec CE, Mason PE, et al. Computer simulation studies of microcrystalline cellulose Iβ. *Carbohydrate Research*. 2006;341(1):138-152. doi:10.1016/j.carres.2005.09.028.

250. Paavilainen S, Róg T, Vattulainen I. Analysis of Twisting of Cellulose Nanofibrils in Atomistic Molecular Dynamics Simulations. *J Phys Chem B*. 2011;115(14):3747-3755. doi:10.1021/jp111459b.

251. Zhao Z, Shklyaev OE, Nili A, et al. Cellulose Microfibril Twist, Mechanics, and Implication for Cellulose Biosynthesis. *J Phys Chem A*. 2013;117(12):2580-2589. doi:10.1021/jp3089929.

252. Bergenstråhle M, Thormann E, Nordgren N, Berglund LA. Force Pulling of Single Cellulose Chains at the Crystalline Cellulose−Liquid Interface: A Molecular Dynamics Study. *Langmuir*. 2009;25(8):4635-4642. doi:10.1021/la803915c.

253. Li Y, Lin M, Davenport JW. Ab Initio Studies of Cellulose I: Crystal Structure, Intermolecular Forces, and Interactions with Water. *J Phys Chem C*. 2011;115(23):11533-11539. doi:10.1021/jp2006759.

254. Parthasarathi R, Bellesia G, Chundawat SPS, Dale BE, Langan P, Gnanakaran S. Insights into Hydrogen Bonding and Stacking Interactions in Cellulose. *J Phys Chem A*. 2011;115(49):14191-14202. doi:10.1021/jp203620x.

255. Tanaka F, Fukui N. The behavior of cellulose molecules in aqueous environments. *Cellulose*. 2004;11(1):33-38. doi:10.1023/B:CELL.0000014769.01795.7f.

256. Heiner AP, Teleman O. Interface between Monoclinic Crystalline Cellulose and Water: Breakdown of the Odd/Even Duplicity. *Langmuir*. 1997;13(3):511-518. doi:10.1021/la960886d.

257. Chami Khazraji A, Robert S. Self-Assembly and Intermolecular Forces When Cellulose and Water Interact Using Molecular Modeling. *Journal of Nanomaterials*. 2013;2013:e745979. doi:10.1155/2013/745979.

258. Aulin C, Ahola S, Josefsson P, et al. Nanoscale Cellulose Films with Different Crystallinities and Mesostructures—Their Surface Properties and Interaction with Water. *Langmuir*. 2009;25(13):7675-7685. doi:10.1021/la900323n.

259. Divne C, Ståhlberg J, Reinikainen T, et al. The Three-Dimensional Crystal Structure of the Catalytic Core of Cellobiohydrolase I from Trichoderma reesei. *Science*. 1994;265(5171):524-528.

260. Divne C, Ståhlberg J, Teeri TT, Jones TA. High-resolution crystal structures reveal how a cellulose chain is bound in the 50 Å long tunnel of cellobiohydrolase I from Trichoderma reesei. *Journal of Molecular Biology*. 1998;275(2):309-325. doi:10.1006/jmbi.1997.1437.

261. Kleywegt GJ, Zou J-Y, Divne C, et al. The crystal structure of the catalytic core domain of endoglucanase I from Trichoderma reesei at 3.6 Å resolution, and a comparison with related enzymes1. *Journal of Molecular Biology*. 1997;272(3):383-397. doi:10.1006/jmbi.1997.1243.

262. Jorgensen WL, Chandrasekhar J, Madura JD, Impey RW, Klein ML. Comparison of simple potential functions for simulating liquid water. *The Journal of Chemical Physics*. 1983;79(2):926-935. doi:10.1063/1.445869.

263. Guvench O, Greene SN, Kamath G, et al. Additive empirical force field for hexopyranose monosaccharides. *J Comput Chem*. 2008;29(15):2543-2564. doi:10.1002/jcc.21004.

264. Guvench O, Hatcher E, Venable RM, Pastor RW, MacKerell AD. CHARMM Additive All-Atom Force Field for Glycosidic Linkages between Hexopyranoses. *J Chem Theory Comput*. 2009;5(9):2353-2370. doi:10.1021/ct900242e.

265. Phillips JC, Braun R, Wang W, et al. Scalable molecular dynamics with NAMD. *J Comput Chem*. 2005;26(16):1781-1802. doi:10.1002/jcc.20289.

266. Soo WC, Lauer H, Wenz G, Bruns M, Petri DFS. Formation of dense cellulose monolayers on silver surfaces. *Journal of the Brazilian Chemical Society*. 2000;11(1):11-15. doi:10.1590/S0103-50532000000100003.

267. Guzmán DL, Roland JT, Keer H, et al. Using steered molecular dynamics simulations and single-molecule force spectroscopy to guide the rational design of biomimetic modular polymeric materials. *Polymer*. 2008;49(18):3892-3901. doi:10.1016/j.polymer.2008.06.047.

268. Verdaguer A, Weis C, Oncins G, Ketteler G, Bluhm H, Salmeron M. Growth and Structure of Water on SiO2 Films on Si Investigated by Kelvin Probe Microscopy and in Situ X-ray Spectroscopies. *Langmuir*. 2007;23(19):9699-9703. doi:10.1021/la700893w.

269. Mascini M. A Brief Story of Biosensor Technology. In: *Biotechnological Applications of Photosynthetic Proteins: Biochips, Biosensors and Biodevices*. Biotechnology Intelligence Unit. Springer US; 2006:4-10. http://link.springer.com/chapter/10.1007/978-0-387-36672-2_2. Accessed November 28, 2016.

270. Pancrazio JJ, Whelan JP, Borkholder DA, Ma W, Stenger DA. Development and application of cell-based biosensors. *Ann Biomed Eng*. 1999;27(6):697-711.

271. Banerjee P, Bhunia AK. Mammalian cell-based biosensors for pathogens and toxins. *Trends in Biotechnology*. 2009;27(3):179-188. doi:10.1016/j.tibtech.2008.11.006.

272. Cooper MA. Optical biosensors: where next and how soon? *Drug Discovery Today*. 2006;11(23–24):1061-1067. doi:10.1016/j.drudis.2006.10.003.

273. Grieshaber D, MacKenzie R, Vörös J, Reimhult E. Electrochemical Biosensors - Sensor Principles and Architectures. *Sensors*. 2008;8(3):1400-1458. doi:10.3390/s80314000.

274. Wang L, Sipe DM, Xu Y, Lin Q. A MEMS Thermal Biosensor for Metabolic Monitoring Applications. *Journal of Microelectromechanical Systems*. 2008;17(2):318-327. doi:10.1109/JMEMS.2008.916357.

275. Becker B, Cooper MA. A survey of the 2006-2009 quartz crystal microbalance biosensor literature. *J Mol Recognit*. 2011;24(5):754-787. doi:10.1002/jmr.1117.

276. Stoney GG. The Tension of Metallic Films Deposited by Electrolysis. *Proceedings of the Royal Society of London Series A, Containing Papers of a Mathematical and Physical Character*. 1909;82(553):172-175.

277. Li S, Orona L, Li Z, Cheng Z-Y. Biosensor based on magnetostrictive microcantilever. *Applied Physics Letters*. 2006;88(7):73507. doi:10.1063/1.2174092.

278. Raiteri R, Grattarola M, Berger R. Micromechanics senses biomolecules. *Materials Today*. 2002;5(1):22–29.

279. Ziegler C. Cantilever-based biosensors. *Anal Bioanal Chem*. 2004;379(7-8):946-959. doi:10.1007/s00216-004-2694-y.

280. Liu D, Shu W. Microcantilever biosensors: probing biomolecular interactions at the nanoscale. *Current Organic Chemistry*. 2011;15(4):477–485.

281. Liu Q, Wu C, Cai H, Hu N, Zhou J, Wang P. Cell-based biosensors and their application in biomedicine. *Chemical reviews*. 2014;114(12):6423–6461.

282. Antonik MD, D'Costa NP, Hoh JH. A biosensor based an micromechanical interrogation of living cells. *IEEE Engineering in Medicine and Biology Magazine*. 1997;16(2):66-72. doi:10.1109/51.582178.

283. Park J, Ryu J, Choi SK, et al. Real-Time Measurement of the Contractile Forces of Self-Organized Cardiomyocytes on Hybrid Biopolymer Microcantilevers. *Anal Chem*. 2005;77(20):6571-6580. doi:10.1021/ac0507800.

284. Park K, Jang J, Irimia D, et al. "Living cantilever arrays" for characterization of mass of single live cells in fluids. *Lab on a Chip*. 2008;8(7):1034–1041.

285. Xi J, Schmidt JJ, Montemagno CD. Self-assembled microdevices driven by muscle. *Nat Mater*. 2005;4(2):180-184. doi:10.1038/nmat1308.

286. Das M, Wilson K, Molnar P, Hickman JJ. Differentiation of skeletal muscle and integration of myotubes with silicon microstructures using serum-free medium and a synthetic silane substrate. *Nature Protocols*. 2007;2(7):1795-1801. doi:10.1038/nprot.2007.229.

287. Das M, Gregory CA, Molnar P, Riedel LM, Wilson K, Hickman JJ. A defined system to allow skeletal muscle differentiation and subsequent integration with silicon microstructures. *Biomaterials*. 2006;27(24):4374-4380. doi:10.1016/j.biomaterials.2006.03.046.

288. Wilson K, Molnar P, Hickman J. Integration of functional myotubes with a Bio-MEMS device for non-invasive interrogation. *Lab on a Chip*. 2007;7(7):920. doi:10.1039/b617939h.

289. Zidovetzki R, Levitan I. Use of cyclodextrins to manipulate plasma membrane cholesterol content: Evidence, misconceptions and control strategies. *Biochimica et Biophysica Acta (BBA) - Biomembranes*. 2007;1768(6):1311-1324. doi:10.1016/j.bbamem.2007.03.026.

290. Ohtani Y, Irie T, Uekama K, Fukunaga K, Pitha J. Differential effects of alpha-, beta- and gamma-cyclodextrins on human erythrocytes. *Eur J Biochem*. 1989;186(1-2):17-22.

291. Fang Y, Ferrie AM. Optical biosensor differentiates signaling of endogenous PAR1 and PAR2 in A431 cells. *BMC Cell Biol*. 2007;8:24. doi:10.1186/1471-2121-8-24.

Appendix: List of Abbreviations

αCD	α-Cyclodextrin
AC	Alternating Current
AFM	Atomic Force Microscope
BPD	Barrels per Day
BSA	Bovine Serum Albumin
CBHs	Cellobiohydrolases
CBH I	Cellobiohydrolases I
CBM	Carbohydrate Binding Module
CD	Catalytic Domain
CFM	Chemical Force Microscopy
CI	Crystallinity Index
CPP	Clean Power Plan
ΔD	Change in the Energy Dissipation Factor
DFM	Dynamic Force Mode
DMEM	Dulbecco's Modified Eagle's Medium
DMSO	Dimethyl Sulfoxide
E	Energy to Separate Two cellulose Layers
E_0	Energy per Mole Glucose
EDTA	Ethylenediaminetetraacetic Acid
EFM	Electrostatic force microscopy
E_I	Internal Energy Between the Two Layers

EG	Endoglucanases
E_k	Kinetic Energy
Δf_n	Changes in the Resonant Frequency
FTIR	Fourier Transform Infrared Spectroscopy
HBSS	Hank's Balanced Salt Solution
HCC cellulose	High Concentration Cellulose
HEPES buffer	4-(2-hydroxyethyl)-1-piperazineethanesulfonic Acid
IC	Integrated Circuit
ITC	Isothermal Titration Calorimetry
LCC cellulose	Low Concentration Cellulose
LFM	Lateral force microscopy
ILs	Ionic liquids
MβCD	Methyl-B-Cyclodextrin
MCC	Microcrystalline Cellulose
MDCK cells	Madin–Darby Canine Kidney Cells
MFM	Magnetic force microscopy
MLCT	Silicon Nitride Microcantilevers
MSM	Magneto-resistive Sensitivity Mapping
NaOAc	Sodium Acetate Buffer
NH	Non-hydrolytic Cellulase
NMMO	N-Methylmorpholine N-oxide
pNPC	p-Nitrophenyl-β-D-Cellobioside
PVAm	Polyvinyl Amine
QCM-D	Quartz Crystal Microbalance with Dissipation Monitoring

ΔR%	Percentage Change of Roughness R_a,
R_a	Average Roughness
SCM	Scanning Capacitance Microscopy
SEM	Scanning Electron Microscope
SEPM	Scanning Electrical Potential Microscopy
SMD	Steered Molecular Dynamics
SPM	Scanning Probe Microscopy
STM	Scanning Tunneling Microscope
TEM	Transmission Electron Microscopy
U	Elastic Energy
XPS	X-ray Photoelectron Spectroscopy
XRD	X-ray diffraction

Vita

Wenjian Du

Education

2010-2017 Ph.D. in Chemistry
Drexel University, Philadelphia, PA, U.S.
2006-2009 M.A. in Material Science and Technology
Beijing University of Chemical Technology (BUCT), Beijing, China
2002-2006 B.A in Polymer Science and Technology
Beijing University of Chemical Technology (BUCT), Beijing, China

Research Experience

2010-Now Research Fellow Drexel University
Supervised by Dr. Jun Xi
2006-2009 Research Assistant Beijing University of Chemical Technology
Supervised by Dr. Qifang Li

Publications

•Xi, J.; Du, W.; Zhong, L. Probing the Interaction Between Cellulose and Cellulase with a Nanomechanical Sensor. In Cellulose – Medical, Pharmaceutical and Electronic Applications; Ven, T., Godbout, L., Eds.; InTech: Janeza Trdine, Rijeka, Croatia, 2013; 125–140

•Han, M.; Li, M.; Du, W.; Ji, H.; Xi, J. A Mammalian Cell-based Nanomechanical Biosensor. J. Nanomed Biotherapeut Discov. 2013, 2: 106

•Du, W; Wang, X; Chen, G; Li, Q. Studies on Quantum Dots Synthesized by Two Different Precursors[J]. Journal of Beijing University of Chemical Technology, 2009, 12(36): 69-73

Teaching Experiences

2010-2016 Teaching Assistant Drexel University
Classes teaches includes: CHEM 101, CHEM 102, CHEM 103, CHEM 113, CHEM 151

Conference Presentations and Other Professional Activities

•Du, W; Xi, J. "Novel approaches to study the interfacial enzymatic activity of cellulase: From the topographical standpoint". 252th ACS National Meeting, Philadelphia, PA. August, 2016

•Du, W; Xi, J. "Use microcantilever technique and AFM surface imaging to examine the time-dependent decrystallization of cellulose by cellulase". 250th ACS National Meeting, Boston, MA. August, 2015

•Du, W; Zhao, L; Zhao, K; Nguyen, C; Xi, J. "Using nano mechanical approach to study enzyme catalysis". 244th ACS National Meeting, Philadelphia, PA. August, 2012.

•Du, W; Zhao, L; Nguyen, C; Xi, J. "Use Nanomechanical Sensor to Detect Cellulase Activities Including Enzymatic Decrystallization and Hydrolytic Cleavage on Cellulose". Biophysical Society 57th Annual Meeting, Philadelphia, PA. February, 2013

Publications Contributing to this Thesis

1. Xi, J., Du, W. & Zhong, and L. Probing the Interaction Between Cellulose and Cellulase with a Nanomechanical Sensor, Cellulose - Medical, Pharmaceutical and Electronic Applications, Dr. Theo G.M. Van De Ven (Ed.), InTech (2013). doi: 10.5772/50285

2. Han, M.-J., Li, M., Du, W., Ji, H.-F. & Xi, J. A Mammalian Cell-based Nanomechanical Biosensor. Journal of Nanomedicine & Biotherapeutic Discovery (2012). doi:10.4172/2155-983X.1000106

(page intentionally left blank)